

2024-05-01

Bcl2 Mediated Targeted Drug Delivery For The Treatment Of Kidney Fibrosis And Stomach Cancer

Humayra Afrin
University of Texas at El Paso

Follow this and additional works at: https://scholarworks.utep.edu/open_etd



Part of the [Biology Commons](#), [Biomedical Commons](#), and the [Pharmacy and Pharmaceutical Sciences Commons](#)

Recommended Citation

Afrin, Humayra, "Bcl2 Mediated Targeted Drug Delivery For The Treatment Of Kidney Fibrosis And Stomach Cancer" (2024). *Open Access Theses & Dissertations*. 4061.
https://scholarworks.utep.edu/open_etd/4061

This is brought to you for free and open access by ScholarWorks@UTEP. It has been accepted for inclusion in Open Access Theses & Dissertations by an authorized administrator of ScholarWorks@UTEP. For more information, please contact lweber@utep.edu.

BCL2 MEDIATED TARGETED DRUG DELIVERY FOR THE TREATMENT OF KIDNEY
FIBROSIS AND STOMACH CANCER

HUMAYRA AFRIN

Doctoral Program in Environmental Science and Engineering

APPROVED:

Md Nurunnabi, Ph.D., Chair

Mahesh Narayan, Ph.D.

Sourav Roy, Ph.D.

Kisuk Min, Ph.D

Jaffer A Ajani, MD

Stephen L. Crites, Jr., Ph.D.
Dean of the Graduate School

Copyright

2024

Humayra Afrin

Dedication

I express my heartfelt gratitude to my husband and our two wonderful sons, Izhaan, and Ibtihaj, for their unwavering support, sacrifices, and constant encouragement, urging me to always strive for excellence. This endeavor is dedicated to them, as well as to my mother, whose inspiration was paramount in initiating the kidney fibrosis project. Additionally, I dedicate this work to the countless individuals enduring the hardships of cancer and kidney diseases.

BCL2 MEDIATED TARGETED DRUG DELIVERY FOR THE TREATMENT OF KIDNEY
FIBROSIS AND STOMACH CANCER

by

HUMAYRA AFRIN, MD

DISSERTATION

Presented to the Faculty of the Graduate School of
The University of Texas at El Paso
in Partial Fulfillment
of the Requirements
for the Degree of

DOCTOR OF PHILOSOPHY

Environmental Science and Engineering

THE UNIVERSITY OF TEXAS AT EL PASO

May 2024

Acknowledgements

Completing this PhD thesis has been a journey filled with challenges, growth, and invaluable support from many individuals whom I am deeply grateful to acknowledge.

First and foremost, I extend my heartfelt gratitude to my supervisor, Dr. Md Nurunnabi, for his unwavering guidance, patience, and expertise throughout this research endeavor. His insightful feedback, encouragement, and dedication have been instrumental in shaping this thesis and my scholarly development. I started my PhD journey with no significant prior research experience, under his supervision I learned whatever I know today, and am continuing to learn. As, I was a medical doctor I obliged by his word he told me once “Dream big, only then you can achieve small”.

I am also indebted to the members of my thesis committee, Dr. Mahesh Narayan, Dr. Sourav Roy, Dr. Kisuk Kin, Dr. Jaffer A. Ajani, for their invaluable feedback, constructive criticism, and scholarly contributions. Their expertise and insights have greatly enriched the quality and depth of this work.

I am grateful to The Department of Environmental Science and Engineering for providing the necessary resources, facilities, and financial support that made this research possible. Special thanks to department chair Dr. Craig Tweedie for his support in my every academic step. I am also indebted to my graduate coordinator Ms. Lina Hamdan for the support which helped me work without any worry about my health or my babies.

I am thankful to the Journal *ACS Applied Material and Interfaces* for accepting and publishing my first article from my PhD research works. Chapter 3 of this dissertation is copied from my article published in the Journal *ACS Applied Material and Interfaces*.

I extend my appreciation to my colleagues and fellow researchers for their camaraderie, intellectual exchange, and moral support. Their friendship and encouragement have been a source of inspiration and motivation during challenging times.

My deepest gratitude goes to my family for their unconditional love, encouragement, and sacrifices. Their unwavering support and belief in my abilities have been the cornerstone of my academic pursuits. I could not finish my PhD without the support of my husband Habibur Howlider. His sacrifices, patience, and belief in my abilities have sustained me through the challenges and triumphs of this journey. I am also immensely grateful to my precious baby Izhaan Rahman and Ibtihaj Rahman. Your boundless love, laughter, and presence have brought joy and balance to my life, reminding me of what truly matters amidst the rigors of academia. Your adorable giggles and innocent curiosity have been a constant source of inspiration and motivation, driving me to persevere and excel. I owe an immeasurable debt of gratitude to my parents for instilling in me a passion for learning, resilience in the face of adversity, and values of integrity and hard work. In addition to my immediate family, I am thankful for the love and support of Dr. Afroz and Dr. Md. Asadul Haque whose encouragement and belief in my abilities have been a constant source of strength and motivation.

In conclusion, I am immensely grateful to everyone who has played a part, no matter how small, in this journey towards the completion of my PhD thesis. Your support, guidance, and encouragement have been invaluable, and I am forever thankful for your contributions.

Abstract

Apoptosis, the programmed death of cells, is primarily regulated by a delicate balance between pro-apoptotic and anti-apoptotic signals. The Bcl-2 (B-cell lymphoma 2) family of proteins acts as anti-apoptotic agents, promoting cell survival. Dysregulation of these proteins is a common occurrence in conditions such as cancer and fibrosis, where overexpression of anti-apoptotic members can foster tumor cell survival and fibroblast activation. In this study, our aim was to explore the therapeutic potential of Bcl-2 inhibitors, both as a small molecule (specifically Navitoclax (Navi)), inhibitor and as Bcl-2 siRNA, for targeted treatment. Intravenous administration of Navi often leads to thrombocytopenia, necessitating a precise delivery strategy to the diseased site while maintaining therapeutic efficacy and minimizing side effects. Our initial project focused on utilizing PLGA-based nanoparticles conjugated with Angiotensin 2 (AT2), a protein commonly overexpressed in kidney disease, to achieve targeted delivery. Intravenous administration of Navi-loaded, AT2-conjugated PLGA nanoparticles demonstrated selective kidney targeting without inducing thrombocytopenia. Histological analysis revealed a reversal of fibrosis post-treatment with targeted nanoparticles, corroborated by improved renal function and apoptosis induction in kidney tissues. Encouraged by these findings, our subsequent endeavor involved advancing the delivery system for Bcl2 siRNA in stomach cancer. While siRNA holds promise for cancer therapy due to its ability to target specific genes, oral delivery remains challenging due to instability in the intestinal environment. To address this, we employed β -Glucan (BG), a mucoadhesive polymer, to shield and stabilize siRNA orally. In vivo studies in a stomach cancer mouse model demonstrated that BG-mediated siRNA formulations effectively reduced Bcl2 expression and induced apoptosis, offering a promising avenue for cancer treatment. In conclusion, our findings underscore the potential of targeted delivery systems for Bcl-2 inhibitors

in cancer and fibrosis therapy, providing a safe and effective means of inducing apoptosis at disease sites.

Table of content

BCL2 MEDIATED TARGETED DRUG DELIVERY FOR THE TREATMENT OF KIDNEY FIBROSIS AND STOMACH CANCER	I
Dedication.....	vi
Acknowledgements.....	v
Abstract.....	vii
Table of content	ix
List of Figure.....	xiii
Chapter 1: Introduction	1
1.1. Role of Bcl2 in cancer and fibrosis.....	1
1.2. Unmet need of an improved treatment for stomach cancer and kidney fibrosis	3
1.3. Approach taken in this study to address the limitations of current therapy	4
Chapter 2: Kidney selective Bcl2 inhibitor delivery improves fibrosis treatment.....	6
Abstract	6
Graphical abstract	7
2.1. Introduction.....	7
2.2. Materials & Methods	12
2.2.1. Materials	12

2.2.2. Synthesis of PLGA nanoparticles	12
2.2.3. Particle characterization (Size distribution, zeta Potential)	13
2.2.4. Loading content and in-vitro Release study.....	13
2.2.5. Docking Calculations and Molecular Dynamics Simulations.	14
2.2.6. Surface plasmon resonance (SPR) analysis	17
2.2.7. Cell culture and nanoparticle uptake.....	18
2.2.8. Immunocytochemistry	18
2.2.9. In-vivo mice model preparation.....	19
2.2.10. <i>In vivo</i> bio-distribution and nanoparticle targeting.....	20
2.2.11. Therapeutic efficacy of PLGA-NPs in the kidney fibrosis mice model	21
2.2.12. Histology and immunohistochemical staining.....	21
2.2.13. Immunofluorescence.....	22
2.2.14. Western blot analysis	22
2.2.15. TUNEL assay.....	23
2.2.16. Blood and serum analysis	23
2.2.17. Hydroxyproline measurement.....	23
2.2.18. Statistical Analysis.....	23
2.3. Results and discussion	24
2.3.1. Characterization of NPs ideal for targeting diseases specific to the kidney:	24

2.3.2. AT2 peptide and protein dynamics modulation shows protein peptide binding	27
2.3.3. In-vitro myofibroblasts promote accumulation of targeted NPs:	30
2.3.4. In-vitro therapeutic efficacy for α -SMA shows reduction of α -SMA in TNP/Navi group	32
2.3.6. Therapeutic efficacy of PLGA NPs	34
2.3.7. Reversal of fibrosis and pro-fibrotic protein expression with TNP/Navi	36
2.3.8. Improvement of kidney morphology and kidney function with TNP/Navi formulation	39
2.3.9. Navi, NP/Navi, and TNP/Navi treatment results in Bcl2 inhibition and apoptosis	43
2.4. Conclusions	44
Supplementary information	46
 Chapter 3: β -Glucan-Mediated Oral Codelivery of 5FU and Bcl2 siRNA Attenuates Stomach	
Cancer	50
Abstract	50
Graphical Abstract	51
3.1. Introduction	51
3.2. Materials and Methodology	56
3.2.1 Materials	56

3.2.2. Preparation of BG and formulations	57
3.2.5 Stability of the formulation	58
3.3 Results and Discussion	65
3.3.2 Mucoadhesive properties of BG	69
3.3.4 <i>In Vivo</i> imaging and biodistribution	72
3.3.5 Phenotypical <i>in vivo</i> treatment efficiency	73
3.3.6 Oral Bcl2 siRNA causes in-vivo gene silencing and apoptosis	75
3.3.7 Therapeutic Efficacy In Vivo.....	78
3.3.8 Serum biochemistry and toxicity	82
3.4 Conclusions.....	82
Supplementary information	83
Summary:.....	88
Acknowledgement	91
Reference:	92

Vita 107

List of Figure

- Figure 1: Role of AT2 in fibrosis development. AT2 binds with the AT2 receptor and activates TGF β -1. TGF β -1 later activates the Smad pathway and activated Smad causes activation of myofibroblast from fibroblast and thereby produces extra cellular matrix (α -SMA, collagen, CTGF, Fibronectin). AT2 can work without the Smad pathway where it can directly produce ECM, that activates Smad and augment fibrosis. 11
- Figure 2: Kidney fibrosis animal model preparation. Schematic representation of kidney fibrosis model preparation and treatment. The image of rat was retrieved from Chemdraw. 20
- Figure 3: Physical properties of NPs. Schematics of nanoparticles (A). Size and Zeta potential of the nanoparticle particles were measured by Zetasizer (B and C). The average size and zeta of TNP/Navi were 339 d.nm and -11.1333 mV. Whereas size and zeta potential of TNPs were 196.5 nm and -0.123 mV. SEM image of TNP/Navi NPs showed smooth surface (D), and SPR analysis response after running AT2 protein over the TNP liganded chip (E). 25
- Figure 4: AT2 peptide and protein dynamics modulation. Peptide RVYIHPI interacts and binds strongly to the N-terminus of AGTR1 membrane protein. **A)** Representative snapshot of the protein-peptide system in the DDPC membrane. The atoms of the membrane bilayer are shown as grey spheres, the AGTR1 protein is shown in cyan, and the peptide is colored according to the types of residues present. White represents non-polar residues; green represents polar residues and blue represents the basic residues. **B)** Binding energy between RVYIHPI and AGTR1 calculated over time for the 400 ns MD trajectory. The average binding energy was calculated over the last half of trajectory. **C)** 2D interaction diagram of protein-peptide interaction at the beginning of the simulation and after 400 ns of simulation. The peptide residues are shown using violet bonds whereas the protein residues are in orange. C, N and O atoms are shown as black, blue and red

circles. Hydrogen atoms have been omitted for clarity. The polar interactions between peptide and protein residues are shown using green dotted lines with a labeling of inter heavy atom distance involved in polar interaction. The protein residues having non-polar interaction are depicted using semi dark red semi circles. **D)** Surface electrostatic potential of the AGTR1 protein calculated using the APBS tool. The positively charged surface is shown in blue while the negatively charged surface is in red. The peptide in the binding pocket is colored according to the atom type: cyan (C), blue (N), and red (O). Hydrogen atoms are not shown for clarity. For better visualization of the peptide in the cavity, the front part of the protein has been removed and the cutting plane is colored in gray. 28

Figure 5: Cellular uptake of targeted NPs and Bcl2 inhibition. NPs uptake by NRK-49F cell line with TGF β -1. NP/RhB and TNP/RhB were added after 24 hr incubation of TGF β -1. Four hours after incubation with NP and TNP it was observed that TNP uptake was higher in the myofibroblast. Whereas no nanoparticle was up taken by the cells with NP/RhB. The scale bar represents 200 μ m (A). 30

Figure 6; In vitro therapeutic effects. α -SMA expression of untreated and treated cell with Fasudil, Navi, NP/Navi, and TNP/Navi (A). The image shows reduced expression of α -SMA with the treatment group. Scale bar represents 50 μ m. The images were quantified in ImageJ and the graph represents the relative intensity (B) and area% (C). In both parameters, α -SMA reduced the most in TNP/Navi group..... 31

Figure 7: In-vivo biodistribution of the NPs. Biodistribution was observed for 24 hr post-administration of the targeted and non-targeted NPs via tail vein. The AT2 conjugated PLGA nanoparticle attached with RhB (TNP/RhB) dye showed kidney targeting ability and mostly accumulated in the kidney for at least 24 hr. Kidney regions are indicated in white dash in the TNP

group. Other than liver no signal was captured with non-targeted NP/RhB particles. Ex vivo nanoparticle uptake in healthy and fibrosed kidneys were measured. Representative ex-vivo images of healthy and fibrosed kidney after treatment with NP/RhB and TNP/RhB. Healthy control without any treatment was used as negative control (control). Healthy represents healthy treated with TNP/RhB, NP/RhB group represents fibrosed kidney treated with NP/RhB, and TNP/RhB represents fibrosed kidney with TNP/RhB. The image shows higher accumulation of targeted particles in fibrosed kidney both in terms of area percentage (B) and fluorescent intensity (C). 33

Figure 8: Size and weight of the harvested kidney. Image of the harvested kidneys (A). Size and weight (C) and (D) of kidneys in different treatment groups were measured after sacrifice. The size of the untreated kidney shrunk by 38.20% (p value 0.0001) than healthy control (A). After treatment with Navitoclax (Navi), Fasudil, NP/Navi, and TNP/Navi, kidney sizes increased up to 26.66% with TNP/Navi. Weight of the mice (B) before and during the treatment. 35

Figure 9: Masson's Trichrome staining of the kidney section. Masson's Trichrome staining of the kidney section in 8X magnification. Scale bar represents 100 μm. The image indicated reduction of fibrosis with the treatment specifically with Fasudil, NP/Navi and TNP/Navi (A). (B) quantitative representation of fibrosis in the kidney section. Error bar represented SD and scale bar represented 100 μm. Hydroxyproline measurement from mice serum showed higher level of hydroxyproline in untreated group which got decreased by the treatment group specifically with Fasudil, NP/Navi and TNP/Navi (C). P-value *indicated <0.05, ** indicated <0.001, and *** indicated <0.0001..... 37

Figure 10: immunofluorescence of kidney sections. Images of kidney sections for CTGF and α-SMA were obtained by direct immunofluorescence (A). The green signal indicates CTGF, and red indicates α-SMA expression. Scale bar represents 100 μm. Western blot of α-SMA (B) and CTGF

(E) was done from the kidney tissue lysate. Quantitative analysis of WB data revealed that untreated kidney tissue had higher expression of both α -SMA (C) and CTGF (F) which reduces with the treatment. (D) and (G) represent the quantitative analysis of α -SMA and CTGF respectively. The error bar represents the SD..... 39

Figure 11: Histology of kidney tissue. H&E staining of kidney sections from different treatment group (A). The untreated kidney section showed damaged renal structure whereas structure improved with the treatment. Serum analysis of kidney function marker Creatinine (B) and Blood urea nitrogen (BUN) (C). High creatinine and BUN level in untreated group indicated the renal disfunction, which improved with the treatment group. Total protein (D) was less than normal level in untreated group of mice. Alkaline phosphatase (ALP), alanine aminotransferase (ALT) was in normal range with all the groups (E and F).). Blood platelet (G)level was lower than normal range with oral Navi group and normal with other groups. The Hb (H) level was below normal range for the untreated mice which indicates anemia in the untreated kidney fibrosis model..... 42

Figure 12: Immunohistochemistry of kidney tissue for Bcl2 expression. Bcl-2 inhibition and apoptosis of tissue after treatment. (A) Tunnel assay shows apoptosis (green dot) of fibrotic cell. (B) WB analysis of Bcl2. Bcl2 expression was decreased in the group treated with TNP/Navi. (C)+(D) Quantitative analysis of WB data and TUNEL assay. Scale bar represents 100 μ m. 44

Figure S 1: Proton NMR. Proton NMR of AT2 (A), PLGA/NHS (B), Navi (C) and PLGA-AT2 (D)..... 46

Figure S 2: SPR spectra. SPR spectra after immobilization of carboxylated gold chip with PLGA/AT2 nanoparticle (A). Response after running collagen over the nanoparticle (NP) liganded chip (B). (a) represents base line response with PBS, (b) is the response of binding of collagen with AT2 and (c) is the curve for dissociation..... 47

Figure S 3: Stability of NPs. The stability of NPs in PBS with 10% FBS were measured by size (A) and zeta (B) potential of the particles for up to 6hrs. It was observed that the particles were stable in the solution, especially (TNP/Navi) particle. 48

Figure S 4: Electrostatic potential surface of the AT2 protein binding to AT2 peptide. Analysis of the electrostatic potential surfaces of the AGTR1 protein binding to RYIHPI peptide. Blue surfaces indicate regions of positive electrostatic potential and red surfaces indicate regions of negative electrostatic potential..... 48

Figure S 5: Transformation of fibroblast to myofibroblast. NRK-49F cell before (a) and after (b) adding TGF β -1. After the incubation of TGF β -1 the cells became slender from round shape. ... 49

Figure S 6: Platelet count post-treatment with different Navi formulations. After administration of oral Navi, NP and TNP blood were collected at each different time point and platelet were measured. A sudden drop of platelet with oral Navi was observed in the 1st hr. With TNP the platelet did not drop as much as oral Navi as 1st hr also was constant up to the 6hrs. With oral Navi the platelet count was decreasing with each time point..... 49

Figure 13: The Mechanism of Action of Co-Treatment of 5-FU and Bcl2 siRNA and Their Synergy to Improve Stomach Cancer Treatment. 55

Figure 14: Chemical and physical properties of the formulations. (A) Chemical structure (repeating unit) and schematic presentation of BG. (B) Schematic representation of preparation of formulations; BG/siRNA, BG/5FU and BG/5FU/siRNA. (C) SEM images of BG/5FU/siRNA BG showed smooth surface and nano size (Scale bar= 5 μ m). (D) Size distribution, and (E) zeta potential of all the formulations were measured using DLS and zeta analyzer, respectively. Data presented as mean \pm SEM, where n=3..... 67

Figure 15: Mucoadhesive properties of BG. (A) A schematic representation of mucoadhesiveness of BG and how it facilitates the transport of siRNA and 5FU across the epithelium. BG/coumarin-6 was incubated on the porcine intestine for a different period and washed for 5 min before taking the image. (B) Image shows that BG facilitates to penetrate of the hydrophobic coumarin-6 into the intestinal layer with time. Whereas only coumarin-6 without BG does not diffuse through the intestine. (C) The same section of BG/coumarin-6 was taken under a ChemiDoc imager (BioRad, USA) and the result corresponded with the image of BG/coumarin-6 in (B). The components in figure (A) were obtained from smart.servier.com. 68

Figure 16: Stability of BG/siRNA particles in PBS and simulated gastric juice Schematic of the formulation (A). The size and zeta potential of BG and BG/siRNA in PBS and gastric juice were measured. Particle size distribution of BG and BG/siRNA was observed in PBS (B) and in simulated gastric juice (C) at 0, 1, 2, 4, and 6 hr. It was observed that after adding siRNA the size of BG increased initially at 0 hr measurement. (D) Gel electrophoresis analysis of naked siRNA and BG/siRNA incubated with simulated gastric juice up to 6 hr. The image showed that naked siRNA was not stable in simulated gastric juice even 1 hr after mixing, whereas siRNA/BG was found to be stable up to 6 hr after mixing with simulated gastric juice. Zeta potential of BG and siRNA with BG was also observed in PBS (E) and in simulated gastric juice (F). Zeta potential of siRNA with BG showed negative charge constantly up to 6 hr. Data presented as mean \pm SEM, where n=3. 71

Figure 17: Fluorescence imaging to investigate biodistribution. (A) In vivo imaging shows noninvasive fluorescence-based localization of orally administered formulations. (B) Ex vivo images of the harvested organs show biodistribution of mice at pre-administration, after 2, 4 and

6 hr. Magnified images of GI tract show that BG particle remain in the stomach at least for 6 hr whereas slowly diffused via intestine. 73

Figure 18: In vivo therapeutic efficacy. (A) Schematic of animal model preparation and treatment. B) Image of the stomach collected from different group of treatment- Healthy (a), Untreated cancer (c), BG/5FU (c), 5FU (d), siRNA (e), BG/siRNA (f), BG/5FU/siRNA (g). (C) and (D) weight and size of the stomach. Data presented as mean \pm SEM, where n=5. 74

Figure 19: Immunohistochemistry to attribute apoptosis. (A) TUNEL assay shows broken nucleus (red arrow) in siRNA, BG/siRNA, and BG/5FU/siRNA groups. Scale bars represent 200 μ m. (B) Western blot analysis also shows reduced Bcl2 expression in BG/5FU/siRNA group compared to naked siRNA and BG/siRNA. The error bar represents the standard deviation. (C) Quantitative analysis of WB, and (D) apoptosis in percentage. Data presented as mean \pm SEM, where n=5. P value <0.0001 is denoted as ***. 76

Figure 20: Immunohistochemistry to attribute expression of Bcl2 protein. (A) Immunohistochemistry for Bcl-2 protein shows higher expression of Bcl-2 in untreated mice stomachs (red arrow). The naked oral siRNA treatment group also had more Bcl-2 expression than BG/siRNA and BG/5FU/siRNA. The scale bar represents 100 μ m. (B) Quantification of Bcl2 immunofluorescence data analysis was presented. Data presented as mean \pm SEM, where n=5.. 77

Figure 21: Immunofluorescence for ki67 of stomach sections of different treatment groups. (A) A higher expression of ki67 (yellow arrow) was observed in untreated group, whereas after treatment the expression got reduced specially with BG/5FU/siRNA formulation. Scale bar represents 100 μ m. (B) Ki67 expression was quantified compared to healthy control. Data presented as mean \pm SEM, where n=5. 79

Figure 22: Histology of stomach. **(A)** The histological staining (H&E) shows a growth (blue arrow) in the untreated section, while after treatment with 5FU, 5FU/BG, and BG/5FU/siRNA the tumor region got significantly reduced. **(B)** H&E staining of stomach cancer sections with 40X magnification. The red rectangular area was cropped and magnified for better morphological understanding. The untreated, naked siRNA, and BG/siRNA shows the feature of adenocarcinoma. The section of BG/5FU/siRNA treatment group almost resemblance as healthy stomach. 80

Figure 23: Serum biochemistry to demonstrate toxicity. Serum analysis for **(A)** total protein (TP), **(B)** alanine aminotransferase (ALT), **(C)** creatinine, and **(D)** blood urea nitrogen (BUN) does not show any significant difference of the treatment group with the untreated. Data presented as mean \pm SEM, where n=5. 81

Figure S 7: Size of BG in PBS **(A)** and Gastric Juice **(B)**. In both PBS and GJ size tends to increase with time. 83

Figure S 8: SEM image of BG/FU **(A)** and BG/siRNA **(B)** 84

Figure S 9: Release study of 5FU. Free 5FU shows a burst release in 2nd hour compared to the BG/siRNA and BG/5DU/siRNA. BG/5FU and BG/5FU/siRNA shows a sustain release up to 10hrs..... 84

Figure S 10: Stability of siRNA formulation in BG. Stability of siRNA formulation in BG. **(A)** Agarose gel electrophoresis of naked siRNA in GJ after incubating for 1,2,4,6 and 8hrs. **(B)** Nanodrop measurement of siRNA shows that naked siRNA without BG is not stable in GJ..... 85

Figure S 11: Surface plasmon resonance (SPR) analysis for binding affinity of BG and mucin. Shows the picks for **(d)** EDC/NHS and **(e)** BG. BG was used as ligand over COOH-Au chip. .. 85

Figure S 12: Figure S1.6. SPR analysis shows the binding of BG to mucin. Curve- a) indicates association of BG with mucin, b) represents the plateau and where BG continues to bind with mucin and c) indicates the dissociation of BG with mucin. 86

Figure S 13: Cellular viability (A) and IC50 (B) value of 5FU formulations. Cellular viability (A) and IC50 (B) value of 5FU formulations. The IC50 value of 5FU, BG/5FU and BG/5FU/siRNA was found to be around $25\mu\text{M}\pm 8.3$, $35\mu\text{M}\pm 9.3$ and $35\mu\text{M}\pm 7.4$ respectively..... 86

Figure S 14: Size and weight of intestine post-treatment. (A) Intestine collected from different treatment group. Weight (B) and size (C) of the collected intestine were measured. No significant difference was found between the treatment and untreated group. 87

Figure S 15: H&E staining of intestine shows no significant toxicity. H&E staining of duodenum, jejunum, and ileum of different treatment groups. No significant toxic effect was observed in the intestinal section..... 87

Chapter 1: Introduction

1.1.ROLE OF BCL2 IN CANCER AND FIBROSIS

Apoptosis, often referred to as programmed cell death, is a highly regulated process of cellular self-destruction that occurs in multicellular organisms [1]. It plays crucial roles in development, tissue homeostasis, and the elimination of damaged or potentially harmful cells [2]. Bcl-2 is primarily known for its anti-apoptotic function. It resides in the outer mitochondrial membrane and functions to inhibit the intrinsic apoptotic pathway, also known as the mitochondrial pathway [3]. This pathway is activated in response to various cellular stresses such as DNA damage, oxidative stress, or growth factor deprivation [4]. Bcl-2 interacts with the Bax and Bak pro-apoptotic proteins. These proteins promote apoptosis by inducing mitochondrial outer membrane permeabilization (MOMP), leading to cytochrome c release and activation of caspases [5]. Bcl-2 inhibits the pro-apoptotic activity of Bax and Bak, thereby preventing MOMP and apoptosis [5]. Dysregulation of Bcl-2 expression or function can have profound implications for cell survival and contribute to various diseases, including cancer. In many types of cancer, Bcl-2 is overexpressed, leading to increased resistance to apoptosis [6]. Additionally, Bcl-2 has been implicated in promoting cancer cell migration, invasion, and metastasis in certain contexts [7]. Bcl2 has been targeted by researchers for various cancer treatment such as hematological cancers [8], ovarian cancers, melanoma [9].

Bcl-2 has also been implicated in promoting the survival of fibrogenic cells, such as fibroblasts and myofibroblasts, which are key mediators of tissue fibrosis [10]. Enhanced expression of Bcl-2 in these cells may protect them from apoptosis and prolong their survival, thereby promoting fibrogenesis and tissue remodeling. Bcl-2 has been found to interact with various signaling molecules involved in fibrogenesis, such as transforming growth factor-beta (TGF- β) and nuclear

factor kappa B (NF- κ B) and p53/p21^{WAF1}, to promote fibroblast activation and collagen production [11]. This suggests that Bcl-2 may contribute to the pathogenesis of fibrosis by enhancing fibroblast activation and extracellular matrix deposition. In this study we have targeted Bcl2 protein for the treatment modality.

In this study we have used Navitoclax, also known by its generic name ABT-263, a small molecule. Navitoclax works by blocking the activity of certain Bcl-2 family proteins, particularly Bcl-2, Bcl-xL, and Bcl-w. By inhibiting these proteins, Navitoclax can promote apoptosis in cancer cells, leading to their death [12]. Navitoclax has shown efficacy in preclinical and clinical studies against various types of cancer, including chronic lymphocytic leukemia (CLL), small cell lung cancer, and lymphomas [13]. Although, the primary focus of Navitoclax (Navi) has been cancer treatment, its mechanism of action as a Bcl-2 family inhibitor suggests potential applications in fibrosis treatment due to its ability to induce apoptosis in activated myofibroblasts, which are key contributors to fibrosis progression [14]. Preclinical studies have shown promising results regarding the potential anti-fibrotic effects of Navi in various models of fibrosis, including liver fibrosis, lung fibrosis (such as idiopathic pulmonary fibrosis), and renal fibrosis [15] [16]. However, despite being a very potential effect for cancer and fibrosis treatment, Navi still did not get FDA approval because of its serious side effect. Navi has been found to create, thrombocytopenia or low platelet count in 63% of patients and neutropenia (low white blood cell count) in 51% of patients [17] [18][19]. Addressing these limitations requires ongoing research and innovation in areas such as precision medicine, targeted therapy, early detection, supportive care, and patient-centered approaches to cancer treatment. In this study we tried to identify a treatment option with Navi without these side effects with targeted delivery of Navi to the site of disease. We also envisioned to establish an easy patient friendly Bcl2 mediated therapeutic approach.

1.2.UNMET NEED OF AN IMPROVED TREATMENT FOR STOMACH CANCER AND KIDNEY FIBROSIS

Both the stomach cancer and kidney fibrosis suffers from lack of proper treatment option and high mortality and morbidity rate [20]. According to the American Cancer Society, the estimated mortality rate for stomach cancer in the United States in 2021 was about 5.5 per 100,000 men and women per year. It is also important to note that Hispanic people suffers from stomach cancer twice as more compared to Non- Hispanic White [21]. The development of better treatment options for stomach cancer is essential to improve patient outcomes, increase survival rates, reduce treatment-related toxicity, and enhance the quality of life for patients living with this disease. Till now the curative option for stomach cancer is surgery and postoperative adjuvant therapy [22]. Even after a painful surgery the survival is not ensured as, according to the American Cancer Society, the 5-year relative survival rate is only about 32%. We tried to develop an oral, effective, painless cure for stomach cancer that does not involve painful surgery or injection.

On the other hand, kidney fibrosis is a key pathological process in the development and progression of chronic kidney disease (CKD). About 10-14% of world population is currently affected with kidney fibrosis [23]. According to the report of National Institute on Diabetes and Digestive and Kidney Diseases (NIDDK) 2020, 100.6 per 1,000 people with CKD die with a higher rate in Black and Hispanic people compare to their White counterparts. On top of that it is a disease that often diagnose late because of being asymptomatic and having non-specific symptoms in the early stage. [24]. If left untreated, progressive kidney fibrosis can eventually lead to end-stage renal disease (ESRD), where the kidneys are no longer able to function adequately to sustain life. At this stage, patients require renal replacement therapy, such as dialysis or kidney transplantation, to survive. Despite having such alarming statistics there is no fibrosis targeted treatment available in the market. The last medication for CKD approved by FDA was Jardiance, to slow the progression of

ESRD [25]. The development of improved treatments for CKD is critical for reducing disease burden, improving patient outcomes, and enhancing quality of life for affected individuals is a demand of time now. Advances in research and innovation are essential for addressing the unmet needs of CKD and stomach cancer patients and improving the standard of care for this chronic condition. Our study is an effort to do that.

1.3. APPROACH TAKEN IN THIS STUDY TO ADDRESS THE LIMITATIONS OF CURRENT THERAPY

We have used nanoparticle mediated targeted drug delivery to avoid the current limitation of treatment. Targeted drug delivery refers to the administration of medication specifically to the site of action within the body, such as a particular organ, tissue, or cell type, while minimizing the exposure of other tissues [26]. Targeted drug delivery offers several advantages over the conventional therapy such as, enhanced therapeutic effect of medications by ensuring a higher concentration of the drug to the site of action, minimize exposure to healthy tissues reduces the likelihood of adverse effects with systemic drug administration, lower doses and less frequent dosing improves the patient adherence to treatment regimens [27][28]. In this study we have used PLGA and BG to deliver the drug on the targeted site. PLGA is a widely used polymer in drug delivery systems due to its biodegradability, biocompatibility, tunable properties, and versatility. PLGA nanoparticle formulation enables controlled release of the drug over time, providing sustained therapeutic levels in the body. [29]. PLGA nanoparticles can also be surface-modified or functionalized with ligands or targeting moieties to achieve targeted drug delivery to specific tissues, cells, or organelles to enhance the drug efficacy while minimizing off-target effects and toxicity [30]. For the treatment of kidney fibrosis, we have modified the surface of PLGA nanoparticle with angiotensin 2 (AT2) peptide to obtain the targeted delivery to fibroblast. AT2 is

a protein that plays a dominant role in development of kidney fibrosis and has been found to be over expressed in renal fibrosis [31]. By promoting proliferation, inflammation and fibrosis, AT2 contributes to the development of chronic diseases like chronic kidney disease [32].

On the other hand, BG has been used as a delivery vehicle for stomach cancer. Mucoadhesive properties of BG helps the particle to remain in the stomach for longer time period and provide stomach specific targeting ability, as the stomach has a very thick ($\sim 700\mu\text{M}$) mucous layer [33].

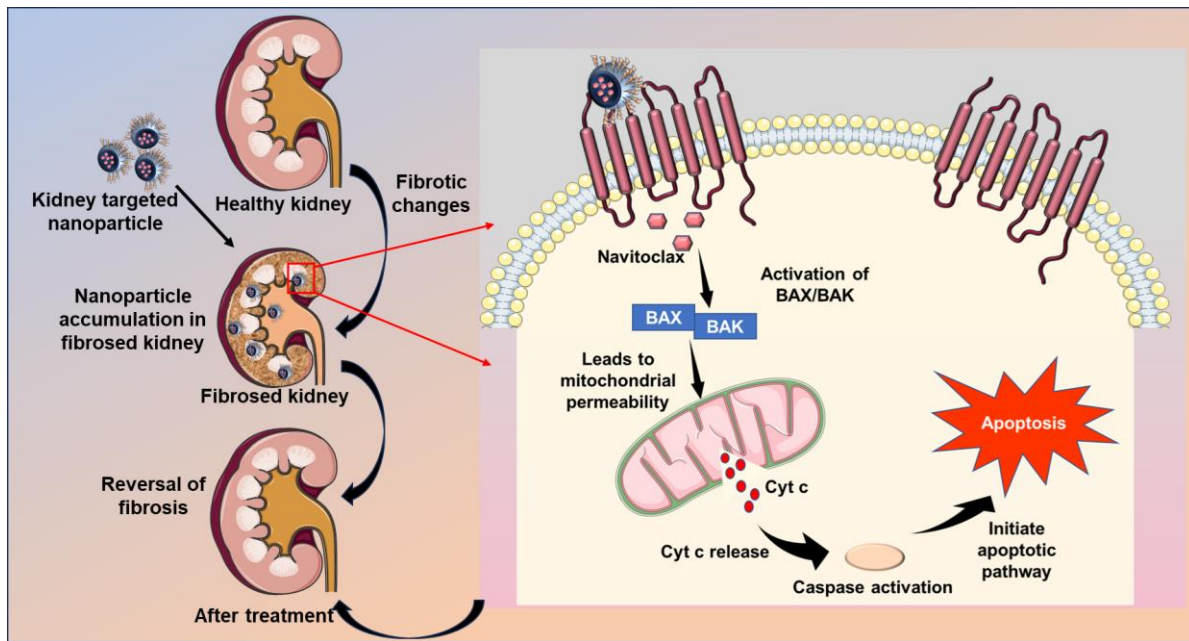
The objective of this study was to address the limitation of Bcl2 inhibitors and promise a better therapeutics for both cancer and fibrosis. In chapter one we have presented the study of kidney fibrosis where we have delivered intravenous Navi to reverse kidney fibrosis while reducing the side systemic adverse effects. Chapter 2 consists of the study of stomach cancer treatment with Bcl2 siRNA. Here the pivotal point was to identify an even more advanced delivery strategy that will provide superior therapeutic efficacy compared to conventional therapy while reducing the side effects. Here we have delivered Bcl2 siRNA orally with the help of BG.

Chapter 2: Kidney selective Bcl2 inhibitor delivery improves fibrosis treatment

ABSTRACT

Kidney fibrosis is one of the deadliest diseases. Kidney fibrosis often goes undiagnosed due to the absence of symptoms until the disease progresses to advanced stages, at which point dialysis or kidney transplant become the only viable treatment options. Despite the significant morbidity and mortality associated with kidney fibrosis, there is currently no treatment available that efficiently and effectively addresses the condition. This study aims to develop a nanoparticle-mediated therapeutic modality targeting kidney fibrosis, anticipating improved therapeutic outcomes. We have modified Poly(lactic-co-glycolic acid (PLGA) nanoparticle to link with angiotensin 2 targeting peptide and loaded with the Bcl-2 inhibitor (Navitoclax/Navi), to carry the payload to the site of action efficiently and specifically. Navi induces apoptosis by inhibiting the anti-apoptotic protein Bcl2. The therapeutic efficacy of various Navi formulations was investigated by both in-vitro and in-vivo models and compared to a group treated with Fasudil, a Rho-kinase inhibitor. Significant reduction of Bcl2 expression and upregulation of apoptosis were observed in group of mice treated with targeted nanoparticle (TNP/Navi) when compared to free Navi or non-targeted formulation (NP/Navi), using immunohistochemistry and molecular biology techniques. A significant reduction in α -SMA and CTGF was observed in the TNP/Navi group for both in-vitro and in-vivo models, that demonstrates an obvious indication of therapeutic potential of the developed formulation. Conservation of normal kidney morphology and less collagen deposition in the kidney treated with TNP/Navi further consolidates that AT2 targeted nanoparticle mediated apoptosis upregulation has the potential to reverse the pathology of kidney fibrosis.

Keywords: kidney; fibrosis; targeted therapy; nanoparticle; navitoclax



GRAPHICAL ABSTRACT

2.1. INTRODUCTION

Fibrosis is a pathological process characterized by the excessive accumulation of extracellular matrix (ECM), mostly collagen, which leads to functional impairment and ultimately functional failure of the affected organ [34]. Fibrosis can occur in many organs, including the kidney, heart, liver, lung, and skin, because of impaired healing of an injury. The key cellular basis of renal fibrosis is the activation of myofibroblasts, resulting in the excessive accumulation of ECM and inflammatory cell infiltration [35][36]. Renal fibrosis, an underlying pathology in the development of chronic kidney disease (CKD), affects 15% of the US populations [37]. CKD often remains undiagnosed until it reaches the end-stage kidney disease (ESKD), as symptoms are not typically apparent in the early stages [38]. Due to the lack of proper therapeutic modalities, 69% of patients are managed in the clinic by dialysis, and 31% are managed by kidney transplant at the ESKD [39]. Both available mitigation options are very expensive, with a mortality rate of 160.8 in every 1,000

among patients managed with dialysis and 50 out of 1000 patients those have received a kidney transplant in 2018 [40][39].

Despite the substantial morbidity and mortality linked to renal fibrosis, there is currently no clinically effective treatment, resulting in kidney fibrosis being a persistent condition. Some antifibrotic agents have demonstrated great potential, but their use is limited due to inadequate efficacy and off-target effects, hindering their ability to reverse the underlying pathology of fibrosis[41]. Clinical management of CKD involves treating symptoms such as high blood pressure, dyslipidemia, electrolyte imbalance, anemia, metabolic acidosis, vitamin D deficiency, uremia [42], and other comorbid conditions, in addition to the use of immunosuppressing agents. Treatments include the use of angiotensin-converting enzyme inhibitors, angiotensin 2 (AT2) receptor blockers, adjustments to drug dosing, and avoidance of potential nephrotoxins to slow down disease progression[43]. Rho-kinase inhibitors, investigated in preclinical rodent models, have emerged as potential candidates for fibrosis treatment [44,45]. However, the lack of specificity and random localization of Rho-kinase inhibitors can lead to various complications, such as conjunctival hyperemia, corneal verticillata, pain at the instillation site, and conjunctival hemorrhages [46]. Therefore, there is an unmet need to discover safer therapeutic candidates and develop a myofibroblast-targeted delivery system that offers improved efficiency and enhanced biosafety.

Navitoclax (Navi) is a novel B-cell leukemia 2 (Bcl-2) inhibitor that induces apoptosis, a form of programmed cell death. In normal wound healing process myofibroblast is cleared up by apoptosis process, however in pathologic condition myofibroblast becomes resistant to apoptosis and [47]. Bcl2 expression in myofibroblast is crucial in the development of fibrosis. Some other fundamental pathways responsible for fibrosis are Wnt, MRTF-A/SRF, Smad, Klotho, and

microRNAs. [48,49]. Various studies, including our own, have demonstrated Navi's potential to ameliorate cancer and slow down fibrosis progression [13,50,51]. Recently, Bcl2 inhibitors have exhibited remarkable therapeutic effects on interstitial and pulmonary fibrosis [52–54]. However, Navi has not yet been approved by the FDA due to severe hematological toxicities observed in clinical trials [55]. Rudin et al. reported that 40% of patients in clinical trials experienced grade III-IV thrombocytopenia as a result of intravenous administration of Navi[55]. Aside from thrombocytopenia, no severe side effects were observed in either pre-clinical or clinical studies involving rodents and humans, respectively [56].

Biocompatible delivery vehicles have been investigated to address the hematological side effects and other toxicity issues caused by off-target delivery, aiming to prevent drug-blood interactions during systemic circulation [57,58]. Specifically, PLGA nanoparticles (NP) have been used for drug delivery for over two decades, enabling organ specific drug delivery to the liver, lungs, and the kidneys [59–61]. To improve the targeting of AT2 overexpressed cells such as fibroblast and myofibroblasts within the kidney, the surface of PLGA NP was modified with an AT2 (angiotensin 2) targeting peptide (RVYIHPI) [62]. The renin-angiotensin system (RAS) plays a critical role in the pathogenesis of renal and cardiovascular disorders, including fibrosis, due to its regulatory functions in arterial pressure and extracellular fluid volume [49]. RAS (Renin-Angiotensin System) pathway activation begins in the kidney with the production of Renin. Renin converts angiotensinogen to angiotensin 1 (AT1), which is then converted to AT2 by angiotensin-converting enzyme (ACE). AT2, the active component of RAS, acts on the kidney, heart, and blood vessels. AT2 activates transforming growth factor- β (TGF β -1) and plays a key role in the development of fibrosis (Figure 1). Furthermore, AT2 stimulates collagen and fibronectin

production, which in turn activates Smad signaling pathways to induce fibrosis [32,49,63,64]. As a result, the AT2 protein has been demonstrated to be overexpressed in kidney fibrosis [64,65].

We hypothesize that a targeted delivery approach specific to AT2 can increase the specificity and potency of the therapeutic modality by concentrating Navi within the cells of interest, for instance myofibroblasts. We also hypothesize that uptake of Navi by other cells where Bcl-2 proteins are not upregulated will not be effective in inducing apoptosis and will thereby minimize the risk of nonspecific accumulation mediated toxicity. In the present study, Navi has been used as a therapeutic agent to alleviate kidney fibrosis. Navi, a phase 2 clinical trial small molecule drug, was loaded into a PLGA nanosphere and its surface was modified with AT2 to improve the targeting specificity toward the cells associated with fibrosis in kidneys. We found that the AT2 targeted PLGA nanoparticle loaded with Navi can reverse kidney fibrosis when administered intravenously to mice with kidney fibrosis. Histological and pathological analysis revealed no signs of systemic or local toxicities, as direct interaction between blood cells and Navi was prevented by the PLGA. Immunohistochemical analysis of the tissues demonstrated that the therapeutic efficacy and apoptosis induced by Navi formulations were higher than the positive control Fasudil. This approach demonstrates promising potential and clinical translational possibilities for improved management of CKD and should be further evaluated using advanced

pre-clinical genetically modified animal models for kidney fibrosis.

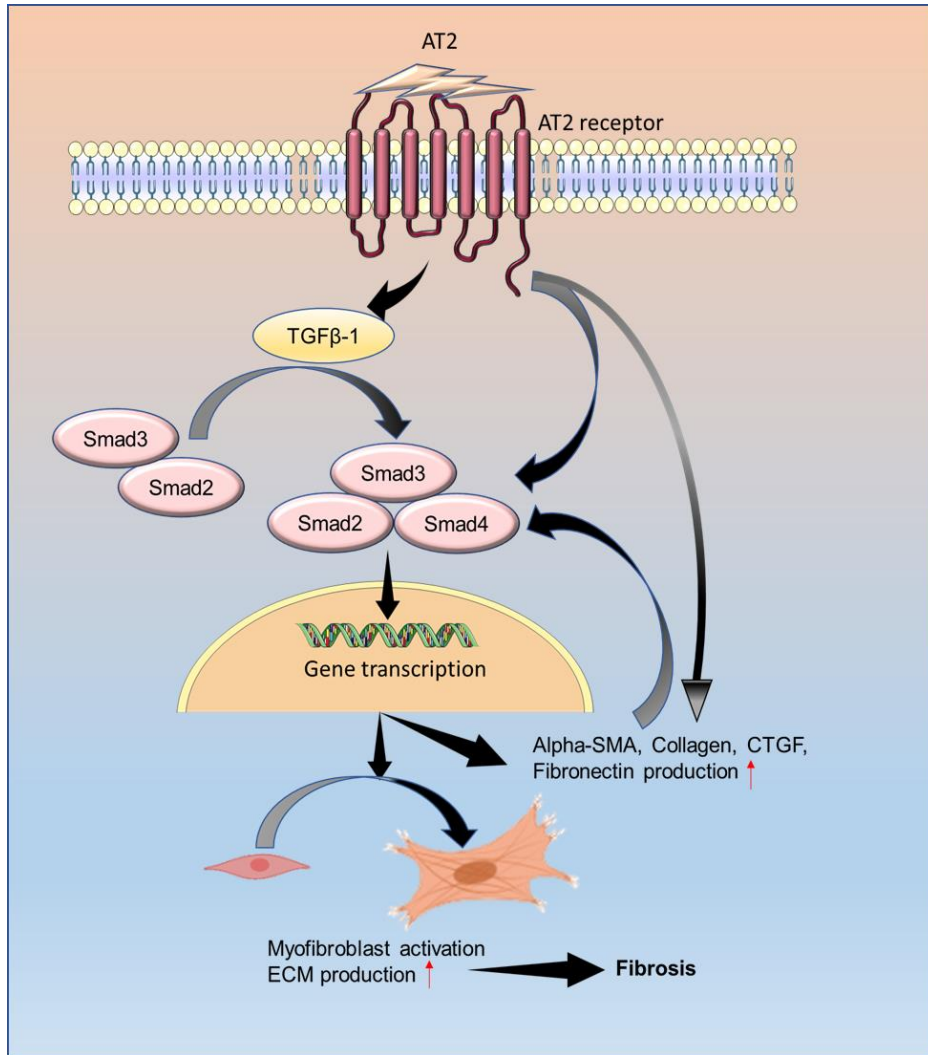


Figure 1: Role of AT2 in fibrosis development. AT2 binds with the AT2 receptor and activates TGFβ-1. TGFβ-1 later activates the Smad pathway and activated Smad causes activation of myofibroblast from fibroblast and thereby produces extra cellular matrix (α-SMA, collagen, CTGF, Fibronectin). AT2 can work without the Smad pathway where it can directly produce ECM, that activates Smad and augment fibrosis.

2.2. MATERIALS & METHODS

2.2.1. Materials

PLGA (lactide:glycolide monomer ratio of 50:50, molecular-weight 12000 Da), Polyvinyl Alcohol (PVA), and Rhodamine B (RhB) were purchased from Sigma–Aldrich (St. Louis, MO). NRK-49F cells and DMEM media were obtained from ATCC (Manassas, VA). Phosphate buffer saline (PBS), penicillin–streptomycin, trypsin/EDTA, and penicillin were purchased from Gibco BRL (Grand Island, NY, US). TUNEL click, Hoechst and all organic solvents were purchased from Thermo Fisher Scientific (Fremont, CA). Solvents were either HPLC grade or American Chemical Society analytical grade reagents. Bcl2 rabbit polyclonal antibody and secondary anti-rabbit antibody conjugated with alexa 488 fluorophore were acquired from (Abclonal, Woburn, MA). The distilled water used was of Milli-Q quality (Millipore, Bedford, MD).

2.2.2. Synthesis of PLGA nanoparticles

The PLGA nanoparticles were prepared using a slightly modified version of the method described in our previously published article [66]. Briefly, PLGA was dissolved in DCM with EDC and NHS and stirred overnight in a reactor. The following day, a cold methanol/ethyl ether co-solvent (50%, V/V) was added to the solution, and the precipitate was lyophilized for 24 hr. To prepare the PLGA-AT2, PLGA-NHS and AT2 were dissolved in DCM and stirred magnetically overnight at room temperature. After 24 hr, the methanol/ethyl-ether co-solvent was added, and the precipitate was lyophilized.

Targeted nanoparticles (TNP) and non-targeted nanoparticles (NP) were prepared using the O/W emulsion method. PLGA-NHS, PLGA-AT2, and Navi were used to prepare TNP, while PLGA-NHS and navitoclax were dissolved in DCM for non-targeted NP. The DCM solution was added dropwise into PVA (1%) at high steering speeds. The reaction mixture was incubated

overnight at room temperature. The sample was then centrifuged for 30 min at 3900 RPM to separate the dispersed and continuous phases. Then, the supernatant was removed, followed by lyophilizing the particle under high vacuum for 24-48 hr, and characterized by measuring particle size and zeta potential values. For biodistribution, RhB fluorescent dye was conjugated with PLGA and PLGA-AT2 to produce NP/RhB and TNP/RhB nanoparticles following the same method.

2.2.3. Particle characterization (Size distribution, zeta Potential)

The size and zeta potential of nanoparticles were characterized using a Zetasizer Nano ZS (Malvern Instruments, UK). The size of PLGA nanoparticles was measured by dynamic light scattering (DLS) at 25 °C temperature and a 173° scattering angle. Zeta potential measurements were performed at 25 °C after diluting the samples to 1 mg/mL in deionized water. The stability, size, and zeta potential of each nanoparticle were assessed for up to 6 hr. Scanning electron microscopy (SEM) and nuclear magnetic resonance (NMR) were also performed to examine the particles and confirm conjugation.

2.2.4. Loading content and in-vitro Release study

Navi drug loading and entrapment efficiencies of the targeted and non-targeted NPs were determined directly by quantifying loaded Navi amount in the NPs by a UV-visible spectrophotometer at $\lambda_{\max} - 345$ nm following the equation of previously published article [67]

$$\text{Drug loading \%} \left(\frac{w}{w} \right) = \frac{\text{mass of drug in nanoparticle}}{\text{mass of nanoparticles}} \times 100\%$$

Entrapment efficiency (EE) of Navi (%)

$$= \frac{\text{Initial amount of Navi used} - \text{amount of Navi in supernatant}}{\text{Initial amount of Navi used}} \times 100$$

In vitro release was studied using dialysis against PBS. Briefly, free Navi, NP/Navi, and TNP/Navi were taken into a 15 kDa dialysis bag individually and a continuous stirring at 100 RPM. 2mg of Navi was in each formulation. 1 mL of solution was collected from the outer phase every on 1, 2, 4, 6, 8, 10 and 12 hr and the same volume of PBS was added to maintain the volume. The release amount of Navi was quantified by measuring the absorbance at the wavelength of 345 nm by a UV–visible spectrophotometer (UV-2800, Shimadzu) [67].

2.2.5. Docking Calculations and Molecular Dynamics Simulations.

In computational studies, we investigated the binding of RVYIHPI peptide sequence with Angiotensin II Receptor Type-1 (AGTR1) protein. The structure of the peptide sequence was extracted from the AlphaFold [68] predicted structure of an uncharacterized protein (A0A078AK97) of 1106 amino acids which contained this sequence, obtained by conducting a peptide search with the help of UniProt database [69]. The confidence level for the structure prediction of these residues was medium (pLDDT score between 70-80). The structure of the AGTR1 protein was also extracted from AlphaFold (P30556). The pLDDT score was between 70-90 signifying high and very high confidence in model prediction for this protein structure. We compared this AlphaFold predicted structure with the crystal structure of synthetic nanobody-stabilized angiotensin II type 1 receptor bound to TRV023 (6OS1). We adopted the AlphaFold structure for our docking purposes because it aligned well with the sequence of the crystal structure, and it had no missing residues. Since the C terminus residues (319 to 359) on the intracellular side of the protein, were predicted to be a long and unstructured coil, we removed them from the AGTR1 protein.

After the preparation of the peptide and AGTR1 structures, docking calculations were performed using the AutoDock Vina software [70] and our automated approach was implemented through a custom Linux shell script (available through <https://github.com/vukoviclab/docking-scan>), reported elsewhere [71]. In the molecular docking calculations, a grid box was systematically positioned at various positions on a grid, scanning the protein surface. The scanning grid had box center x-, y- and z-coordinates changed from -33.8 to 18.2 Å, -50.6 to -7.3 Å and -8.5 to 68.6 Å. Each grid box dimension was $2 \times 2 \times 2$ nm³ with an interval of 5 nm with a default spacing and exhaustiveness of 0.0375 nm and 8, respectively. Our procedure ranked the locations of the peptide ligands on the AGTR1 protein surface with different docking scores signifying the binding strengths of each pose.

To obtain the best binding poses with the highest negative binding scores, we analyzed those ligand docking poses acquired through AutoDock Vina which had a binding score more negative or equal to -8.0 kcal/mol. We only selected the docking pose where the peptide was docked near the N-terminus of the protein, which is a part of the AGTR1 extracellular domain [72] in agreement with the experiments which designed the peptide to target the extracellular side of AGTR1, as the initial configuration for the ensuing molecular dynamics (MD) simulations. This pose had the highest negative docking score of -8.6 kcal/mol indicating highest binding affinity between the peptide and the protein in this pose. The modeled peptide-AGTR1 complex system was placed in a 1,2-Didecanoyl-sn-glycero-3-phosphocholine (DDPC) bilayer membrane, built with CHARMM-GUI membrane builder [73] and CHARMM36 topology [74]. The bilayer was built in a rectangular box with 116 lipid molecules in the upper leaflet and 114 lipid molecules in the lower leaflet, and 16,065 TIP3P water molecules, distributed equally between the two layers. The system was neutralized with sodium and chloride ions.

The simulations of the solvated peptide-AGTR1 complex in the DDPC membrane were performed with NAMD2.13 package [75] and CHARMM36 forcefield parameters [76,77]. All simulations were conducted with Langevin dynamics in the NpT ensemble, where the value of the Langevin constant γ_{Lang} was set to 1.0 ps^{-1} , the pressure remained constant at 1 bar, and the temperature remained constant at either 298 K. The long-range Coulomb interactions were calculated every two-time step, using the Particle Mesh Ewald (PME) method [42], with periodic boundary conditions applied in all directions. After 5,000 steps of minimization, solvent molecules were equilibrated for 1 ns while the atoms of this protein-peptide complex were restrained using harmonic forces with a spring constant of $1 \text{ kcal}/(\text{mol} \cdot \text{\AA}^2)$. Next, the system was equilibrated in a 400 ns long production MD run, with harmonic restraints applied on a central heavy atom of the protein with a spring constant of $1 \text{ kcal}/(\text{mol} \cdot \text{\AA}^2)$. The three orthogonal dimensions of the periodic cell were allowed to fluctuate independently while keeping the ratio of the unit cell in the x-y plane constant.

2.2.5.1. Binding energy calculations.

The relative binding free energies between RVYIHPI and AGTR1 were calculated using the Molecular Mechanics Generalized Born-surface Area (MMGB-SA) [43] method over time with the trajectory obtained from our MD production run. The following equation was used to calculate the individual free energies of the extracted configurations of the protein, the peptide, and the complex:

$$G_{tot} = E_{MM} + G_{solv-p} + G_{solv-np} - T\Delta S_{conf},$$

where, E_{MM} , G_{solv-p} , $G_{solv-np}$, ΔS_{conf} respectively represent the summation of the bonded and the Lennard-Jones energy terms, the polar contribution of the solvation energy, the nonpolar contribution of the solvation energy, and the entropy of conformation. NAMD2.13

package generalized Born implicit solvent model [44] was used to calculate all the above terms, except ΔS_{conf} as the contribution of conformational entropy term was neglected. The dielectric constant of the solvent for these calculations was taken to be 78.5. The relative binding free energy was finally calculated as:

$$G_{MMGB-SA} = G_{tot}(\text{complex}) - G_{tot}(\text{protein}) - G_{tot}(\text{peptide}).$$

2.2.5.2. Residue-residue interaction analysis.

The interactions between residues of the protein and the residues of the peptide were studied with the help of a LIGPLOT program [78] for the initial and final configurations of the system. The initial configuration refers to the structure obtained from the docking calculation, and the final configuration refers to the structure obtained after a 400 ns equilibration in MD simulations.

2.2.5.3. Electrostatic interaction analysis.

The electrostatic potential surfaces of AGTR1 were analyzed using APBS (Adaptive Poisson-Boltzmann Solver), [79] and the APBS electrostatics plugin from VMD, for the last configuration of the system in the MD trajectory.

2.2.6. Surface plasmon resonance (SPR) analysis

To assess the binding affinities between AT2 protein and AT2 peptide, binding analysis was performed using the iMSPR-mini (iCLUEBIO, Korea) at 25 °C. TNPs were drop-cast onto the gold sensor chip at a concentration of 50 µg/mL. AT2 and Collagen 1 proteins were then dissolved in PBS and injected over the AT2 peptide-attached gold chip to record resonance

changes and assess the binding affinity. PBS (pH 7.4) was used as the negative control. Response curves were collected using iMSPR Software for protein-peptide binding affinity analysis.

2.2.7. Cell culture and nanoparticle uptake

The rat renal fibroblast cell line (NRK-49F) was used for in vitro cellular uptake studies. The cells were cultured at 37 °C in a humidified atmosphere containing CO₂ (5%) in DMEM medium with FBS (10%) and penicillin (1%). The cells were grown as a monolayer and harvested with EDTA solution (0.25%), followed by seeding 1000 cells in a 24 well plate. The following day, the complete media was replaced with serum-free media containing 10 µg/mL TGFβ-1 (transforming growth factor beta) (R&D System, Minneapolis, MN, USA) to activate the process of converting the fibroblasts into myofibroblasts.

After 24 hour incubation with TGFβ-1, 20 µL of NP/RhB and TNP/RhB (0.5 mg/mL) were added to the wells and incubated for 4 hr. After incubation, Hoechst dye was added to stain the nuclei and the cells were incubated in the dark for another 40 min. The medium was then aspirated from the wells, and the cells were washed three times with cold PBS (pH 7.4). Images were then taken with a DM660 Leica microscope (Leica Microsystem, Deerfield, IL, USA).

2.2.8. Immunocytochemistry

Cells were grown around 70-80% confluency on coverslips and incubated overnight in serum-depleted medium and then treated with TGF-β1 (10 ng/mL) and all the treatments (NP, TNP, NTP/Navi, TNP/Navi, Fausidil) for 24 hr. Next day after washing with cold PBS. Paraformaldehyde (4 %) was added for 10 min for fixation. Then the cells were permeabilized with Triton-X100 (0.1 %) in PBS for 10 min at room temperature and then blocked with BSA (2 %) in PBST to block non-specific binding for 1 hr. The samples were incubated at 4°C for overnight with 1:500 diluted rabbit anti-α-SMA antibodies. After one wash with PBS, the samples

were incubated with 1:100 diluted FITC-conjugated goat antirabbit IgG antibodies (Abclonal, (Woburn, MA) for 1 hr at room temperature. Then washed with PBS, (DAPI). DAPI-positive and α -SMA-positive cells were counted in the slide at three randomly chosen regions under a DM660 Leica microscope (Leica Microsystem, Deerfield, IL, USA).

2.2.9. In-vivo mice model preparation

Six to seven-week-old C57BL/6 mice (21–25 g) were purchased from Jackson Laboratory (Bar Harbor, ME, USA) and maintained under specific pathogen-free conditions. All experiments were performed with approval from the Institutional Animal Care and Use Committee (IACUC) of the University of Texas at El Paso (protocol # A-201920-1). A single dose of 250 mg/kg folic acid was injected intraperitoneally (IP) to develop a mouse model of kidney fibrosis according to a previously published article [80]. The mice were divided into 6 groups: Healthy, Untreated, oral Navitoclax, Fasudil, TNP/Navi, NP/Navi. Fifteen days after the folic acid injection, the treatment began in different groups on every 5th day. After the 3rd treatment, we waited for 5 days, and the mice were sacrificed. Organs and blood were collected for further analysis. Immediately after collection one kidney from each group was frozen for primary cell isolation, western blot, and qPCR analysis.

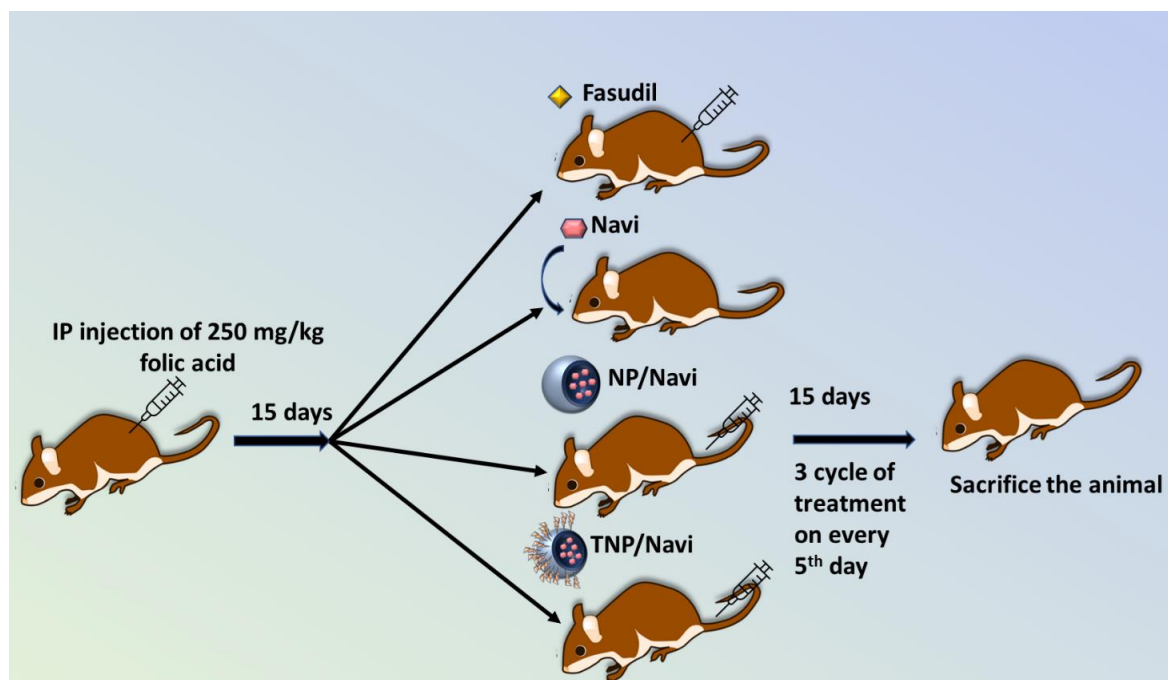


Figure 2: Kidney fibrosis animal model preparation. Schematic representation of kidney fibrosis model preparation and treatment. The image of rat was retrieved from Chemdraw.

2.2.10. *In vivo* bio-distribution and nanoparticle targeting

To examine the kidney properties and biodistribution of nanoparticles, both NP and TNP were labeled with RhB fluorescent dye. Fluorescence distribution was observed using an IVIS® Spectrum (PerkinElmer, Waltham, MA, USA) and Quantum FX (Perkin Elmer, Waltham, MA, USA) for co-registering functional optical signals with anatomical μ CT. NP/RhB and TNP/RhB were dissolved in PBS and injected intravenously into the mouse tail vein at a dose of 1 mg/kg. Mice were anesthetized with isoflurane throughout the imaging procedure. 2D/3D fluorescence imaging and μ CT scans were performed before injection and at 3, 6, and 24 hr post-injection. All images were generated using the Living Image® 4.3.1 software (PerkinElmer, Waltham, MA, USA).

Ex-vivo image of kidney was taken to examine the targeting ability of TNP in fibrosed kidney compared to healthy. NP/RhB and TNP/RhB were administered intravenously via tail vein and animals were sacrificed after 4 hr. The kidney was collected and immediately was subjected to image using a ChemiDoc imaging System. A healthy control without any treatment was used as a negative control. The images were analyzed using ImageJ software.

2.2.11. Therapeutic efficacy of PLGA-NPs in the kidney fibrosis mice model

In the established folic acid induced chronic kidney fibrosis model, mice were divided into 6 treatment groups: healthy, untreated, Fasudil, Navi (PO), NP/Navi, and TNP/Navi. The dose of Navi in the groups with free oral Navi and intravenous PLGA NPs was 10 mg/kg. Fasudil was administered via intraperitoneal injection at a dose of 10 mg/kg. Five days after the final treatment, animals were sacrificed, and organs and blood were collected for further analysis. Kidney size was measured using a digital slide caliper. Kidney weight was also measured.

2.2.12. Histology and immunohistochemical staining

Tissue processing was performed using an auto processor (Thermo Scientific Spin Tissue Processor Microtome STP-120). Tissues were dehydrated using different concentrations (70%, 95%, and 100%) of histologically graded ethanol (Fisher Scientific, USA) and then submerged in xylene and infiltrated with paraffin. Paraffin-embedded tissues were sectioned (6 μm) onto Super Frost Plus slides using a Shandon Finesse E/ME microtome. Slides were air-dried for 2 days before staining. Tissue sections were deparaffinized and stained with hematoxylin and eosin. Masson's trichrome staining was also performed using a Masson's Trichrome Staining Kit (Abcam, Cambridge, UK) to visualize the fibrotic area. All procedures were performed according to a previously published protocol [81]. Images were obtained using a MoticEasyScan One slide scanner (Motic Digital Pathology, USA). Immunohistochemistry for α -SMA and CTGF was

performed using anti-rabbit polyclonal α -SMA antibody (Abclonal, USA) and anti-CTGF rabbit polyclonal antibody (Abclonal, USA). All sections were mounted using Cytoseal 60 (ThermoFisher Scientific, USA)

2.2.13. Immunofluorescence

For IFC, sectioned tissue was deparaffinized and rehydrated. Then, antigen unmasking with boiled 1 mM EDTA solution the section was then washed and then permeabilized by incubating the sections in PBS supplemented with 0.2% Triton X-100 (Sigma-Aldrich) for 45 min. Kidney sections were also used for IFC staining to detect the expression of extracellular matrix proteins. The sections were incubated with blocking buffer (1%) at room temperature. The sections were then incubated with a fluorescent dye conjugated primary antibody. The antibodies used for IFC were as follows: α -smooth muscle actin (1:100), α -SMA eFlour and FITC-CTGF (1:100) (FabGenX, USA). The following day, the sections were covered with DAPI mounting media (Abcam, Cambridge, UK). The image was taken using a Leica DM600 microscope. All images were analyzed using ImageJ software.

2.2.14. Western blot analysis

To examine the expression of α -SMA, CTGF, and Bcl-2, proteins were extracted from tissues and underwent western blot analysis as previously described [67]. For in-vitro western blotting analysis NRK-49F cells were cultured in a 6 well plate and treatment were added for 24 hr before the collection of protein. The antibodies used were as follows: anti- α SMA (1:1000), anti-CTGF (1:1000), anti-Bcl2 (1:1000) and anti- α -tubulin (1:2500). WB was performed following the same method as described before [66].

2.2.15. TUNEL assay

TUNEL assay was performed using the Click-iT Plus TUNEL assay kit (Cat #C10625) (ThermoFisher Scientific, Waltham, Massachusetts, USA). The assay was performed according to the manufacturer's instructions.

2.2.16. Blood and serum analysis

Blood was collected in heparinized tubes from the posterior vena cava after sacrifice. Blood samples (500 μ L - 1 mL) were collected from each mouse. Blood samples were analyzed using the DREW HEMAVET instrument. Serum was separated from the blood serum and analyzed using Heska Element DC for liver and kidney toxicity markers.

2.2.17. Hydroxyproline measurement

Total hydroxyproline was measured in the serum collected from different treatment groups using a hydroxyproline assay kit (Cat # 102966-250) (VWR, Atlanta, GA, USA). The assay was performed in accordance with the manufacturer's instructions. The samples were acid hydrolyzed and then cleaned using activated charcoal. After the addition of the substrate, the optical density was measured at 565 nm. The concentration was measured using a calibration curve made with different concentrations of hydroxyproline protein.

2.2.18. Statistical Analysis

Data are presented as mean \pm SD. Statistical analyses were performed using GraphPad Prism version 9 (GraphPad Software, San Diego, CA, USA). Two-sample comparisons were determined using a two-tailed Student t-test. Statistical significance was set at $p < 0.05$.

2.3. RESULTS AND DISCUSSION

2.3.1. Characterization of NPs ideal for targeting diseases specific to the kidney:

Four different PLGA nanoparticles (NPs) were prepared for this study: PLGA NP (NP), AT2 targeted PLGA (TNP), Navi loaded PLGA (NP/Navi), and AT2 peptide linked PLGA NP loaded with Navi (TNP/Navi) (**Fig. 1A**). These NPs were characterized by size and zeta potential. NPs were dissolved and diluted in deionized water for size and zeta potential measurements. Dynamic light scattering (DLS) revealed that the size of the PLGA NPs increased with each added compound.

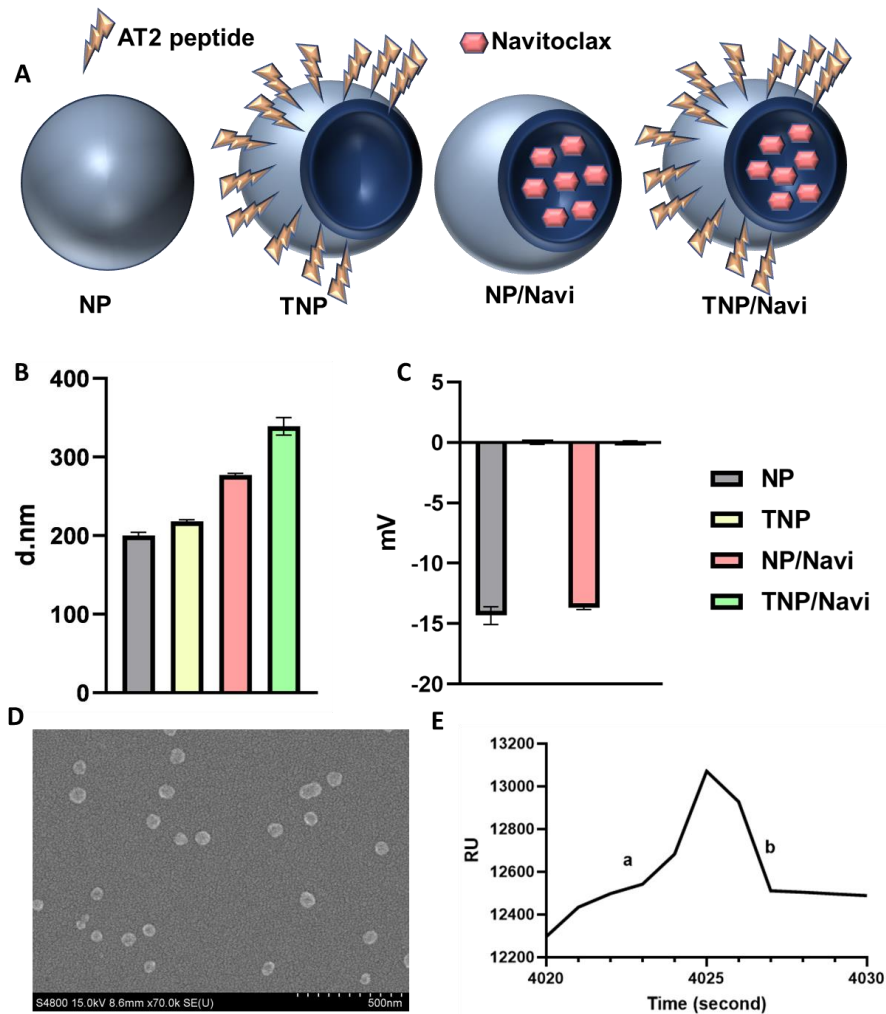


Figure 3: Physical properties of NPs. Schematics of nanoparticles (A). Size and Zeta potential of the nanoparticle particles were measured by Zetasizer (B and C). The average size and zeta of TNP/Navi were 339 d.nm and -11.1333 mV. Whereas size and zeta potential of TNPs were 196.5 nm and -0.123 mV. SEM image of TNP/Navi NPs showed smooth surface (D), and SPR analysis response after running AT2 protein over the TNP liganded chip (E).

The size of the free PLGA NPs were measured as 200 nm in diameter, but their size increased up to 339 nm upon peptide conjugation and Navi loading (TNP/Navi). Similarly, the zeta potential of NPs was measured as -14.33 mV but changed to -0.123 mV upon peptide

conjugation and Navi loading (TNP/Navi) (**Fig. 3B**). The size distribution and zeta potential values demonstrated that particle size increased and negative zeta potential value decreased due to presence of positively charged AT2 peptide and loading of lipophilic small molecule [82]. The changes in size and zeta potential of the particles confirmed the nanoscale size and optimal zeta potential for kidney targeting. The negatively charged glomeruli basement membrane [83] facilitates the transport of the kidney-targeting particle TNP/Navi may triggered by both active targeting and charge-charge interaction, concurrently. Although the glomerulus pore size is approximately ~70 nm, in glomeruli nephropathy, both size and charge are disrupted, allowing particles larger than 1000 nm to penetrate [84]. It has been reported in a previous study that mesoscale PLGA coated with PEG nanoparticle, approximately 400 nm in size, had 7 times higher accumulation in the proximal tubule of the kidney and effectively escaped the reticuloendothelial system. Therefore, the particles created for this study were ideal for targeting diseases specific to kidney. The SEM image confirms the size of the TNP/Navi particles and reveals a smooth surface with spherical shape (**Fig. 3C**). NMR analysis was conducted to confirm chemical conjugation between PLGA and peptide, and the peak shift in the NMR spectrum is an indication conjugation of AT2 peptide and PLGA (**Fig. 3D**). NMR spectra of other particles are presented in the supporting information (**Fig. S1**). The loading content (LC) and loading efficiency (LE) of Navi in TNP/Navi and NP/Navi were calculated as 17.01% and 23.57% and loading efficiency was calculated as 73.95% and 80.4321%, respectively.

Stability of different particles were measured for up to 6 hr in PBS and FBS solution (10%). The size of NPs increased over time because of aggregation (**Fig. S4**). However, the zeta potential value was relatively stable for at least 6 hr, confirming the stability of the TNP/Navi. The cumulative release profile showed that release of Navi from NP/Navi is higher and faster compared

to TNP/Navi observed for up to 8 hr (**Fig. S3**). SPR analysis was performed to measure the targeting ability of the peptide to the AT2 protein and other fibrotic proteins, such as collagen. After injecting the AT2 protein onto the COOH-attached gold chip, an increase in the response from the baseline was observed, confirming the TNP's capacity to bind the AT2 protein (**Fig. 3D**). Collagen 1 also produced a slightly higher response, confirming the targeting NPs (PA) were able to bind with collagen, as shown in **Fig. S2**.

2.3.2. AT2 peptide and protein dynamics modulation shows protein peptide binding

To examine the complex of RVYIHPI peptide bound to AGTR1 and the energetics of their binding, we modeled this complex by molecular docking calculations and then simulated it using molecular dynamics simulations. In experiments, the RVYIHPI peptide would be targeting the extracellular side of the AGTR1 membrane protein. In docking calculations, the RVYIHPI peptide was found to have one primary location for binding to the extracellular side of AGTR1, which is inside the top cavity of AGTR1, as seen in **Fig 4** and **Fig S5**. The most favorable docking score for the peptide is -8.6 kcal/mol.

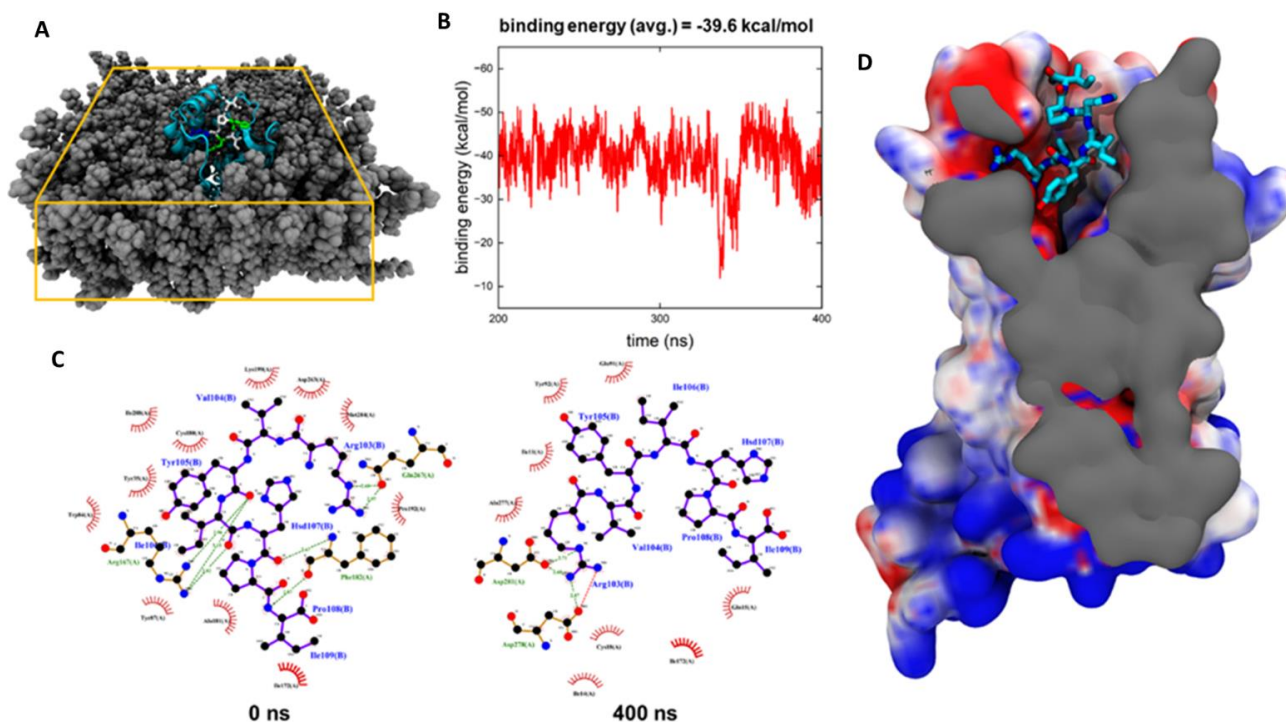


Figure 4: AT2 peptide and protein dynamics modulation. Peptide RVYIHPI interacts and binds strongly to the N-terminus of AGTR1 membrane protein. A) Representative snapshot of the protein-peptide system in the DDPC membrane. The atoms of the membrane bilayer are shown as grey spheres, the AGTR1 protein is shown in cyan, and the peptide is colored according to the types of residues present. White represents non-polar residues; green represents polar residues and blue represents the basic residues. B) Binding energy between RVYIHPI and AGTR1 calculated over time for the 400 ns MD trajectory. The average binding energy was calculated over the last half of trajectory. C) 2D interaction diagram of protein-peptide interaction at the beginning of the simulation and after 400 ns of simulation. The peptide residues are shown using violet bonds whereas the protein residues are in orange. C, N and O atoms are shown as black, blue and red circles. Hydrogen atoms have been omitted for clarity. The polar interactions between peptide and protein residues are shown using green dotted lines with a labeling of inter-heavy atom distance involved in polar interaction. The protein residues having non-polar

interaction are depicted using semi dark red semi circles. **D)** Surface electrostatic potential of the AGTR1 protein calculated using the APBS tool. The positively charged surface is shown in blue while the negatively charged surface is in red. The peptide in the binding pocket is colored according to the atom type: cyan (C), blue (N), and red (O). Hydrogen atoms are not shown for clarity. For better visualization of the peptide in the cavity, the front part of the protein has been removed and the cutting plane is colored in gray.

The complex of RVYIHPI peptide bound to AGTR1 was then embedded in a DDPC membrane and simulated for 400 ns, as described in the Methods. During the equilibration simulation, the peptide adjusted inside the binding cavity of AGTR1. The simulations reveal the average binding free energy of the peptide RVYIHPI to the AGTR1 protein as -39.6 kcal/mol (**Fig 4B**). The specific interactions involved between the residues of the protein and the peptide have been examined with LIGPLOT. **Fig 4C** shows that in the initial configuration there are several hydrogen bonding interactions between the residues Arg167, Phe182, Gln267 of AGTR1 and residues Tyr105, Ile106, Pro108, Hsd107 and Arg103 of the peptide. There are also points of hydrophobic contact between several residues of AGTR1 as shown by the red spoked arcs including Trp84, Tyr35, Pro192, etc., and the peptide. After 400 ns simulation, the final peptide: AGTR1 configuration shows hydrogen bonding interactions between Asp281, Asp278 of AGTR1 with Arg103 of the peptide. There are also several protein residues like Ala277, Cys18, Gln15 which have hydrophobic contacts with the peptide. There is a salt bridge formation between Asp278 and Arg103 as indicated by the red dotted bond. Although, the overall number of hydrogen bonding interactions decreases as the simulation progresses from 0 ns to 400 ns, the peptide rearranges itself so that Arg103 of peptide can maximize its interaction with the negatively charged binding pocket of the protein (Asp278 and Asp281). Also, Ile109 finds the slightly positively

charged pocket of AGTR1, shown in **Fig 4D**. These stabilizing electrostatic interactions favor the strong binding interaction between peptide RVYIHPI and protein AGTR1.

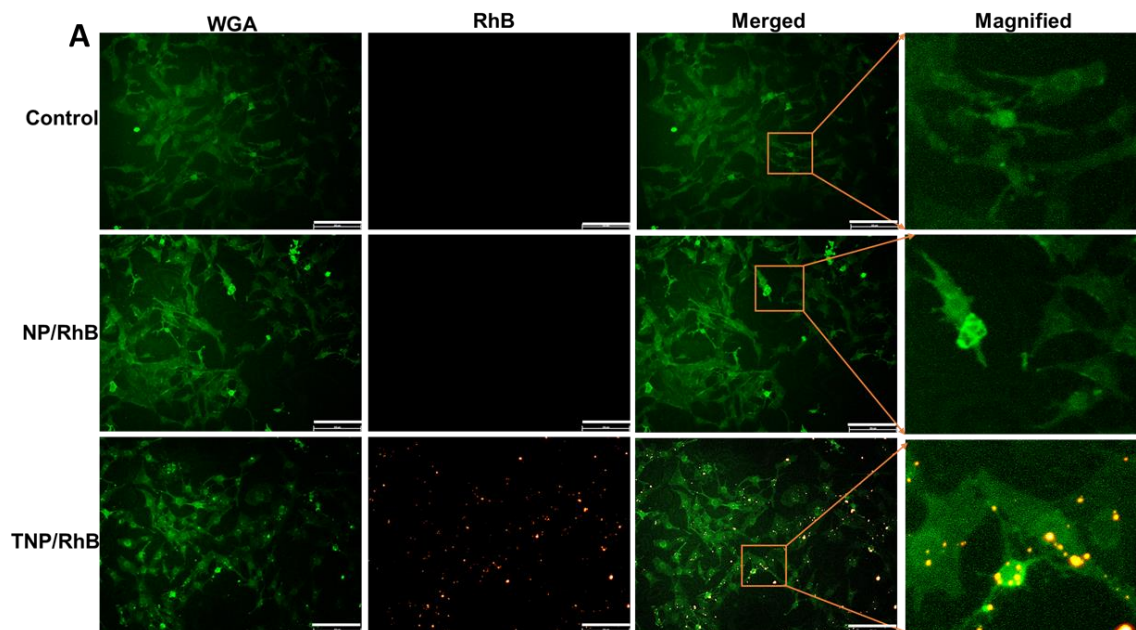


Figure 5: Cellular uptake of targeted NPs and Bcl2 inhibition. NPs uptake by NRK-49F cell line with TGF β -1. NP/RhB and TNP/RhB were added after 24 hr incubation of TGF β -1. Four hours after incubation with NP and TNP it was observed that TNP uptake was higher in the myofibroblast. Whereas no nanoparticle was up taken by the cells with NP/RhB. The scale bar represents 200 μ m (A).

2.3.3. In-vitro myofibroblasts promote accumulation of targeted NPs:

NRK-49F cells were treated with TGF β -1 to convert fibroblasts into myofibroblasts. Bright field images of cells were taken before and after adding the TGF β -1 (**Fig. S6**). Cells became slender after adding TGF β -1, confirming the conversion of myofibroblasts. Healthy fibroblasts typically present in all tissues and help in wound healing. Exposure to cytokines such as IL-1 and

IL-8 due to injury can activate fibroblasts into myoblasts, initiating the fibrosis process. Certain proteins, such as AT2, α -SMA, and VCAM1 are overexpressed in myofibroblasts [85,86]. To confirm the uptake of nanoparticles, RhB labeled PLGA (non-targeting) and TNP/RhB were added to the cells after TGF β -1 treatment, and the targeted nanoparticles showed higher accumulation in the cells (**Fig. 5A**).

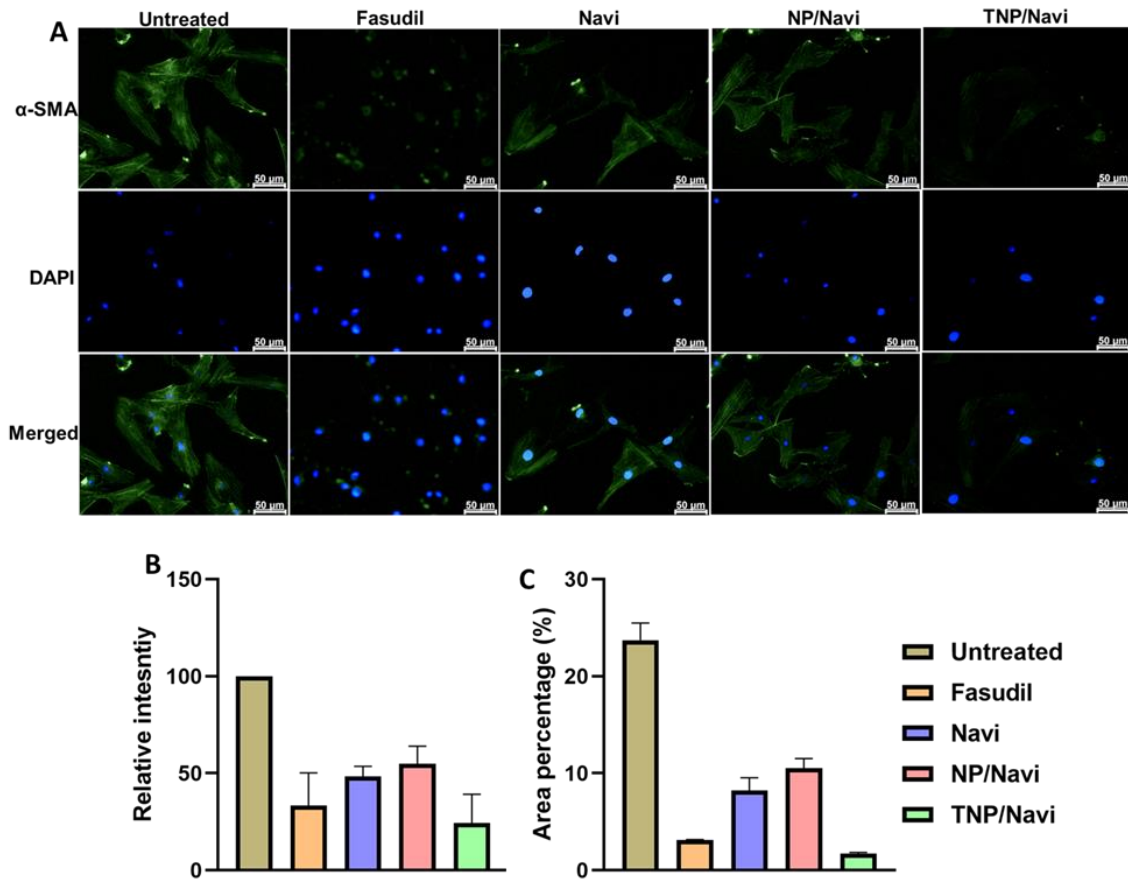


Figure 6; *In vitro* therapeutic effects. α -SMA expression of untreated and treated cell with Fasudil, Navi, NP/Navi, and TNP/Navi (A). The image shows reduced expression of α -SMA with the treatment group. Scale bar represents 50 mm. The images were quantified in ImageJ and the graph represents the relative intensity (B) and area% (C). In both parameters, α -SMA reduced the most in TNP/Navi group.

2.3.4. In-vitro therapeutic efficacy for α -SMA shows reduction of α -SMA in TNP/Navi group

In-vitro therapeutic efficacy was measured by immunocytochemistry for α -SMA. Myofibroblast is a contractile fusiform cell with α -SMA, which is responsible for the multiple physiological process like wound healing and fibrosis [87,88]. In response to tissue injury fibroblast migrates to the injured cite and transform into myofibroblast and produce α -SMA and stress fibroblast [89]. Hence, α -SMA is considered as one of the reliable and significant markers for myofibroblast as well as fibrosis. The immunocytochemistry results showed that TGF- β increased the production of α -SMA in untreated cells whereas, after treatment the α -SMA significantly reduced (P value 0.0001) especially with Fasudil (P value 0.0064) and TNP/Navi (P value 0.0034). The image was quantified both in terms of intensity and area % (**Fig. 6**).

2.3.5. Biodistribution of PLGA NPs

We investigated the targeting ability and biodistribution of AT2 conjugated PLGA NPs in live mice using IVIS and CT co-registration. RhB conjugated PLGA without any targeting peptide was used as a control. Both the particles were used in 1mg/kg concentration. Significant accumulation of TNP/RhB in the kidney was observed 3 hr after administration (**Fig. 7B**) Although there were still nanoparticles in the kidney 6 hr post administration, few NPs were observed in other major organs such as the liver, lungs, and heart. After 24 hr post injection, TNP particles remained in the kidney, while NPs from other organs were cleared. A 3D rotating image is provided in the supplementary section (PPT).

To measure the selective nanoparticle accumulation in kidney, ex-vivo image of the excised kidney was taken (**Fig. 7B**). It showed 66.01% higher accumulation of TNP (80.24%) in fibrosed kidney than in healthy kidney (14.23%). In fibrosed kidney 43.75% more accumulation

of TNP was observed than non-targeting particles (36.49%), which confirms the targeting ability of the TNP in fibrosed kidney (**Fig. 7C, and Fig. 7D**).

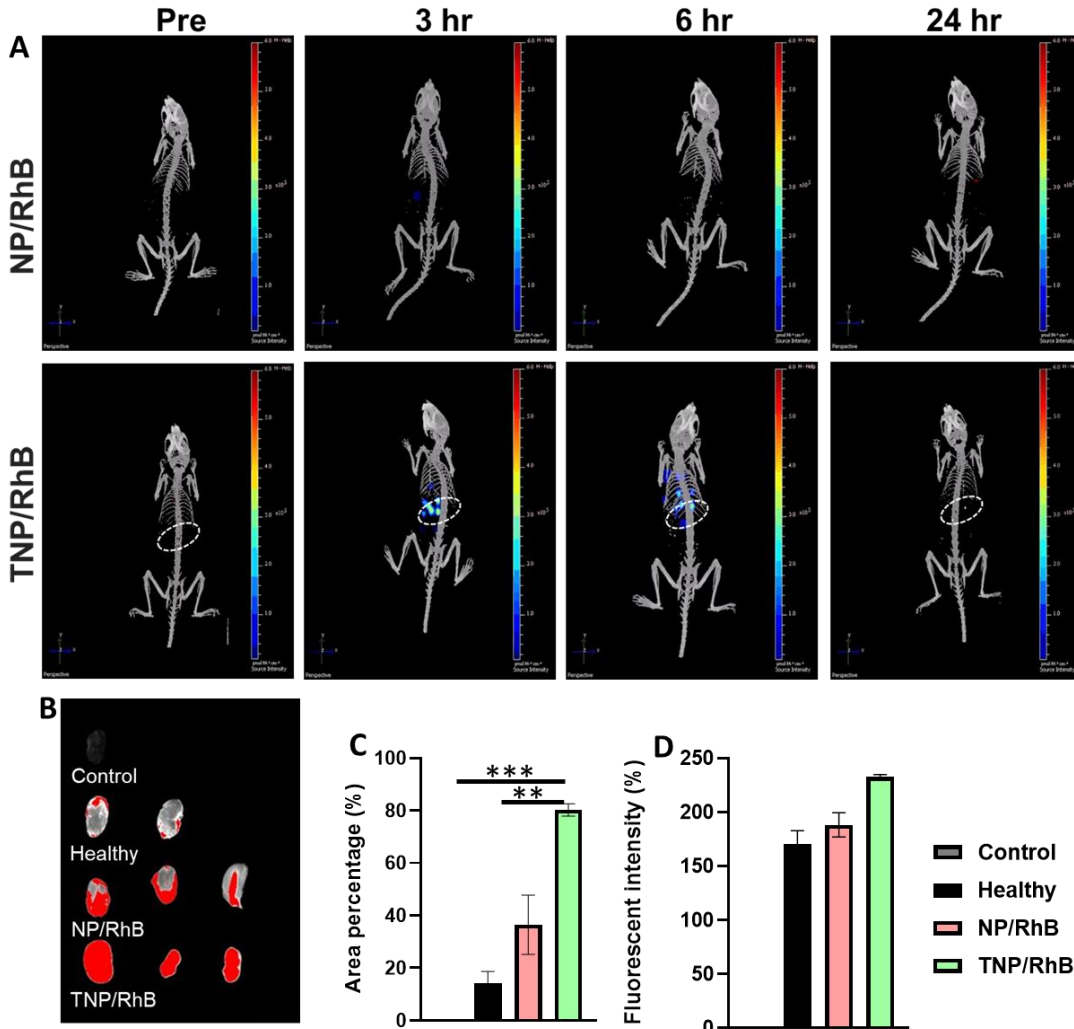


Figure 7: In-vivo biodistribution of the NPs. Biodistribution was observed for 24 hr post-administration of the targeted and non-targeted NPs via tail vein. The AT2 conjugated PLGA nanoparticle attached with RhB (TNP/RhB) dye showed kidney targeting ability and mostly accumulated in the kidney for at least 24 hr. Kidney regions are indicated in white dash in the TNP group. Other than liver no signal was captured with non-targeted NP/RhB particles. Ex vivo

nanoparticle uptake in healthy and fibrosed kidneys were measured. Representative ex-vivo images of healthy and fibrosed kidney after treatment with NP/RhB and TNP/RhB. Healthy control without any treatment was used as negative control (control). Healthy represents healthy treated with TNP/RhB, NP/RhB group represents fibrosed kidney treated with NP/RhB, and TNP/RhB represents fibrosed kidney with TNP/RhB. The image shows higher accumulation of targeted particles in fibrosed kidney both in terms of area percentage (B) and fluorescent intensity (C).

2.3.6. Therapeutic efficacy of PLGA NPs

After observing the high accumulation of TNP in the kidney, we began investigating the therapeutic efficacy using kidney fibrosis model developed in C57BL/6 mice. The mice were weighed and divided into 6 groups (healthy control, untreated disease control, Navi (PO), Fasudil (IP), NP/Navi (IV), and TNP/Navi (IV)). Treatments were started at 15 days after the fibrosis induction and involved 3 cycles. Each treatment modalities were administered every 5th days. Five days after the last treatment, the kidneys were harvested to measure their size and weight. We have observed that the size and weight of kidneys were significantly decreased after treatment with (p < 0.0005) in the untreated group, increased. In chronic kidney disease, kidney size is reduced due to damaged nephrons (**Fig. 8C, and Fig. 8D**) [90]. The fibrosis process, which heals damaged nephrons in the kidney, cause organ shrinkage, a phenotypic indication of fibrosis development [90,91].

Body weights of the mice were also measured to monitor toxicity of the therapeutics modalities. The body weights of untreated mice significantly increased after the end of the treatment. However, in the treatment group, weight initially decreased during the middle of the treatment but then increased following TNP/Navi and NP/Navi treatment. Healthy mice

experienced consistent weight gain. With Navi (PO) and Fasudil (IV), weight reduction persisted throughout the treatment, possibly due to toxicity or treatment ineffectiveness. Body weights of untreated mice were higher than that of mice in the treatment groups (**Fig. 8B**).

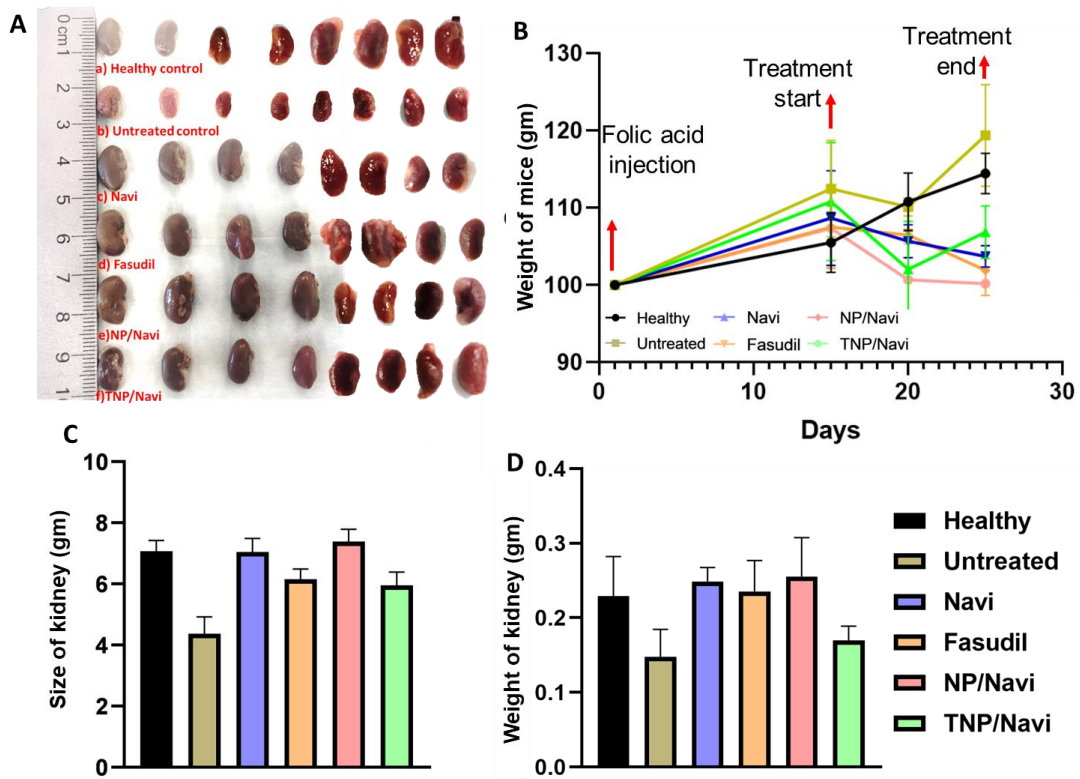


Figure 8: Size and weight of the harvested kidney. Image of the harvested kidneys (A). Size and weight (C) and (D) of kidneys in different treatment groups were measured after sacrifice. The size of the untreated kidney shrunk by 38.20% (p value 0.0001) than healthy control (A). After treatment with Navitoclax (Navi), Fasudil, NP/Navi, and TNP/Navi, kidney sizes increased up to 26.66% with TNP/Navi. Weight of the mice (B) before and during the treatment.

Kidney failure can lead to the accumulation of excess fluid in the body, a condition known as edema, which may have contributed to the observed weight gain in mice [92]. Edema occurs

during kidney damage due to sodium retention and reduction of protein levels in the blood. In kidney damage, the pores of glomeruli change, allowing proteins to pass through, resulting in hypoproteinemia in the blood [93]. Lower protein levels cause low capillary colloidal pressure, resulting in low circulatory volume. As a defense mechanism to maintain blood circulation in the vital organs, the kidneys increase the circulatory volume by retaining sodium and water, which can lead to edema. Edema in chronic kidney disease often begins with the face and legs before progressing to ascites (abdominal cavity) [94,95]. In the untreated mouse serum, the total protein level was found to be 2.3 g/dL, lower than the reference range (5-8 g/dL), which explains the weight gain in mouse model.

2.3.7. Reversal of fibrosis and pro-fibrotic protein expression with TNP/Navi

In kidney fibrosis, there is an excessive accumulation of extracellular matrix proteins such as α -SMA, CTGF, collagen 1, and hydroxyproline. To assess the therapeutic effect of treatment, tissue sections were stained with Masson's trichrome (MT) stained to visualize the collagen/fibrotic areas in the tissue. During MT staining, fibrotic areas or collagen in the kidney appeared blue, while other regions were red/pink in color (**Fig. 9A**). The untreated kidney section exhibited a larger blue region compared to the healthy group, which appeared to decrease after treatment. After staining, images were taken at 8X magnification and analyzed with ImageJ software to represent the quantitative data. For quantitative measurement, whole tissue sections were analyzed to avoid bias. It was observed that untreated kidney sections had the highest collagen accumulation or large fibrotic area. In untreated group the fibrotic area percentage was $51.72 \pm 0.41\%$ (**Fig. 9C**). Fibrosis was reduced with treatment. In the TNP/Navi treatment group, the fibrotic area was significantly ($p < 0.005$) reduced by 34.23% compared to the untreated group (**Fig. 9A, and Fig. 9B**). Serum hydroxyproline measurement showed a significant reduction in

hydroxyproline after treatment with TNP/Navi compared to untreated cells ($p < 0.0001$) (**Fig. 9C**). Hydroxyproline is an important diagnostic factor for the severity of fibrosis and plays a crucial role in the synthesis of collagen [96,97]. The reduction in hydroxyproline levels indicates that the TNP has the ability of fibrosis treatment in kidney.

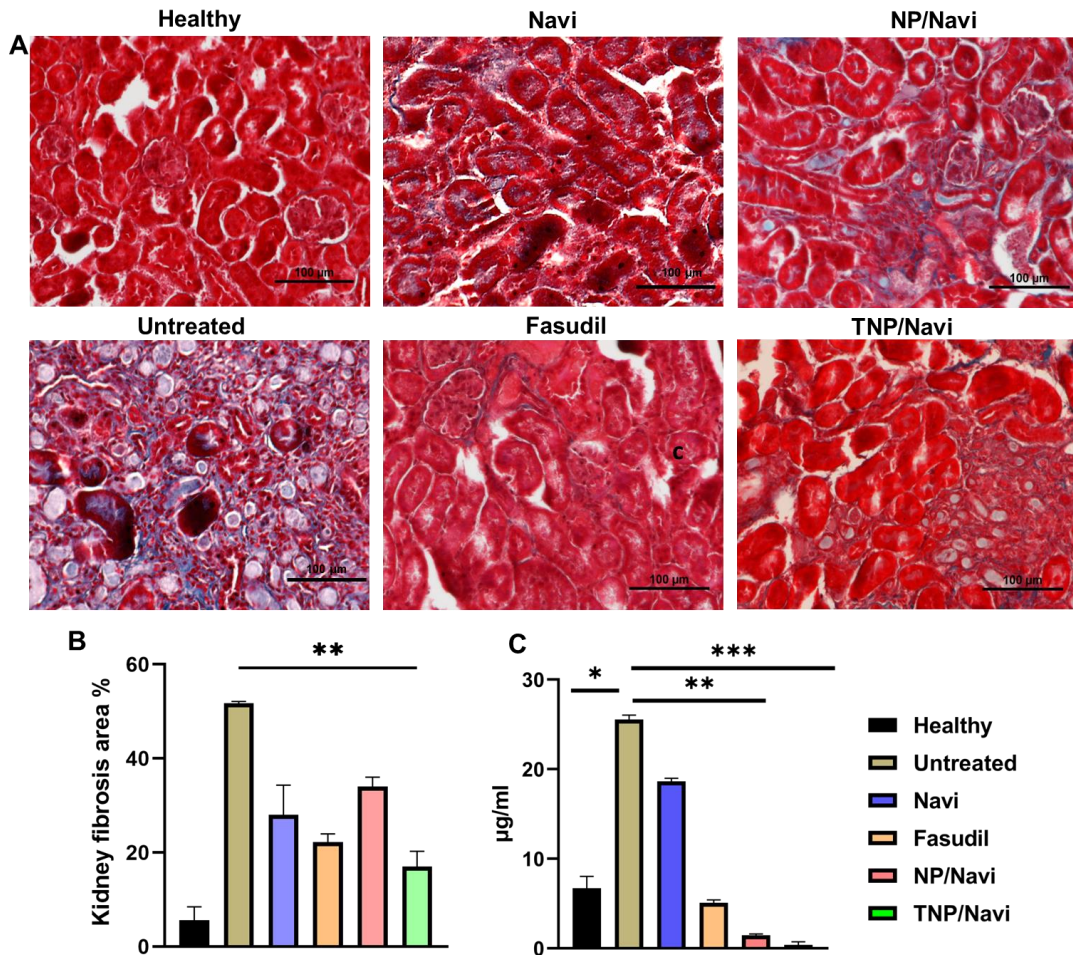


Figure 9: Masson's Trichrome staining of the kidney section. Masson's Trichrome staining of the kidney section in 8X magnification. Scale bar represents 100 µm. The image indicated reduction of fibrosis with the treatment specifically with Fasudil, NP/Navi and TNP/Navi (A). (B) quantitative representation of fibrosis in the kidney section. Error bar represented SD and scale bar represented 100 µm. Hydroxyproline measurement from mice serum showed higher level of

*hydroxyproline in untreated group which got decreased by the treatment group specifically with Fasudil, NP/Navi and TNP/Navi (C). P-value *indicated <0.05, ** indicated <0.001, and *** indicated <0.0001.*

Other fibrotic proteins such as α -SMA and CTGF, were measured by immunofluorescence (**Fig. 10A**). A higher intensity (arbitrary unit) of CTGF was observed in the untreated group (79.8 ± 3.76) which decreased with treatment (**Fig. 10F**). More specifically, treatment with TNP/Navi particles resulted in a CTGF expression level close to that of healthy controls. An increased α -SMA level was observed in the untreated group (9.18 ± 0.46 arbitrary unit) compared to control and decreased following treatment. No fluorescent signal for α -SMA was detected with NP/Navi and TNP/Navi treatment group. The red arrow indicates the green CTGF region, and the yellow arrow indicates red α -SMA. Images were taken at 10X magnification, with the scale bar representing 100 μ m. Western blot data of α -SMA and CTGF also supports the immunofluorescence data. Statistically significant increase in expression of α -SMA ($p < 0.0005$) with untreated from healthy and decrease after treatment with TNP/Navi ($p < 0.005$). CTGF in untreated kidney fibrosis mice also increased but decreased for the mice with treatment.

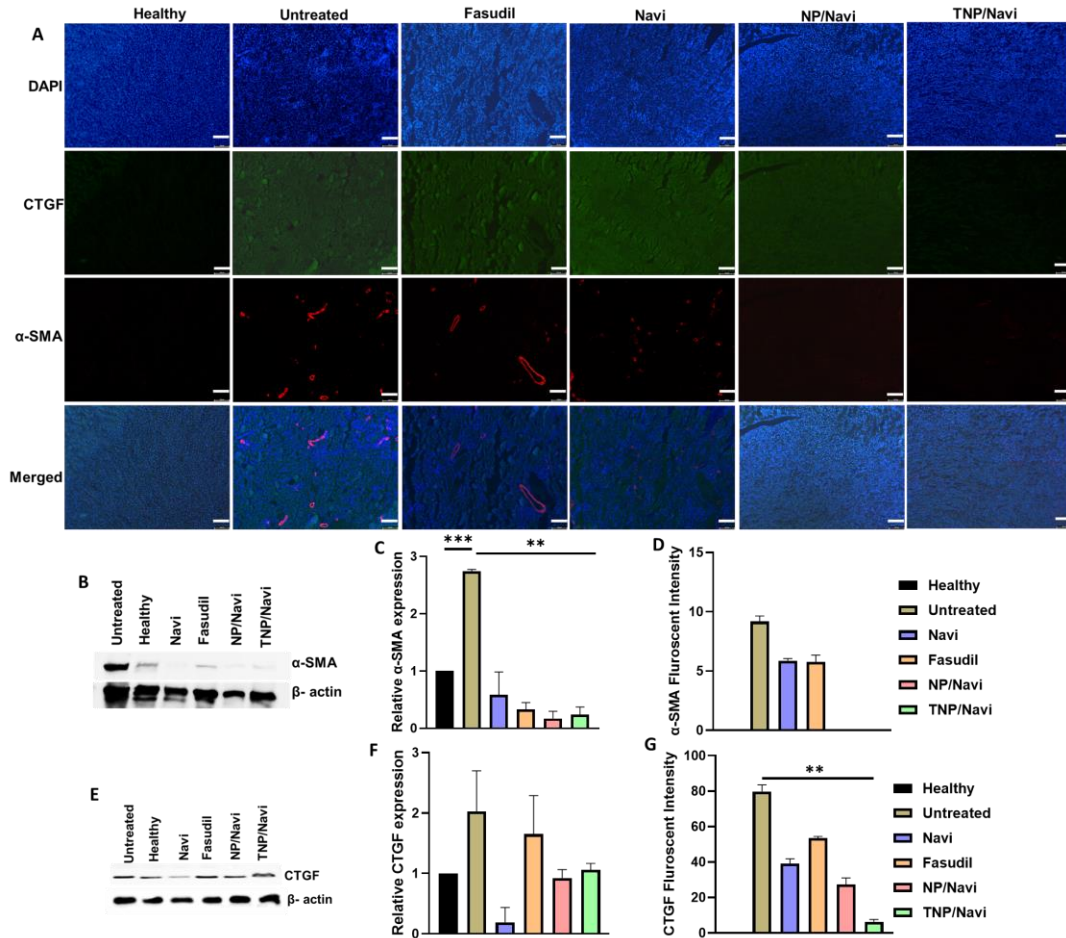


Figure 10: immunofluorescence of kidney sections. Images of kidney sections for CTGF and α -SMA were obtained by direct immunofluorescence (A). The green signal indicates CTGF, and red indicates α -SMA expression. Scale bar represents 100 μ m. Western blot of α -SMA (B) and CTGF (E) was done from the kidney tissue lysate. Quantitative analysis of WB data revealed that untreated kidney tissue had higher expression of both α -SMA (C) and CTGF (F) which reduces with the treatment. (D) and (G) represent the quantitative analysis of α -SMA and CTGF respectively. The error bar represents the SD.

2.3.8. Improvement of kidney morphology and kidney function with TNP/Navi formulation

Kidney morphology was assessed using H&E staining of the paraffin-embedded kidney sections. We observed distorted kidney morphology in the untreated group, accompanied by

increased nuclear infiltration (blue dots) (**Fig. 10A**). In contrast, the healthy group exhibited distinguishable glomeruli (yellow arrow) and tubules (green arrow). After treatment, kidney morphology improved and closely resembled the healthy group, especially with TNP/Navi, where the kidney structure was more visible with less nuclear infiltration.

Serum analysis was performed to evaluate kidney function and systemic toxicity (**Fig. 11B-11H**). Two crucial indicators of kidney dysfunction are creatinine and blood urea nitrogen (BUN). In the untreated group, the creatinine level (**Fig. 11B**) was measured as 1.6 mg/dL, while the creatinine level for a healthy mouse is up to ~1.2 mg/dL [98]. Therefore, a creatinine level greater than 1.2 mg/dL in the untreated mice suggests impaired kidney function. However, treatment with TNP/Navi and NP/Nabi formulation reduced the creatinine level within the normal range (0.3-0.6 mg/dL) confirming the restoration of renal function. BUN levels were also elevated in the untreated group but were decreased upon treatment (**Fig. 11C**). Liver function tests, including total protein (TP), alkaline phosphatase (ALP), and alanine aminotransferase (ALT) were conducted (**Fig. 11D-11F**). TP decreased in the untreated group due to impaired kidney function, where the kidney pore size was large enough to allow proteins to pass through the membrane [94]. Total protein level increased from 2.3 ± 0.51 gm/dL (untreated) to 3.775 ± 0.89 in TNP/Navi group (**Fig. 11D**). No significant changes in platelet and hemoglobin (Hb) level indicates that the treatment did not produce any hematological side effect even though the formulations (TNP and NP) were delivered intravenously. A reduction of Hb level up to 6.77 ± 2.9 mg/dL (**Fig. 11H**) in untreated group was observed but increased with the treatment, confirming anemia, which is a common symptom in kidney fibrosis. Healthy kidney produces erythropoietin (EPO), which stimulates bone marrow to produce blood cells. Kidney fibrosis impairs kidney function, resulting in reduced EPO production and, subsequently, anemia [99]. However, Hb level reached the normal range (10-14

g/dl) upon treatment, indicating therapeutic progress. Systemic presence of Navi results in reduced platelet count by inducing thrombocytopenia [100]. In healthy, Navi, Fasudil, TP/Navi and TNP/Navi group the Hb level was 13.16 ± 1.19 , 10.55 ± 3.61 , 12.75 ± 4.43 , 9.05 ± 2.22 and 14.25 ± 2.19 mg/dL, respectively. The reduced level of Hb in TP/Navi than that of TNP/Navi indicates the off targeting hematological side effect of TP/Navi formulation. Thrombocytopenia was observed for orally administered Navi, whereas TNP/Navi, NP/Navi and Fasudil did not cause thrombocytopenia in the blood (**Fig. 11G**). Platelet count was observed for 6 hours after administration of Navi (PO), NP/Navi (IV) and TNP/Navi (IV). The platelet value decreased in the 1st hour which remained constant with the free Navi than TNP/Navi (**Fig. S6**).

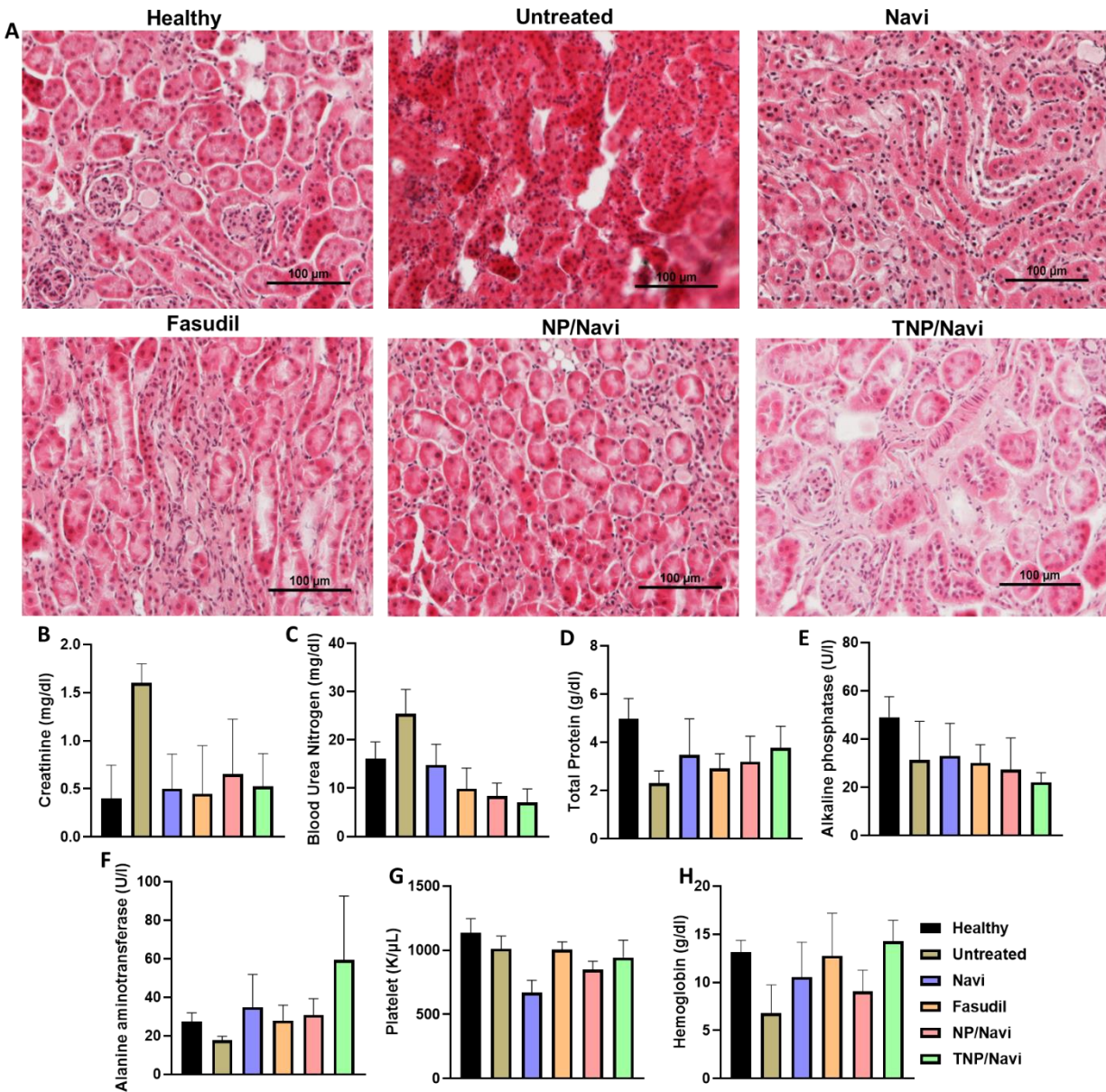


Figure 11: Histology of kidney tissue. H&E staining of kidney sections from different treatment group (A). The untreated kidney section showed damaged renal structure whereas structure improved with the treatment. Serum analysis of kidney function marker Creatinine (B) and Blood urea nitrogen (BUN) (C). High creatinine and BUN level in untreated group indicated the renal dysfunction, which improved with the treatment group. Total protein (D) was less than normal level in untreated group of mice. Alkaline phosphatase (ALP), alanine aminotransferase (ALT)

was in normal range with all the groups (E and F). Blood platelet (G) level was lower than normal range with oral Navi group and normal with other groups. The Hb (H) level was below normal range for the untreated mice which indicates anemia in the untreated kidney fibrosis model.

2.3.9. Navi, NP/Navi, and TNP/Navi treatment results in Bcl2 inhibition and apoptosis

Bcl2 inhibition and apoptosis were assessed using western blotting and TUNEL assay from serum samples and tissue sections from different treatment groups. Reduced Bcl2 expression was observed in WB with Navi, NP/Navi, and TNP/Navi treatment group (**Fig. 12B**). After analyzing the WB data using ImageJ the relative expression in different groups was found to be 0.65 ± 0.13 , 0.56 ± 0.01 , 0.52 ± 0.04 , 0.74 ± 0.17 and 0.44 ± 0.10 in untreated, Navi, Fasudil, NP/Navi and TNP/Navi respectively (**Fig. 12C**). The TUNEL assay was used to measure apoptosis by visualizing the broken nucleus, was performed on tissue sections from kidney. For Navi, NP/Navi, and TNP/Navi, TUNEL-positive cells were $10.49\pm 1.25\%$, $19.55\pm 6.14\%$ and $38.86\pm 4.88\%$ respectively, supporting the western blot data (**Fig. 12A and 12D**). TUNEL assay indicates more apoptosis in Navi treated kidney specifically in TNP/Navi. In TNP/Navi treated group 35.16% more apoptosis ($p < 0.05$) was observed in the TNP/Navi group compared to the untreated mice. The above studies confirmed that free Navi, NP/Navi, and TNP/Navi NPs reduced the expression of Bcl2 protein, inducing apoptosis of fibrotic cells since the particles were targeted to myofibroblasts.

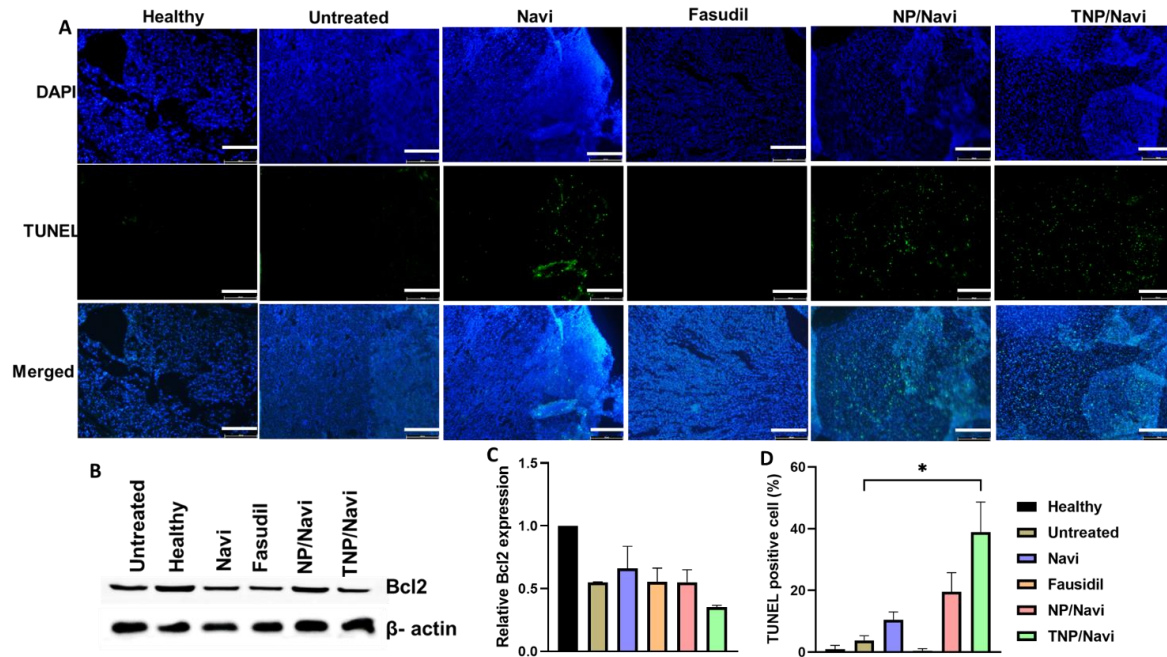


Figure 12: Immunohistochemistry of kidney tissue for Bcl2 expression. Bcl-2 inhibition and apoptosis of tissue after treatment. (A) Tunnel assay shows apoptosis (green dot) of fibrotic cell. (B) WB analysis of Bcl2. Bcl2 expression was decreased in the group treated with TNP/Navi. (C)+(D) Quantitative analysis of WB data and TUNEL assay. Scale bar represents 100 μ m.

2.4. CONCLUSIONS

Kidney fibrosis is a challenging and irreversible condition with limited effective and available treatment options. The use of the Bcl2 inhibitor (Navitoclax) has emerged as a potential approach to mitigate fibrosis. Despite its potential, however, Bcl2 inhibitors can cause severe haemato-toxicity, resulting in platelet destruction. Consequently, navitoclax is often administered orally to prevent direct exposure to blood cells, despite its low availability. To overcome this challenge, the present study employed AT2 peptide conjugated PLGA nanoparticles to deliver Navi specific to kidney and cells associated with fibrosis such as fibroblast and myofibroblast. The

AT2-targeted nanoparticles successfully ameliorated fibrosis, as confirmed by immunostaining of α -SMA and CTGF. This was accompanied by a reduction in the hydroxyproline levels and significant improvements in kidney function markers such as creatinine and BUN. In summary, nanoparticle enabled fibrosis-targeting Navitoclax (TNP/Navi) delivery showed less toxicity than oral administration of Navitoclax and significantly less side effects than Fasudil. This study represents a significant advancement in the development of kidney-targeting particles for the delivery of Navitoclax. These promising findings suggest that AT2 targeting hold emerging potential for improving outcome of kidney fibrosis treatment could represent a viable therapeutic option for treating kidney fibrosis, potentially paving the way for clinical trials in the future.

SUPPLEMENTARY INFORMATION

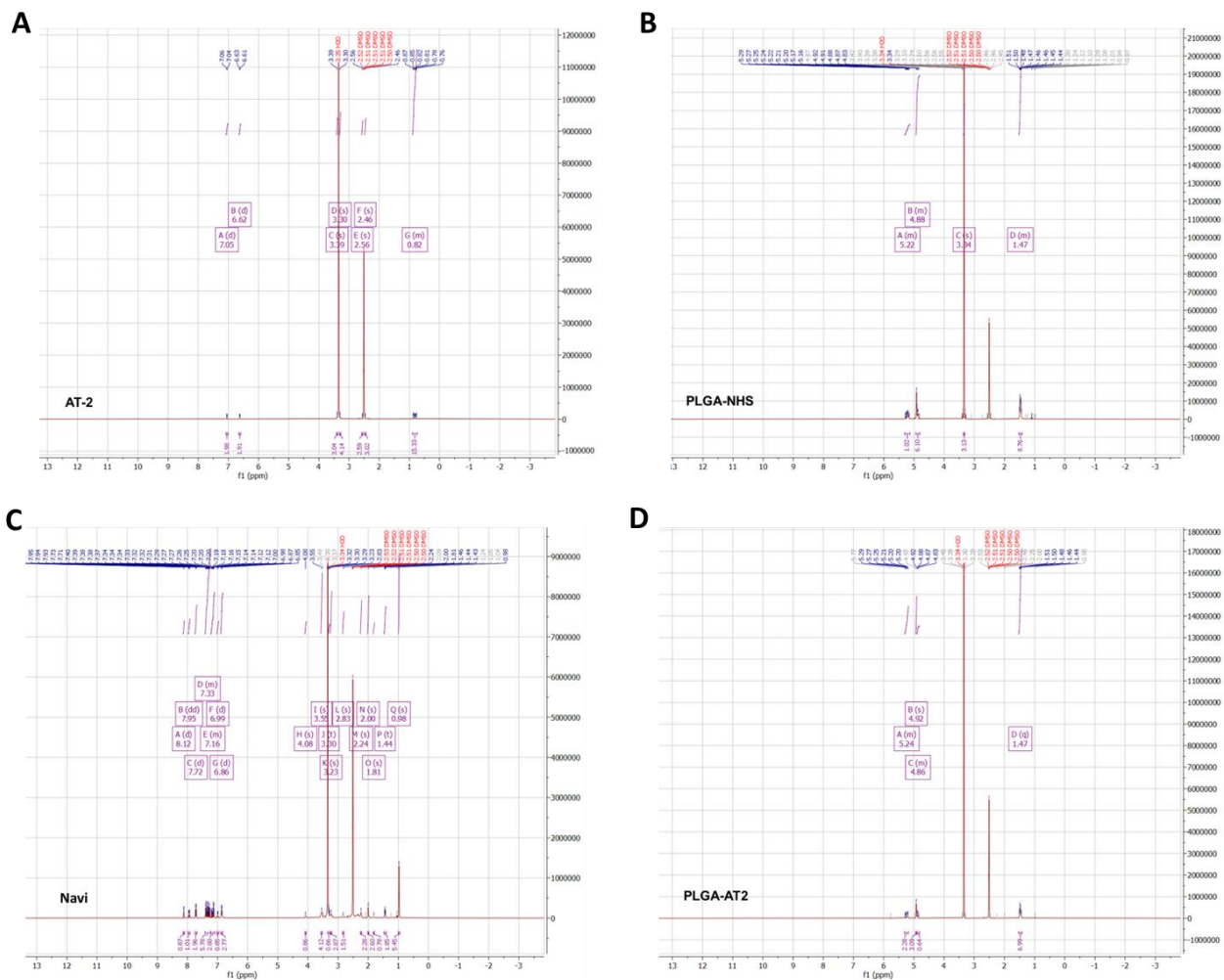


Figure S 1: Proton NMR. Proton NMR of AT2 (A), PLGA/NHS (B), Navi (C) and PLGA-AT2 (D).

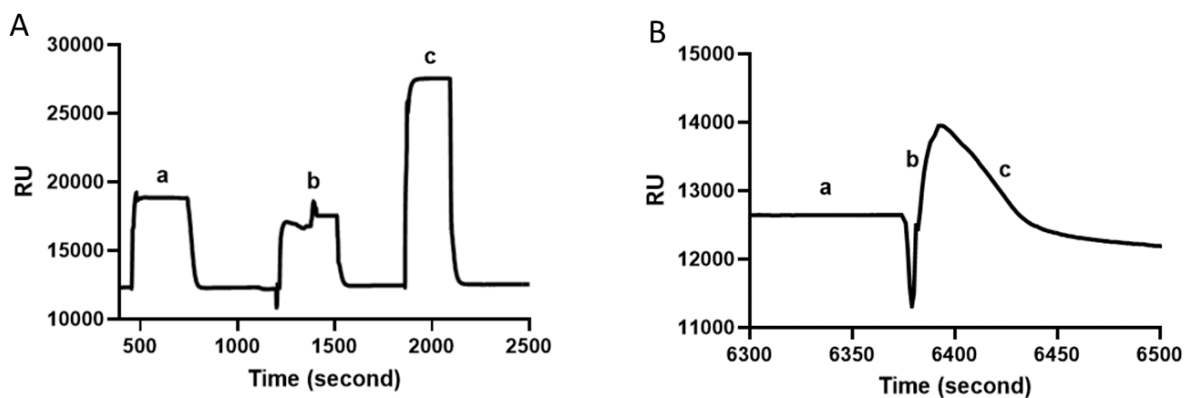


Figure S 2: SPR spectra. SPR spectra after immobilization of carboxylated gold chip with PLGA/AT2 nanoparticle (A). Response after running collagen over the nanoparticle (NP) liganded chip (B). (a) represents base line response with PBS, (b) is the response of binding of collagen with AT2 and (c) is the curve for dissociation.

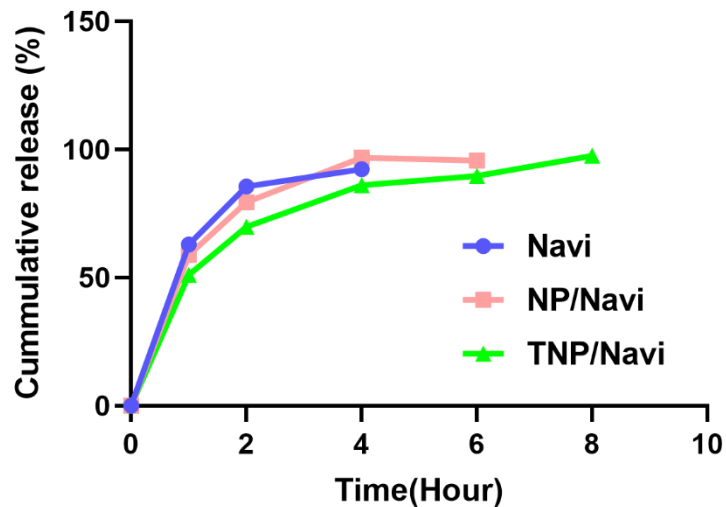


Figure S3: Release profile of Navi. Release profile of Navi shows slower release of TNP/Navi than free Navi.

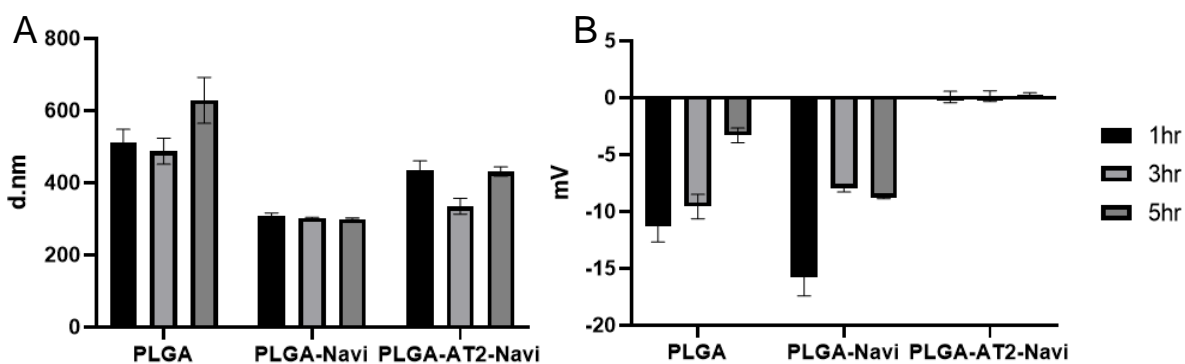


Figure S 3: Stability of NPs. The stability of NPs in PBS with 10% FBS were measured by size (A) and zeta (B) potential of the particles for up to 6hrs. It was observed that the particles were stable in the solution, especially (TNP/Navi) particle.

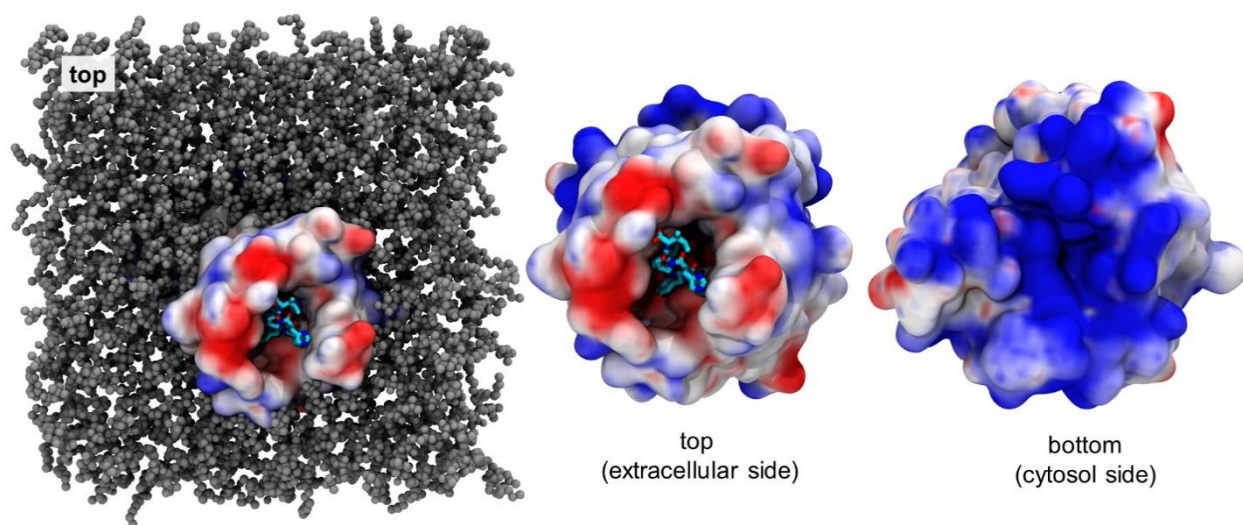


Figure S 4: Electrostatic potential surface of the AT2 protein binding to AT2 peptide. Analysis of the electrostatic potential surfaces of the AGTR1 protein binding to RYIHP1 peptide. Blue surfaces indicate regions of positive electrostatic potential and red surfaces indicate regions of negative electrostatic potential.

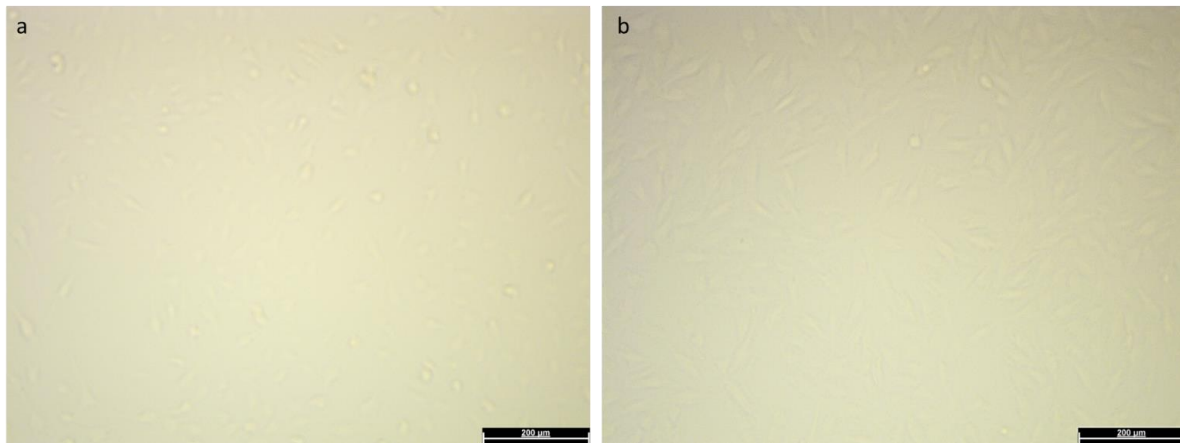


Figure S 5: Transformation of fibroblast to myofibroblast. NRK-49F cell before (a) and after (b) adding TGF β -1. After the incubation of TGF β -1 the cells became slender from round shape.

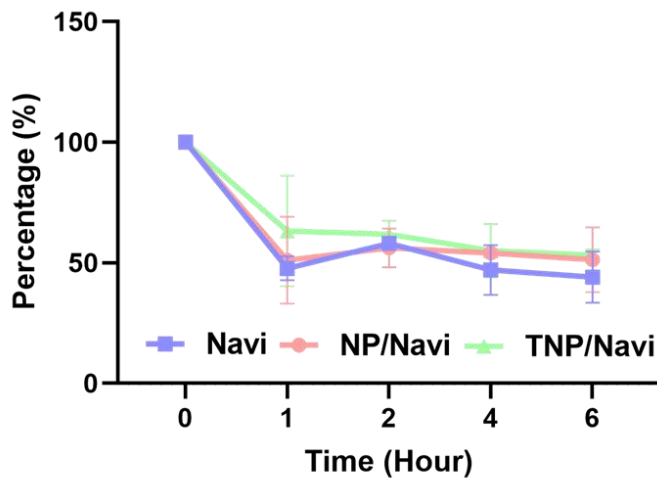


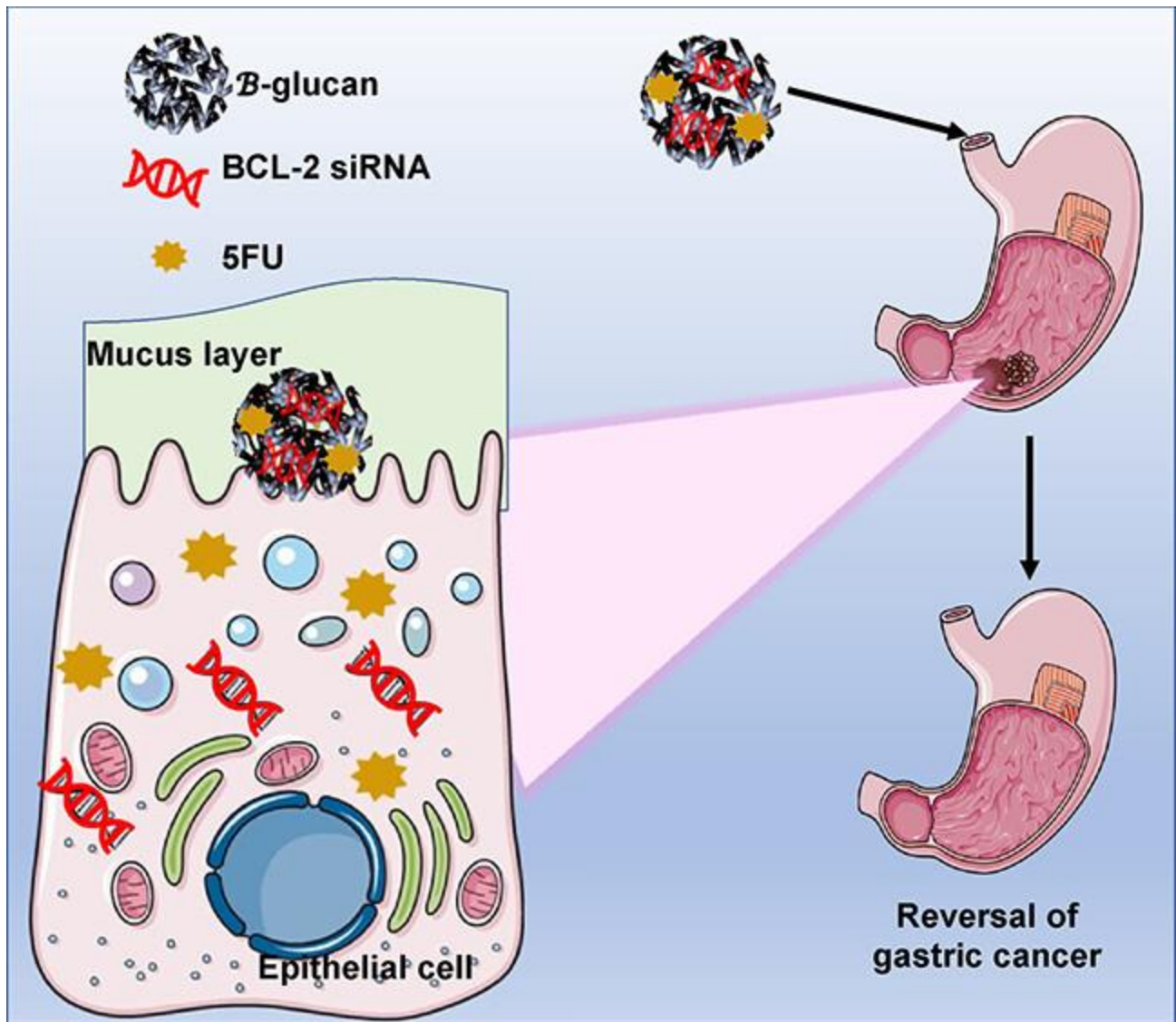
Figure S 6: Platelet count post-treatment with different Navi formulations. After administration of oral Navi, NP and TNP blood were collected at each different time point and platelet were measured. A sudden drop of platelet with oral Navi was observed in the 1st hr. With TNP the platelet did not drop as much as oral Navi as 1st hr also was constant up to the 6hrs. With oral Navi the platelet count was decreasing with each time point.

Chapter 3: β -Glucan-Mediated Oral Codelivery of 5FU and Bcl2 siRNA Attenuates Stomach Cancer

ABSTRACT

Based on cancer related deaths, stomach cancer is ranked 5th, and 1st among Hispanics. Lack of technologies for early diagnosis and unavailability of target specific therapeutics is largely the cause of the poor therapeutic outcomes from existing chemotherapeutics. Currently available therapeutic modalities are invasive and require systemic delivery, though the cancer is localized in the stomach at its early stage. Therefore, we hypothesize that an oral local delivery approach can extend retention duration of the therapeutics modalities within the stomach and thereby enhance therapeutic efficacy. To accomplish this, we have developed a β -glucan (BG) based oral delivery vehicle that can adhere to the mucus lining of the stomach for an extended period while controlling release of Bcl2 siRNA and 5-fluorouracil (5FU) payload for over 6 hr. We found that Bcl2 siRNA selectively knocked down the Bcl2 gene in C57BL/6 stomach cancer mice model followed by upregulation of apoptosis and remission of cancer. BG was found to be very effective in maintaining stability of siRNA for at least 6 hr, when submerged in simulated gastric juice tested *in vitro*. To investigate potential therapeutic effects *in vivo*, we used a stomach cancer mice model, where C57BL/6 mice were treated with 5FU, BG/5FU, siRNA, BG/siRNA, and BG/5FU/siRNA. Higher inhibition of Bcl2 and therapeutic efficacy was observed in mice treated with BG/5FU/siRNA confirmed with Western blotting and a tunnel assay. Significant reduction in tumor region was observed with histology (H&E) and immunohistochemistry (Ki67, TUNEL, and Bcl2) analysis. Overall, the oral formulation shows improved efficacy with non-significant side effects compared to the conventional treatment tested in gastric cancer mice model.

Keywords: stomach cancer; oral biologics; oral local delivery; stomach specific



GRAPHICAL ABSTRACT

3.1. INTRODUCTION

Stomach cancer is the 5th most common cancer by incidence and 3rd most deadly cancer [101]. In 2018, 782,685 out of 1,033,701 patients were died of stomach cancer worldwide [102]. According to the data from the American Cancer Society 26,380 new stomach cancer patients will be diagnosed solely in the United States in 2022, and among the diagnosed individual, 11,090 will die. Currently available therapeutic interventions for stomach cancer treatment are chemotherapy,

immunotherapy, radiotherapy, and surgery. Among FDA approved chemotherapeutic drugs, 5-fluorouracil (5FU), Capecitabine, Docetaxel, Epirubicin, Doxorubicin, Trastuzumab, Trifluridine, and Tipiracil are most widely considered in clinic for stomach cancer treatment [103]. Other promising drugs are those developed for immunotherapy, such as PDL1 inhibitors like Pembrolizumab or Nivolumab, and targeted gene therapy drugs have also shown promise for stomach cancer therapy [104]. Some genes (for instance IL-8, CLDN1, KRT17, CLDN7, and MMP7) are reportedly upregulated, and some other genes (for instance GAS5, ZIC1, RASAL1, *GPER*, *KIAA1324*, *ADA* and *SLC9A2*) are found to be downregulated in stomach cancer [105–108]. It has also been reported that upregulation of STAB1, STAT3, Bcl2, and Bcl-xL genes occur in the stomach during cancerous state [108,109].

Like the treatment of other cancers, for stomach cancer treatment, dosage form, rout of administration and dosage amount of the chemotherapeutics is crucial to avoid potential severe risk of toxicity to the healthy tissue associated with non-specific distribution. Stomach cancer management is severely challenging due to the difficulty to deliver the appropriate amount of drug to the location of cancer and maintain their therapeutic concentration for prolong duration, regardless of rout of administration. This is further compounded by the relatively late diagnosis that is more typical of stomach cancer patients and that occurs when the cancer has grown and spread across the stomach [110]. In addition, oral administration of chemotherapeutics is not very effective due the bowel movement and shorter retention duration. The retention duration of any orally administered drug to the stomach is 10-30 min, much less than the duration often needed to induce adequate therapeutic effect and maintain appropriate therapeutic concertation within the cancer site [111,112] . Finally, oral delivery of therapeutic modalities is challenging because of significantly low bioavailability resulting from poor intestinal permeability, enzymatic

degradation, thick mucus membrane barrier, and off-target localization [113]. In order to overcome these issues, we aim to develop an oral local delivery vehicle, made from the mucoadhesive carrier, b-glucan (BG) [114]. BG is a unique carbohydrate polymer that is naturally present in the cell wall of yeast, fungi, and cereal. BG used in this study is a barley derived low viscosity glucose polymer with a molecular weight of 179,000 Da. We have previously reported that BG is very stable in acidic buffer, has a strong binding affinity with mucin, and forms microstructure particles in presence of fatty acid [114]. Studies show that the BG-based vehicle is highly effective in oral vaccine and protein delivery [115,116]. The BG-mediated mucoadhesive particle has the ability to protect the therapeutic regimens from the harsh gastric environment, enhance retention of the therapeutic payload within the stomach for a longer duration, and maintain sufficient therapeutic concentration for prolong period (6 hr or more) [117]. In addition, BG was found to act as an immune modulator of the gastrointestinal (GI) tract [118]. Finally, BG also has shown significant potential in GI site-specific drug delivery to treat liver diseases, bowel disease, and stomach cancer [117,119,120]

5FU is a pyrimidine analog, a potent and widely used chemotherapy to treat GI-tract related cancers including stomach cancer [121,122]. A meta-analysis of stomach cancer treatment revealed a significant advantage in terms of 3-year survival when on chemotherapy with S-1, an oral 5FU derivative (80 %), compared to the surgery (70%). 5FU or S-1 is considered as first-line treatment due to better efficacy but is recommended to administer with adequate precaution to avoid the severe risk of side effects associated with toxicity [123]. Despite having higher therapeutic effectivity, oral delivery causes various side effects within the GI tract and intravenous administration produces toxicities in major organs including the heart, lungs and kidney [124]. Side effects of 5FU include cardiotoxicity, hypotension, breathing problem, hair loss, and weight loss

[124]. With the development of a delivery platform that has the potential to minimize systemic distribution of 5FU and increase drug concentration within the site of cancer, it is highly likely possible to minimize drug-mediated toxicity and increase therapeutic effects. Besides, 5FU itself is not very effective of treating cancer, for instance, treatment response rate is between 10-15% for advanced colorectal cancer. Therefore, we presume that a combination of RNAi can improve the therapeutic effect by synergizing the mechanism of action. Therefore, we aim to incorporate a Bcl2 small interfering RNA (siRNA) that holds emerging promise for the genetic treatment of cancer. Since its discovery, siRNA is considered to apply for various cancer treatments as gene therapy including stomach cancer [125,126].

Bcl2 overexpression has been found in cancers including the stomach, breast and pancreas, where it promotes the proliferation of cancer cell [127–130]. Bcl2 downregulation has also been to induce apoptosis to tumor cell and make them more sensitive to chemotherapy. [131] Some recent reports have demonstrated strategies for improved oral delivery of siRNA to ameliorate hepatic cancer through nanoparticle and mucoadhesive molecules [132]. The Bcl2 family is composed of a subset of proteins that act as apoptosis regulators (Figure 13). Research suggested that the hyperactivation of Bcl2-related anti-apoptotic effects correlates with cancer occurrence, progression, and prognosis. Therefore, we hypothesize that a combination of Bcl2 siRNA and 5FU can accelerate stomach cancer therapeutic outcomes when given orally.

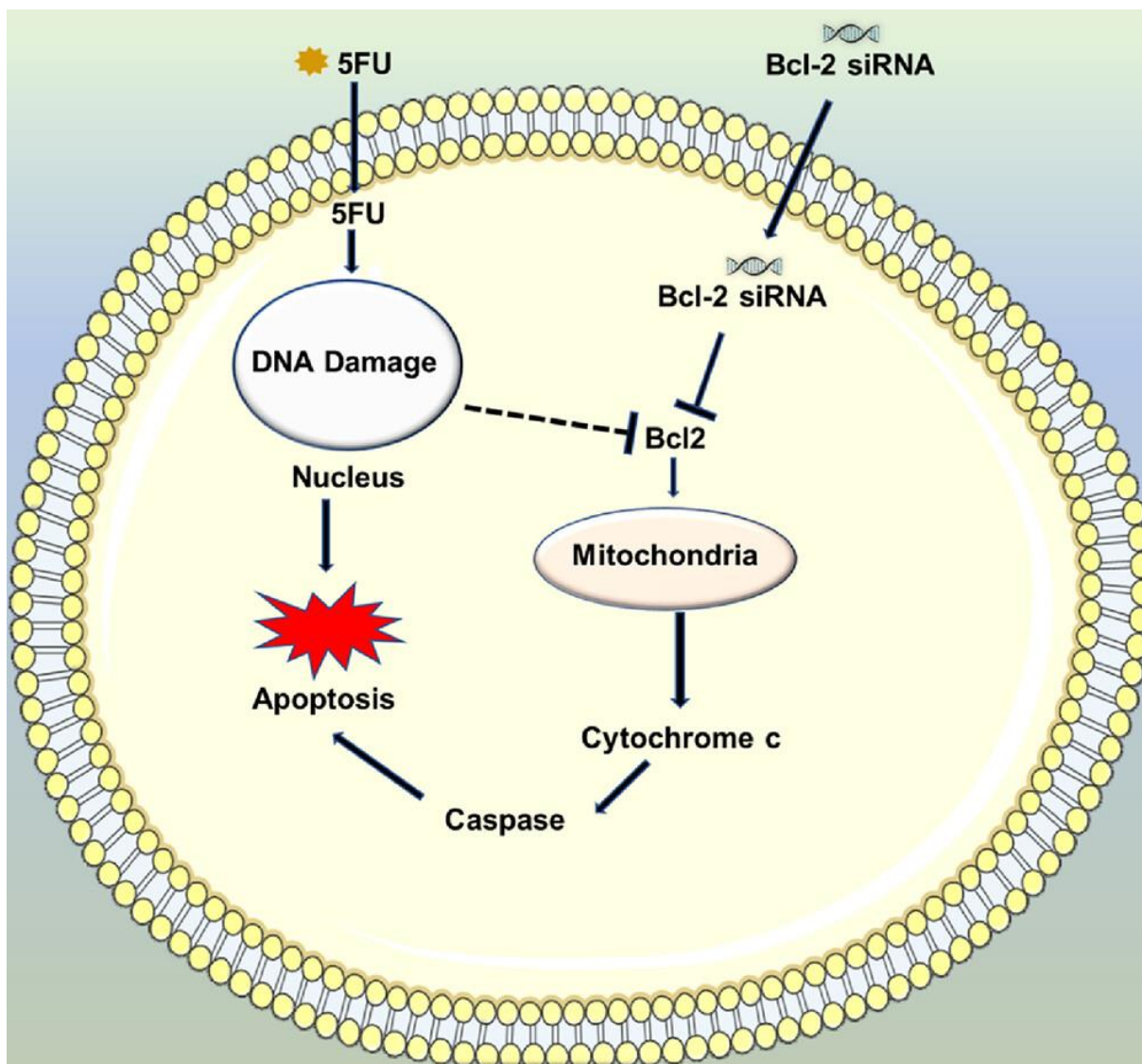


Figure 13: The Mechanism of Action of Co-Treatment of 5-FU and Bcl2 siRNA and Their Synergy to Improve Stomach Cancer Treatment.

To prove the concept and to investigate therapeutic feasibility, 5FU and siRNA were loaded within a nanoparticle composed with BG. Both physical and chemical characterization were conducted prior to utilizing the formulation for *in vitro* and *in vivo* studies. We have observed that the BG-based oral vehicles not only increase retention of the payload of 5FU and siRNA within the stomach but also facilitate sustained release of the payload for over 6 hr. *In vivo* studies

revealed that the oral delivery of BG/siRNA/5FU downregulates the Bcl2 protein by 60% and increases apoptosis by 140% with a daily oral dose for 15 days. Immunohistochemistry analysis of stomach tissue also shows that Ki67 expression reduces by 300% compared to untreated cancer and 5FU groups, and 200% compared to siRNA treated group. These results are obvious indication of the potency and effectiveness of the BG-based oral formulation of siRNA/5FU. The toxicological studies including histochemistry and serum biochemistry also demonstrate the biosafety of the orally administered siRNA/5FU formulation and hold a strong promise for pre-clinical studies with larger animals.

3.2. MATERIALS AND METHODOLOGY

3.2.1 Materials

The human colon cancer cell line (CaCo2) and stomach cancer cell line (AGS) were purchased from ATCC (Manassas, VA). 5FU, sodium dodecyl sulfate, and Coumarin 6, were purchased from Sigma-Aldrich (St. Luis, MO). β -Glucan (MW 179,000) was purchased from Megazyme (Wicklow, Ireland). Bcl2 siRNA was purchased from cell signaling technology (Danvers, MA). Fetal bovine serum (FBS), penicillin, Phosphate-buffered saline (PBS), and 0.05% Trypsin-EDTA were purchased from Life Technologies (Carlsbad, CA). Bcl-2 SiRNA I (Cat #6441) was purchased from Cell Signaling Technologies (Danvers, MA). Bcl2 antibody, ki67 antibody, and FITC- Goat anti-Rabbit IgG was purchased from ABclonal (Woburn, MA). Simulated gastric juice was purchased from RICCA (Arlington, TX). Click-iT Plus Tunnel assay, eosin, xylene, Harris Hematoxylin, was purchased from Fisher Scientific (Waltham, MA).

3.2.2. Preparation of BG and formulations

BG NP were prepared by direct physical mixing method. In details, 30 mg of BG was dissolved in 1 mL of DI water upon heating at 80 °C and constant stirring for 15-20 min. Upon heating and continuous stirring BG form transparent gel like solution. Thereafter, with discontinue of heating 12 mg of 5FU was directly added to the BG solution and kept stirring for additional 30 min for uniform mixing.

To prepare BG/5FU/siRNA, 12 µL of siRNA was added in BG/5FU under constant stirring. Then it was mixed with alternate sonication and vertexing. siRNA loaded BG nanoparticle was prepared via electrostatic interaction. 30 mg of BG was dissolved in 1 mL of DI water upon heating at 80 °C and constant stirring for 15-20 min. 12 µL (12 nM) of siRNA was added into the BG solution after it comes to the room temperature. The siRNA solution was added to the BG solution dropwise under vigorous stirring for 10 min. The formation of the BG/siRNA nanoparticle form via electrostatic interaction between BG and siRNA.

3.2.3 Characterization of the formulations

The particle size and zeta potential of BG formulations were determined by a Zeta sizer (Nano ZS, Malvern Instruments, Worcestershire, UK) and kept at 25 °C during the measuring process. All formulations were analyzed three times and the results are presented as the mean. The stability of the formulations and their individual payload were evaluated in saline (pH 7.4) and simulated gastric juice (pH 1-1.4) at different time points. For measuring the size and zeta potential of BG, BG/5FU, BG/siRNA, and BG/5FU/siRNA, all the formulations were diluted in deionized water.

3.2.4 In vitro release study

In vitro release using a dialysis bag against simulated gastric juice. Briefly free 5FU, BG/5FU and BG/5FU/siRNA were taken into the dialysis bag individually. 2 mg of 5FU were dissolved in 100 μ L of DMSO and were dialyzed against 50 mL of simulated gastric juice (pH 1-1.4, 37 °C) with 2 kDa MWCO dialysis bags, and continuous stirring at 100 RPM. 1 mL of solution was collected from outer phase in every 2 hr for a 12 hr period and the same volume of GJ was added to maintain the volume. The release amount of 5FU into the GJ was quantified by measuring the absorbance at the wavelength of 265 nm by UV-Visible spectrophotometer (UV-2800, Shimadzu spectrophotometer) [133].

3.2.5 Stability of the formulation

To examine the stability of the formulations, naked siRNA and siRNA with BG were diluted in PBS and incubated with BG at 37 °C for 0, 1, 2, 4, and 6 hr, and size and zeta potential were measured. To measure the stability of siRNA in gastric juice with and without BG, siRNA and BG/siRNA were diluted with simulated gastric juice and incubated for 0, 1, 2, 4, and 6 hr and then size and zeta potential were measured according to the method demonstrated earlier. Gel electrophoresis of these formulations was also conducted to confirm the stability of loaded siRNA. To determine the stability of siRNA within BG, the siRNA samples were separated into 1% Agarose gels. Agarose solution was prepared by dissolving in 1X TAE and heated in a microwave for 3 min until dissolved completely. Ethidium bromide was added to the solution before pouring the agarose solution into the casting stand and a 10-well comb was placed to generate wells that are 1.5 mm deep. The melted agarose was allowed to cool for 30 min at room temperature for polymerization. The chamber was filled with 1X TAE buffer solution to a height of 1.5 cm above

the gel surface. RNA samples were premixed with the agarose gel loading dye (6X) prior to loading 20 mL (1 μ L siRNA, 3 μ L dye with 6 μ L of simulated gastric juice, and 10 μ L BG) of samples into the wells from left to the right. The power supply was activated as soon as all wells were filled, to avoid initial diffusion of the dye into the gel. The samples were run at 100V for 40 min and were imaged using ChmiDoc image analysis (BioRad, USA). The formulations were incubated in GJ for 0, 1, 2, 4, and 6 hr prior to measure stability of the payload of siRNA. The stability of naked siRNA and BG/siRNA in GJ were also measured by the nanodrop as well.

3.2.6 Ex-vivo diffusion study

To measure the diffusion of hydrophobic small molecule through the intestinal layer an ex-vivo study with porcine intestine was done. Here cumarin-6 was used a model hydrophobic molecule instead of 5FU for visualization purposes. Cumarin-6 and BG/cumarine-6 was added over the porcine intestine for different time point. In each time point the intestine was washed with PBS for 5 min then was subjected to image. BG/cumarin-6 particle was prepared by O/W emulsion.

3.2.7 Surface Plasmon Resonance (SPR) to demonstrate binding interaction between formulations and mucin

To demonstrate physical and chemical interaction between the BG-based formulations and mucin, we used the SPR (ibClu, South Korea) technique. BG solution was run over carboxylate functionalized (-COOH) Au-chip, 1x PBS was used as a running buffer, and 50 μ M mucin was used as an analyte. The experiment was conducted according to the manufacturer's instruction. Briefly, EDC and NHS were added over the COOH-Au chip for 3 min with real-time monitoring.

Then, BG was run over the chip for 5 min at a flow rate of 30 $\mu\text{L}/\text{min}$ followed by running of ethanolamine blocking buffer. From the change of response from baseline, the immobilization of BG was confirmed. After immobilizing the chip with BG, mucin was injected at flow rate of 30 $\mu\text{L}/\text{min}$ for 5 min and after that regeneration buffer was injected to wash out the excess analyte from the chip. The data was collected from the software and graph were plotted in Prism GraphPad.

3.2.8 Cell culture

For the cell experiment AGS cell line were used. The cells were cultured at 37 °C in a humidified atmosphere containing 5% CO_2 in DMEM media supplemented with 10% FBS. 5000 cells per well were seeded in a 96-well plate and incubated overnight. BG formulations with different concentration of 5FU (45 μM , 35 μM , 25 μM , 15 μM , and 5 μM), and 1 nM of siRNA were added into the cells and incubated for 24 hr. To measure cytotoxicity, an MTT assay kit (Vybrant MTT cell proliferation assay kit, ThermoFisher) was used according to the manufacturer's instructions. In brief, 10 μL of the MTT solution was mixed with 100 μL of the culture medium for 4 hr in the incubator. Then 100 μL of SDS-HCl solution was added to each well and mixed well. Then incubated for another 12 hr in a humidified chamber. Finally, the absorbance at 570 nm was taken. Healthy cells without any formulation were used as a control; background absorbance was subtracted from each value, and the cell viability percentage was measured [66]. The data is provided in the supplementary figure S7.

3.2.9 Development of stomach cancer mice model

All animal experiments were carried out in strict accordance with protocols approved by the Animal Care and Use Committee of the University of Texas at El Paso comply with the

National Research Council's Guide for the Care and Use of Laboratory Animals. Both male and female (50:50) mice were chosen for the experiments as sex has no significant influence in the stomach cancer. A stomach cancer mice model was developed by feeding N-methyl-N-nitrosourea (NMNU) with water (IACUC protocol no A-201019-A). The 6-week-old C57BL/6 mice were kept in a 12 hr light-12 hr dark cycle. The mice had unprotected access to food and water. NMNU was dissolved in distilled water available *ad libitum*, freshly prepared three times per week. The mice received 240 ppm NMNU in the drinking water over 5 weeks (every other week). Five weeks after NMNU administration, the mice were ready for the experiment, as the method was reported elsewhere [134,135]. A total of 30 stomach cancer mice were prepared and divided randomly into 5 groups- no treatment (control), 5FU, BG/5FU, siRNA, BG/siRNA, and BG/5FU/siRNA. Another group of healthy mice were used as a negative control without any treatment. To investigate therapeutic feasibility, 5FU (10 mg/kg) and siRNA (100 nM) was administered either orally (PO) or intravenously (IV). All the formulations were freshly prepared prior to administration. Formulations were administered orally on every 3rd day for the subsequent 5 cycles over 15 days. The animals were sacrificed 72 hr after the last treatment followed by the organ harvest and blood collection for further studies. Immediately after harvesting the size and weight of the stomach and intestine were measured.

3.2.10 In vivo and ex vivo imaging for biodistribution

To understand the absorption and biodistribution profile of the orally administered formulation, coumarin-6, a fluorescent dye was loaded with BG and orally administered via gavage to mice. For in vivo imaging the mice were anesthetized and then imaged using an in vivo imaging system (IVIS) at different time points of post-administration, according to the method published

earlier[136]. For the ex vivo imaging, the mice were sacrificed after 2, 4 and 6 hr of post-administration, and the organs were harvested, followed by imaging using the IVIS.

3.2.11 *In vivo* protein expression

The fresh frozen stomach tissue was homogenized using RIPA buffer with freshly prepared protease inhibitor in it. The homogenate was then centrifuged at 13,000 rpm for 10 min at 4 °C. The supernatant was collected, and the total protein content was determined using Bradford's assay (Sigma-Aldrich). SDS-PAGE (12%) was performed to separate protein samples (30 µg) at 70–80 V for 3 hr at room temperature. Later, the proteins were transferred to a PVDF membrane using a transfer unit run at 25 V overnight at 4 °C. The PVDF membrane was blocked by incubating with 3% BSA containing TBST for 90 min. The membrane was incubated with Bcl2 and β-actin primary antibodies (Abclonal, USA) overnight at 4 °C. After three washing cycles with ice-cold PBS, the membrane was incubated with horseradish peroxidase-conjugated secondary antibody (Abclonal., USA) for 2 hr at room temperature. The primary and secondary antibodies were used at a 1:1000 dilution ratio. The membrane was treated with ECL mixture. The bands were visualized using a ChemiDoc imaging system (BioRad, USA). The band intensities were calculated using ImageJ software.

3.2.12 Histology

Three days after the last treatment the animals were sacrificed to harvest the organs for further histology and immunohistochemistry. Different part of intestine (duodenum, jejunum, and ileum) was embedded in OTC and other organs were embedded in paraffin. Fresh frozen stomach was processed in STP 120 Spin Tissue Processor (Fisher Scientific, USA) and embedded in

paraffin on the following day. The tissue was cut at 6 μm thickness and was attached on a super frost plus slide (Fisher Scientific, USA). The slides with tissue sections were used for H&E staining, immunofluorescence assay, and tunnel assay. H&E image was taken using a MoticEasyScan One slide scanner (Motic digital pathology, USA) and Leica DM 6000B fluorescent microscope.

3.2.13 Immunofluorescence and immunohistochemistry analysis

Immunofluorescence analysis was performed to understand the Bcl2 and ki67 protein expression in tumor tissues after treatment with different formulations. The 6 μm thin sections were obtained by sectioning paraffin-embedded colon tissues using a microtome. Sections were mounted onto poly-l-lysine-coated super plus charged glass slides and rehydrated in multiple concentrations of alcohol and xylene for 5 min each. Sections were incubated with antigen retrieval sodium citrate buffer (10 mM sodium citrate buffer pH 6, 0.05% Tween 20) at 90–95 °C for 10 min and blocked using 2.5% bovine serum albumin (BSA) in Tris-buffered saline for 1 hr at room temperature. Then, the sections were incubated with Bcl2 and ki67 primary antibody (at 1:100 and 1:50 dilution ratio) overnight at 4 °C. The next day, the sections were incubated with FITC-Goat Anti-Rabbit IgG secondary antibody for 2 hr at room temperature. The slides were then dehydrated and mounted with DAPI mounting media. Images were acquired using Leica microscope.

3.2.13 TUNEL assay

Click-iT™ Plus TUNEL Assay (Thermo Fisher) and an Alexa Fluor™ 488 dye assay kit was used in this assay to examine the fragmentation of DNA and detection of apoptosis according to the manufacturer's instructions. Shortly, a fresh frozen stomach sample was fixed in formalin. And

then was dehydrated in increasing concentration of alcohol. After cleaning in xylene those tissues were submerged in paraffin. The paraffin-embedded tissues were cut to 6µm thickness for the assay. Before conducting the assay, the section was deparaffinized with xylene by decreasing the concentration of ethanol from 100% to 70%. After deparaffinization, the stomach sections of all treatment groups were washed twice in PBS for 5 min and then incubated for 15 min with 1X Proteinase K solution (Component H in the assay kit was diluted 1:25 in PBS). The slides were again fixed in 4% PFA for 20 min and washed with PBS for 5 min. To induce DNA-stand breakdown in the skin, skin samples were incubated with 1 unit of DNase I (diluted in 1X DNase I Reaction Buffer (20 mM Tris-HCl, pH 8.4, 2 mM MgCl₂, 50 mM KCl) for 30 min at room temperature. After incubation, the sections were washed with DI water and 100 µL of TDT Reaction Buffer (Component A in the kit) were added to each well and incubated for 10 min. The TDT reaction buffer was removed and replaced with 50 µL of the prepared TDT reaction mixture for 1 hr. Next, the reaction mixture was removed, and each well was rinsed with DI water and the samples were incubated in 3% BSA and 0.1% Triton™ X-100 in PBS for 5 min with gentle shaking. After rinsing the slide with 1X PBS 50 µL of freshly prepared Click-iT™ Plus TUNEL Reaction cocktail added to each section for 30 min in the dark. The reaction cocktail was removed and replaced with 3% BSA in PBS for 5 min. The samples were rinsed with 1X PBS and mounted with DAPI mounting media and a coverslip. prepared for imaging by placing the tissue on a glass slide and adding a mounting medium and a coverslip. The slides were incubated for 1 hr at 4 °C and then images were taken using Leica LAS X software attached to a Leica DM2000 microscope (Leica, Germany).

3.2.14 Serum biochemistry

Serum biochemistries analysis was conducted to determine the systemic toxicity of the formulations administered to the stomach cancer mice model. Three days after the last dose of treatment, the mice were euthanized, and 1 mL of blood was collected from the portal vein in heparin-coated tubes. Blood was centrifuged at 3000 rpm for 7 min and plasma was collected. Serum biochemistry analysis included parameters related to liver and kidney function, e.g., aspartate aminotransferase (AST), alanine aminotransferase (ALT/GPT), alkaline phosphatase (ALP), total protein (TP), blood urea nitrogen (BUN), and creatinine (Cr). Biochemical analyses were quantified using a chemical analyzer (Element-DC by HESKA), and the results were presented using GraphPad Prism software.

3.2.15 Statistics and image analysis

All experiments were carried out in triplicates, and the error bar is indicated as mean \pm SD unless stated otherwise. Student t-test, Welch's nonparametric t-test, and one-way analysis of variance (ANOVA) was performed using GraphPad Prism nonlinear regression software (GraphPad Software Inc.). A P value of <0.05 was considered significant. *Indicates statistical significance with $p < 0.05$; *** indicates statistical significance with $p < 0.001$. Image analysis of immunofluorescence and tunnel assay was done by using the OpenCV Python programming library.

3.3 RESULTS AND DISCUSSION

3.3.1 Preparation and characterization of BG particles

The barley-derived low-viscosity BG used in this study is a long-chain polysaccharide, with very low solubility in the aqueous solution (**Figure 14 A**). With gentle stirring in association with rising

temperature (up to 80 °C) the BG get dissolved completely in DI water. BG itself used as both solubilizer and carrier of the payload for both 5FU and siRNA. The method of the formulation preparation is shown in **figure 14 B**. Upon heating at 80 °C the mixture of BG forms a gel like clear solution in presence of water which facilitate mixing of the hydrophobic 5FU physically. We have used SEM, to confirm shape and size of the - BG/5FU, BG/siRNA and BG/5FU/siRNA formulations (**Figure 14 C**). The SEM images of BG/5FU and BG/siRNA are provided as the supplementary information (**Figure S8**).

The size of BG, BG/5FU, BG/siRNA, and BG/5FU/siRNA was measured as 273.66 ± 39.87 , 569 ± 52.43 , 470 ± 80.24 , 439.66 ± 42.33 , respectively, using dynamic light scattering (DLS). The result indicates that size of the 5FU and siRNA loaded particles were bigger compared to naked BG particles. Zeta potential of BG, BG/5FU/, BG/siRNA and BG/5FU/siRNA were recorded as 0.01 ± 0.06 , 1.76 ± 0.09 , -3.36 ± 0.63 , -0.91 ± 0.19 , respectively. The zeta potential of BG/siRNA/siRNA were increased compared to BG/siRNA, as BG/5FU showed a positive charge (1.76 ± 0.09 mV). The change of zeta potential confirms the successful loading of 5FU and siRNA within BG nanoparticle. We do not see excessive changes, as the siRNA is meant to be loaded within the core and that is not expected to impact on charges on surface.

The size and zeta potential of BG in PBS and simulated gastric juice were measured up to 5 hr of incubation at room temperature. We have observed that the average particle size and zeta potential changed with each loading of the compound. The average size of BG in PBS was 273 ± 39 nm in diameter at the first hour and 386 ± 54 , and 583 ± 81 nm in diameter at 3rd and 5th hr of incubation (**Supporting figure S7**). Which is an indication that the formulations tend to form aggregation and that results in increment of the diameter. Similarly in the presence of simulated gastric juice, the average size of BG was found to be 276 ± 15 , 399 ± 18 , and 608 ± 62 nm in diameter at 1st, 3rd, and

5th hr, respectively. It has been observed that with time the size tends to increase, as well. After 5 hr of incubation the size increased by almost 200% in both saline and simulated gastric juice. As the size is almost similar in both PBS and simulated gastric juice, we can conclude that gastric juice does not impact the formulation differently than saline. BG is hydrophilic in nature and due to the presence of abundant hydroxyl groups that participate in hydrogen bonding with water and give the molecule the ability to hold water [137].

The release study of 5FU was conducted in a simulated GJ. BG incorporated 5FU shows sustained release trend compared to the free 5FU. The cumulative release of free 5FU reaches to the 100% in 5 hr of dialysis, whereas, for BG/5FU formulations 100% release of 5FU takes almost 10 hr, is an indication of sustained release (**Supplementary Figure S9**).

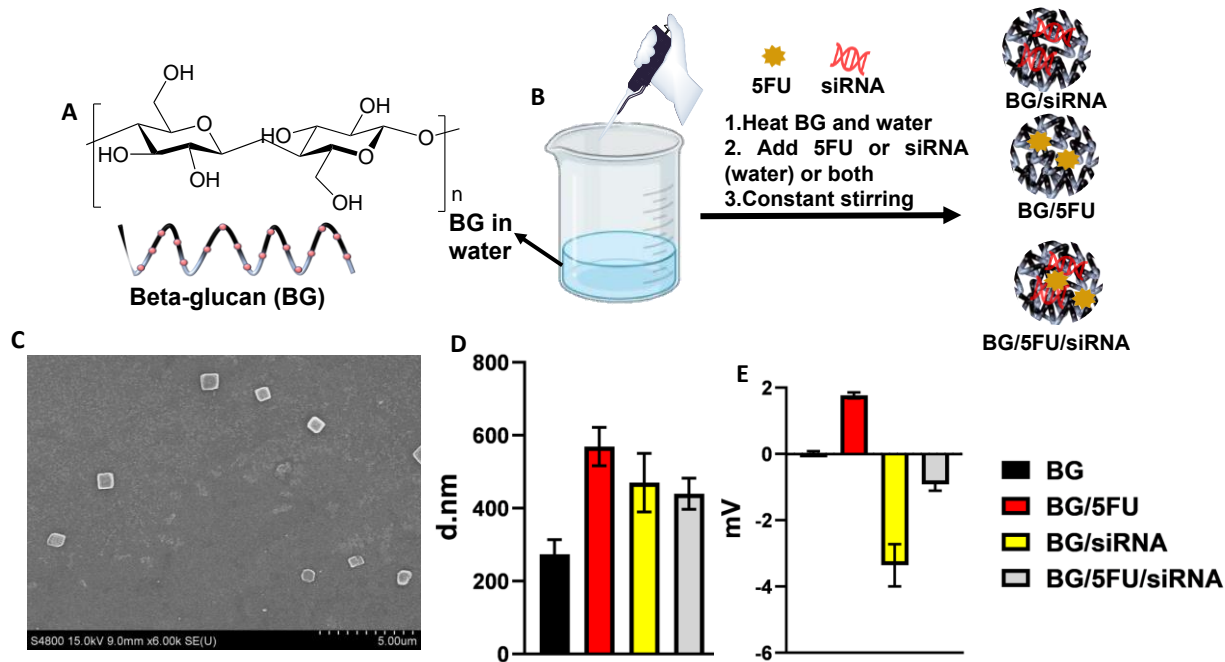


Figure 14: Chemical and physical properties of the formulations. (A) Chemical structure (repeating unit) and schematic presentation of BG. (B) Schematic representation of preparation of formulations; BG/siRNA, BG/5FU and BG/5FU/siRNA. (C) SEM images of BG/5FU/siRNA BG showed smooth surface and nano size (Scale bar= 5 μm). (D) Size distribution, and (E) zeta

potential of all the formulations were measured using DLS and zeta analyzer, respectively. Data presented as mean \pm SEM, where n=3.

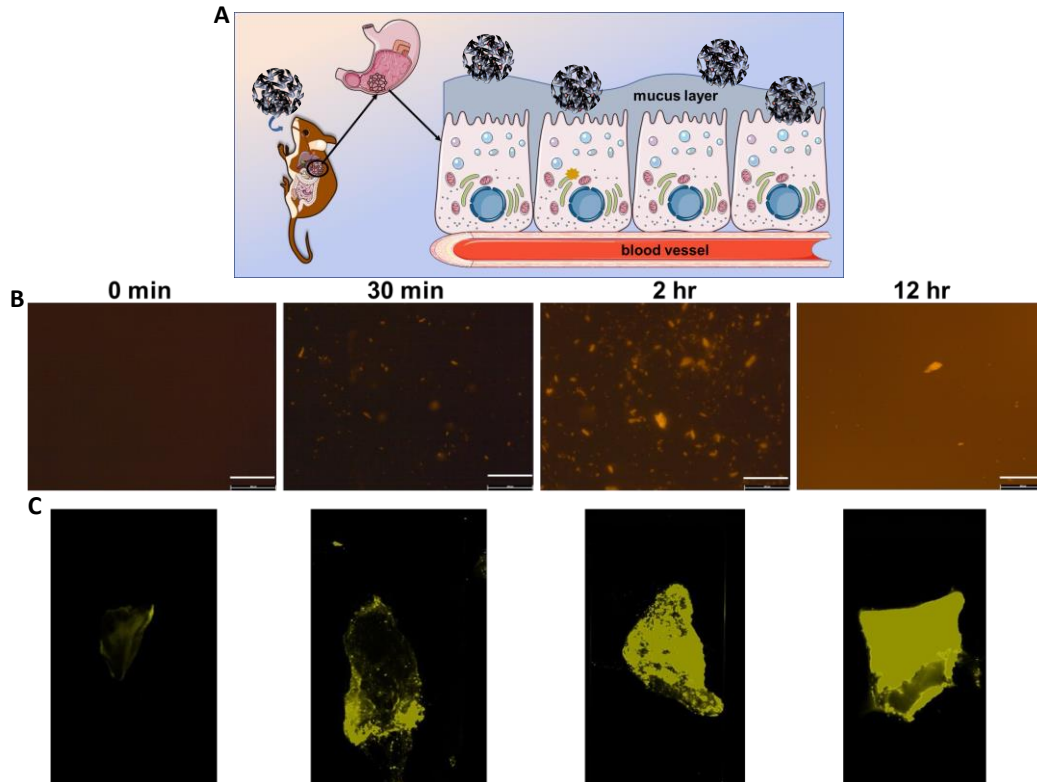


Figure 15: Mucoadhesive properties of BG. (A) A schematic representation of mucoadhesiveness of BG and how it facilitates the transport of siRNA and 5FU across the epithelium. BG/coumarin-6 was incubated on the porcine intestine for a different period and washed for 5 min before taking the image. (B) Image shows that BG facilitates to penetrate of the hydrophobic coumarin-6 into the intestinal layer with time. Whereas only coumarin-6 without BG does not diffuse through the intestine. (C) The same section of BG/coumarin-6 was taken under a ChemiDoc imager (BioRad, USA) and the result corresponded with the image of BG/coumarin-6 in (B). The components in figure (A) were obtained from smart.servier.com.

3.3.2 Mucoadhesive properties of BG

Figure 15A demonstrates how BG particles interact with mucus layer within stomach. The mucoadhesiveness and intestinal transportation of hydrophobic small molecule were further confirmed by an *ex vivo* diffusion study in a porcine intestine lumen. As the mucous layer is a barrier for hydrophobic molecules, to check how it cross through the epithelial layer with assistance of BG we have used coumarin-6, a small molecule hydrophobic fluorescent dye with similar chemical and physical properties (molecular weight and hydrophobicity) as 5FU, for ease of visualization and detection purpose [138]. Higher fluorescence intensity and accumulation of coumarin-6 was observed in the stomach layer with increment of duration of incubation. At the 2nd hr, presence of coumarin-6 was observed within deeper layers of the intestine, which indicates the transportation of hydrophobic small molecule (**Figure 15B**). At the 12th hr, coumarin-6 incorporates evenly across the layers of the intestine. The same tissue was subjected to be observed under a ChemiDoc imager to capture the fluorescence signal within the cross-sectioned of the intestinal lumen and similar result was observed. With time (0.5, 2, and 12 hr) more coumarin-6 were distributed throughout the intestine which is an indication and confirmation of BG's ability to facilitate intestinal transportation of hydrophobic payload (**Figure 15C**). However, the image with only coumarin-6 shows that without BG, coumarin-6 itself is not able to diffuse through the intestinal layer.

Mucoadhesive polymers have been found to be crucial in delivering nucleic acid and peptide drugs. Recently a study stated that mucoadhesive nanoparticle has the potential to deliver KDM6A-mRNA on the targeted site and treat bladder cancer [139]. SPR analysis was performed to examine how BG interacts with mucin. The results demonstrate that BG has mucoadhesive properties and

binds with the mucus in presence of acidic simulated gastric juice. A carboxylated gold (Au) chip was modified with BG and a solution of mucin was run over the chip to understand their binding kinetics, association, and dissociation profile. SPR analysis shows a response of 30000 RU from baseline, which confirms the strong binding affinity of BG with mucin. Curve (a) indicates the association of BG with mucin, curve (b) represents the plateau as it continues binding, and curve (c) represents the dissociation of BG with mucin. As mucin is the main component of the mucus layer, the association, and binding profile of BG with mucin provides evidence of BG's affinity with mucus layer and its ability to bind with (**Figure S11, and S12**).

3.3.3 Stability of siRNA payload in BG formulation

The stability of siRNA was measured with and without BG in PBS and simulated gastric juice. The size and zeta potential measurement of BG and BG/siRNA in presence of PBS and simulated gastric juice were conducted from 0 to 6 hr to examine the stability of siRNA payload. siRNA is a nucleic acid with a negatively charged surface and forms particles via electrostatic interaction with the partially cationic-charged BG (0.0158 mV). Size of the BG/siRNA formulation was measured as 370 ± 80 nm at 0 hr and 707 ± 76 nm in diameter at 6th hr. The increasing size indicates the possibility of self-aggregation of siRNA in simulated gastric juice when attached to BG (**Figure 16B, and 16C**). The result was confirmed by zeta potential analysis. As negatively charged siRNA was attached to positively charged BG the net charge of the BG/siRNA became almost neutral. The zeta potential of BG/siRNA in simulated gastric juice was measured as -0.68 ± 0.99 mV immediately after dissolving and -0.80 ± 1.96 mV after 6 hr of incubation (**Figure 16E and 16F**). The consistency of the zeta potential confirms the stability of siRNA payload within BG while dissolved into simulated gastric juice.

The stability of siRNA was further confirmed by the agarose gel electrophoresis. The band shows that the siRNA is stable while loaded within BG for at least 8 hr, both in simulated gastric juice (Figure 16D) whereas naked siRNA was found to be stable only for 2 hr after incubation with GJ (Supporting figure S10). siRNA stability analysis by nanodrop also supports western blotting results.

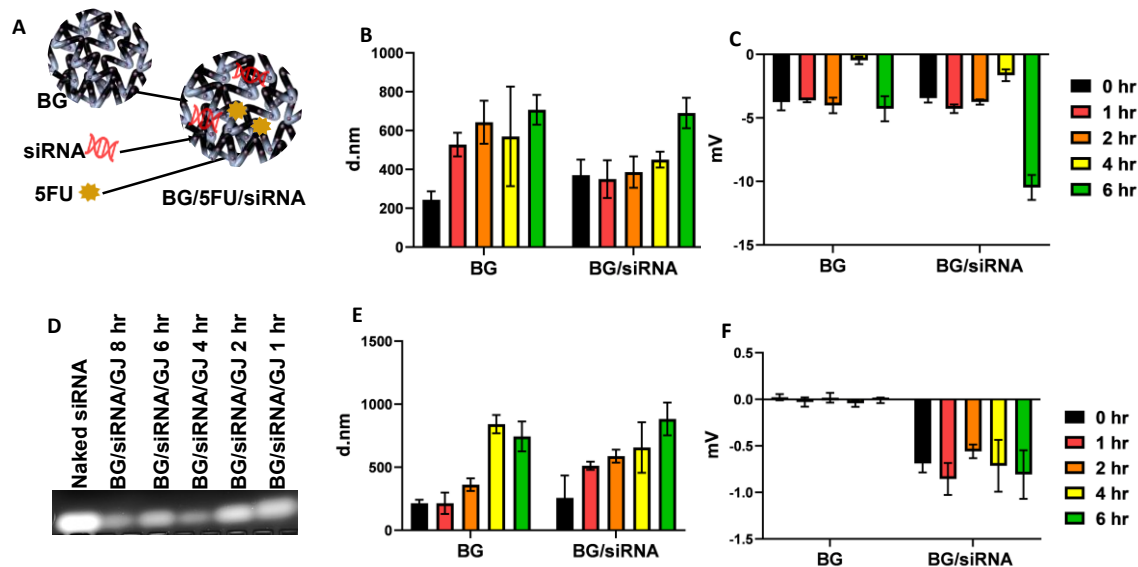


Figure 16: Stability of BG/siRNA particles in PBS and simulated gastric juice Schematic of the formulation (A). The size and zeta potential of BG and BG/siRNA in PBS and gastric juice were measured. Particle size distribution of BG and BG/siRNA was observed in PBS (B) and in simulated gastric juice (C) at 0, 1, 2, 4, and 6 hr. It was observed that after adding siRNA the size of BG increased initially at 0 hr measurement. (D) Gel electrophoresis analysis of naked siRNA and BG/siRNA incubated with simulated gastric juice up to 6 hr. The image showed that naked siRNA was not stable in simulated gastric juice even 1 hr after mixing, whereas siRNA/BG was found to be stable up to 6 hr after mixing with simulated gastric juice. Zeta potential of BG and siRNA with BG was also observed in PBS (E) and in simulated gastric juice (F). Zeta potential of

siRNA with BG showed negative charge constantly up to 6 hr. Data presented as mean \pm SEM, where $n=3$.

3.3.4 *In Vivo* imaging and biodistribution

To investigate the in-vivo biodistribution and organ accumulation coumarin-6 loaded BG was administered orally to the mice. It was examined that the BG can retain in the stomach for at least 6 hr (**Figure 17A**). To confirm further, the ex vivo image of organs was also taken after being euthanized. In both in vivo and ex vivo image BG was found to be retained only in the stomach. Except for the stomach it goes to the intestine and almost clears out from the intestine by 6th hr. BG retains the higher intensity of fluorescence in stomach through the 6 hr period. The result confirms that the BG is highly stomach specific which can maintain sustain release of hydrophobic payload (**Figure 17B**).

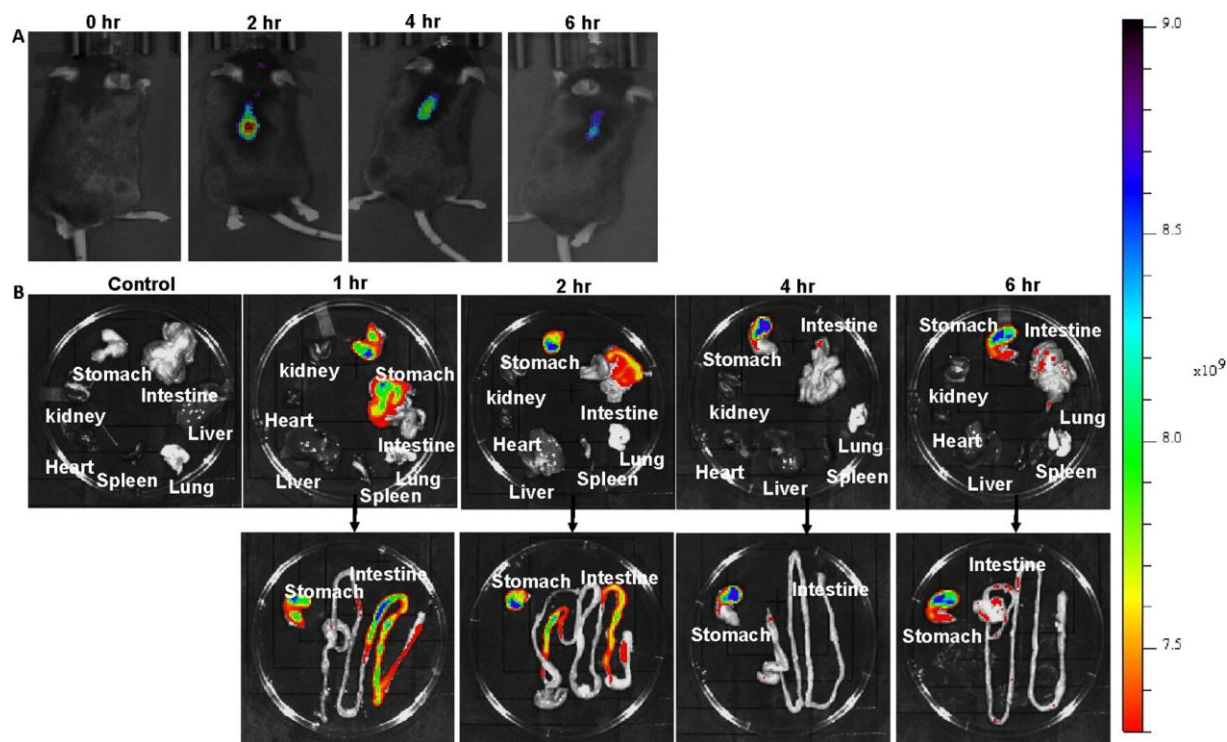


Figure 17: Fluorescence imaging to investigate biodistribution. (A) In vivo imaging shows noninvasive fluorescence-based localization of orally administered formulations. (B) Ex vivo images of the harvested organs show biodistribution of mice at pre-administration, after 2, 4 and 6 hr. Magnified images of GI tract show that BG particle remain in the stomach at least for 6 hr whereas slowly diffused via intestine.

3.3.5 Phenotypical *in vivo* treatment efficiency

Stomach cancer was induced to C57BL/6 mice by feeding N-methyl-N-nitrosourea (NMNU) in every other week for 5 weeks period (**Figure 18A**). The cancer induced mice were treated with saline, 5FU, siRNA, BG/5FU, BG/siRNA, and BG/5FU/siRNA via oral administration for 5 times at every 3rd day. The siRNA mentioned in the in-vivo experiment is Bcl2 siRNA. Before starting the treatment we investigate a control siRNA, Bcl2 siRNA I and Bcl2 siRNA II. We observed no change of Bcl2 with control and with Bcl2 siRNA II we got less reduction of Bcl2 expression compared to Bcl2 siRNA I. That's why we decided to move forward with Bcl2 siRNA I in further study. To investigate phenotype of therapeutic progress upon treatment with formulation in compared with saline treated mice, we have harvested the animal after 72 hr of 5th treatment. The size and weight of the stomach and intestine were measured immediately after the collection of the organs (**Figure 18B, 18C, and 18D**). A reduction in the size and weight of the stomach was observed in the untreated and oral siRNA treatment group, and this is an indication of a cancerous state. However, no significant difference in the size and weight of the intestine was observed (Supportin Figure S14), which is an indication of localized cancer specific to the stomach. In stomach cancer, the mice loss appetite due to reduced production of ghrelin hormone [140], hence we have observed weight loss in the untreated group when compared to the healthy control. On

top of that, cancer-mediated inflammation also results in the shrinkage of the organ, the stomach in this case. Reduction of size upon oral administration of nitroso compound is one of the phenotypic indications of induction of stomach cancer, and gaining the size back to normal which is comparable to healthy mice demonstrated the therapeutic efficacy of orally administered BG/siRNA/5FU formulation. The therapeutic efficacy of BG/siRNA/5FU has been further confirmed with histological and immunohistochemistry analysis with the tissues.

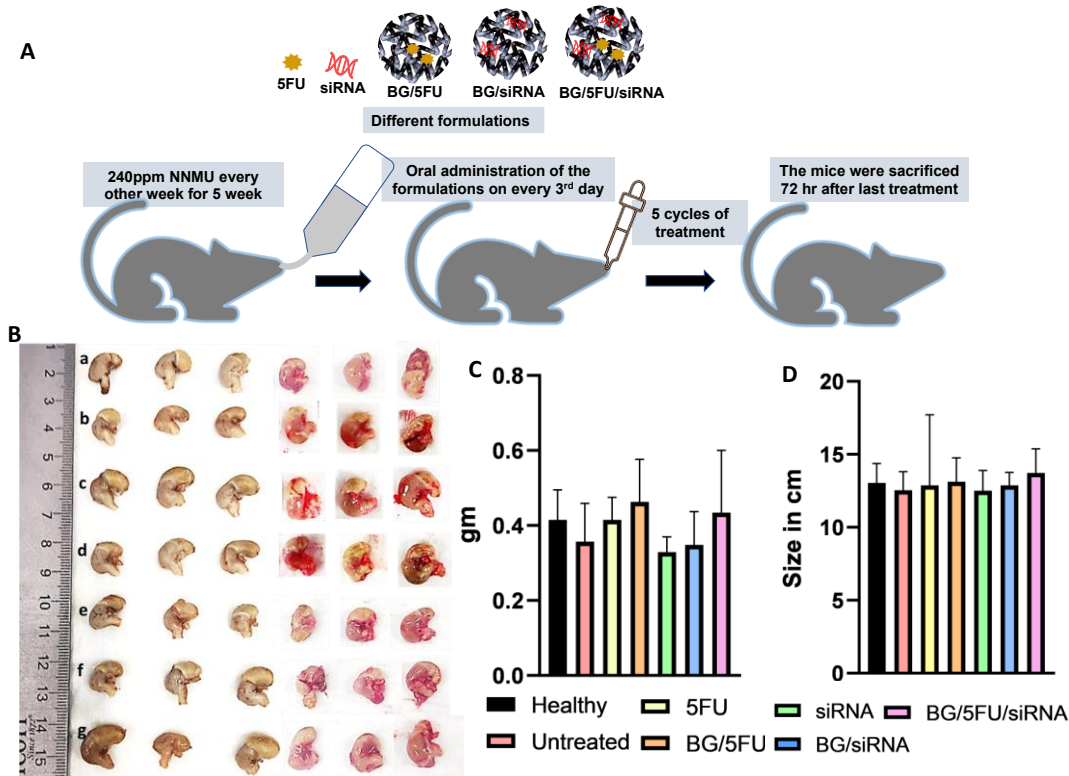


Figure 18: In vivo therapeutic efficacy. (A) Schematic of animal model preparation and treatment. (B) Image of the stomach collected from different group of treatment- Healthy (a), Untreated cancer (c), BG/5FU (c), 5FU (d), siRNA (e), BG/siRNA (f), BG/5FU/siRNA (g). (C) and (D) weight and size of the stomach. Data presented as mean \pm SEM, where $n=5$.

3.3.6 Oral Bcl2 siRNA causes in-vivo gene silencing and apoptosis.

A TUNEL assay was conducted to investigate the apoptosis within the tissue from the stomach of both healthy, untreated cancer, and treated cancer mice. We have observed significantly higher apoptosis in the stomach treated with BG/5FU/siRNA than the stomach treated with naked siRNA and both untreated and healthy control (**Figures 19A, and 19D**). No fragmented DNA was observed within the stomach tissues of healthy control and untreated mice, which indicates that oral co-delivery of siRNA and 5FU induces apoptosis in stomach cancer. Apoptosis was quantified by the mean fluorescent intensity and compared with healthy control and untreated control. The degree of apoptosis was calculated as 49, 107, 38, 62, and 131% for the 5FU, BG/5FU, siRNA, BG/siRNA, and BG/5FU/siRNA group relative to untreated control, respectively.

This reveals that apoptosis for BG/5FU/siRNA treated group was 69.46% more than BG/siRNA, and 95% more than free siRNA. To examine if the apoptosis was caused by downregulation of Bcl2, western blotting (WB) analysis was performed from the tissue lysate of different treatment groups. The WB data shows significant downregulation of Bcl2 gene resulted in by oral BG/5FU/siRNA compared to conventional naked oral siRNA (p-value <0.005), and untreated (p-value <0.0005). Data showed that the downregulation of Bcl2 gene expression was inversely proportional with the DNA fragmentation, which confirmed that the apoptosis resulted from the Bcl2 downregulation. Relative expression of Bcl2 was 1, 1.07 ± 0.008 , 1.24 ± 0.11 , 0.76 ± 0.02 , 0.88 ± 0.05 , 1.66 ± 0.14 , and 0.29 ± 0.04 for the healthy, untreated, 5FU, BG/5FU, siRNA, BG/siRNA, and BG/5FU/siRNA, respectively (**Figure 19B and Figure 19C**). This data confirms that BG-assisted orally administered siRNA was protected from the harsh gastric environment and was able to pass the mucus layer of the intestine and go into the site of action to silence the Bcl2 gene.

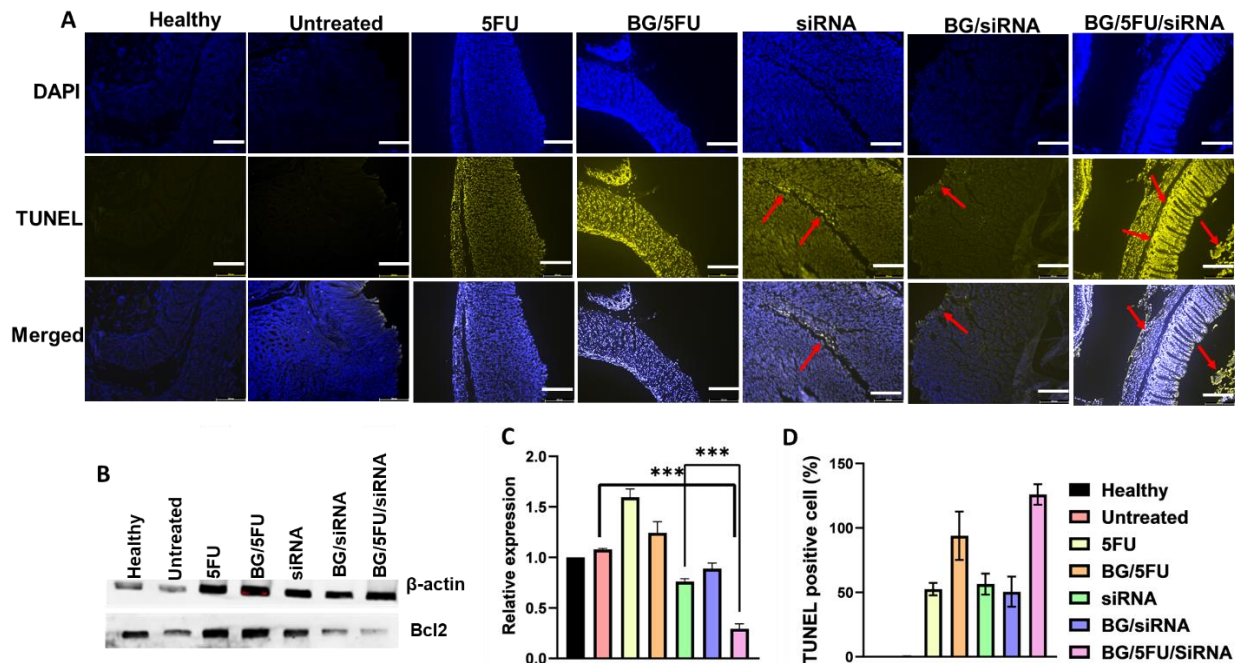


Figure 19: Immunohistochemistry to attribute apoptosis. (A) TUNEL assay shows broken nucleus (red arrow) in siRNA, BG/siRNA, and BG/5FU/siRNA groups. Scale bars represent 200 μ m. (B) Western blot analysis also shows reduced Bcl2 expression in BG/5FU/siRNA group compared to naked siRNA and BG/siRNA. The error bar represents the standard deviation. (C) Quantitative analysis of WB, and (D) apoptosis in percentage. Data presented as mean \pm SEM, where n=5. P value <0.0001 is denoted as ***.

The stomach tissue was also utilized to analysis Bcl2 protein expression using immunohistochemistry (IHC). The anti-Bcl2 positive area was quantified in comparison to the whole tissue section stained with DAPI. The area percentage of Bcl2 antibodies for healthy, untreated, 5FU, BG/5FU, siRNA, BG/siRNA, and BG/5FU/siRNA was 1.19%, 1.46%, 1.22%, 1.45%, 0.97%, 1.11%, and 0.47%, respectively (**Figure 20A**). To measure the relative expression of Bcl2 on the tissue section the data was calculated and compared with the stomach tissue

collected from the healthy mice, where Bcl2 expression in healthy mice was considered as 100% (**Figure 20B**). The immunofluorescence data reciprocates the same as WB data. Oral delivery of BG/5FU/siRNA resulted in the lowest expression of Bcl2 as observed in WB and immunofluorescence images of tumor tissue. In the immunofluorescence image, we have observed higher Bcl2 expression in the untreated tissue section. The untreated section had 51.20% more expression of Bcl2 than compared to the healthy control. The mice treated with BG/5FU/siRNA had 111.45%±1.6 less expression of Bcl2 compared to untreated cancer and 68.39% less expression than mice treated with naked siRNA. Mice treated with BG/siRNA also causes less expression of Bcl2 confirmed by WB and ICH but the combination of siRNA and 5FU resulted in higher Bcl2 inhibition efficiency. This confirms that siRNA with 5FU produces a synergistic effect in downregulating the Bcl2 proteins.

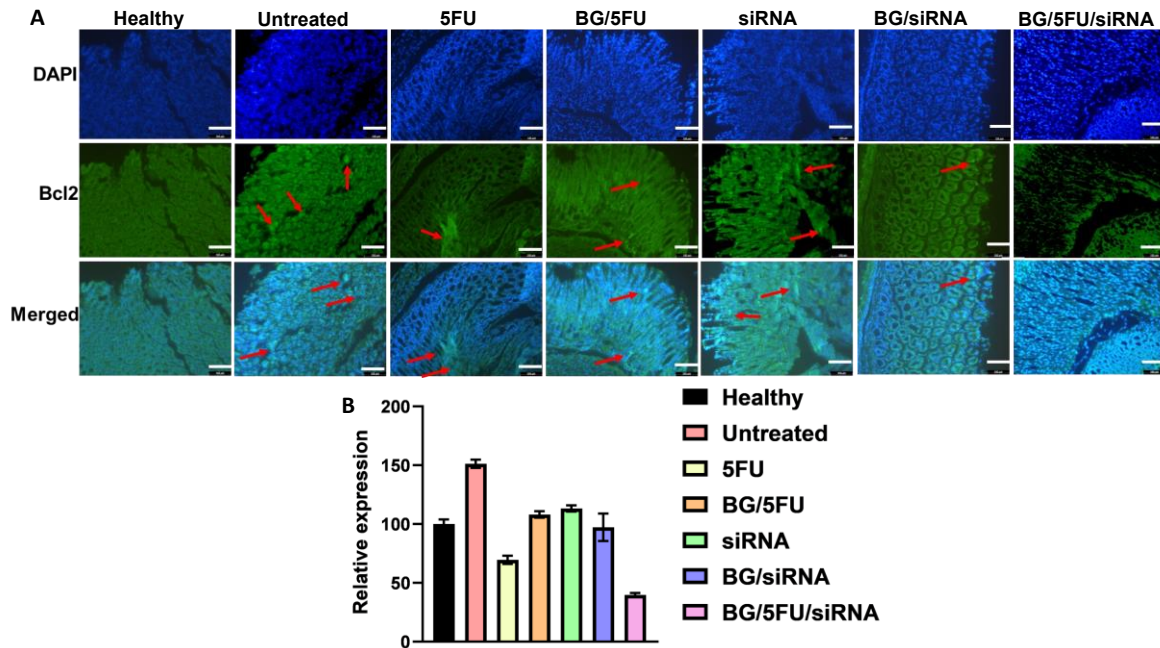


Figure 20: Immunohistochemistry to attribute expression of Bcl2 protein. (A) Immunohistochemistry for Bcl-2 protein shows higher expression of Bcl-2 in untreated mice stomachs (red arrow). The naked oral siRNA treatment group also had more Bcl-2 expression than

BG/siRNA and BG/5FU/siRNA. The scale bar represents 100 μ m. (B) Quantification of Bcl2 immunofluorescence data analysis was presented. Data presented as mean \pm SEM, where n=5.

3.3.7 Therapeutic Efficacy In Vivo

Cell proliferation marker was measured by immunofluorescence assay to evaluate the antitumor effect of the formulations. Ki67 is a protein found in the nucleus of the cancer cell. Detection of Ki67 expression has been a reliable indicator for cancer proliferation and prognosis in cancers including stomach cancer [141]. Therefore, Ki67 is considered an important indicator of therapeutic assessment and chemosensitivity. Studies show that higher expression of Ki67 corresponds with a low chemosensitivity [142]. In this study, the stomach section from different treatment groups of mice was subjected to immunofluorescence for Ki67 protein analysis. The untreated stomach showed higher expression of Ki67 (yellow arrow) and with treatment, specifically with BG/5FU/siRNA, the expression of Ki67 expression was reduced significantly (**Figure 21A**). The protein expression was quantified from immunofluorescence images. The area with Ki67 positive cells was measured in compared to the whole tissue section with DAPI stained. The area (%) of healthy, untreated, 5FU, BG/5FU, siRNA, BG/siRNA, and BG/5FU/siRNA was measured as 100%, 446.86%, 221.44%, 155.61%, 498.85%, 278.82%, and 90.27%, respectively. The Ki67 expression in the untreated group was 346.86% higher in the untreated group compared to the healthy control. Whereas, with BG/5FU/siRNA treatment group the expression was reduced by 356.59% when compared to the stomach of untreated cancer mice (**Figure 21B**). We have also observed partial expression of Ki67 to the group of mice treated with 5FU which is comparatively higher than mice treated with BG/5FU/siRNA [143].

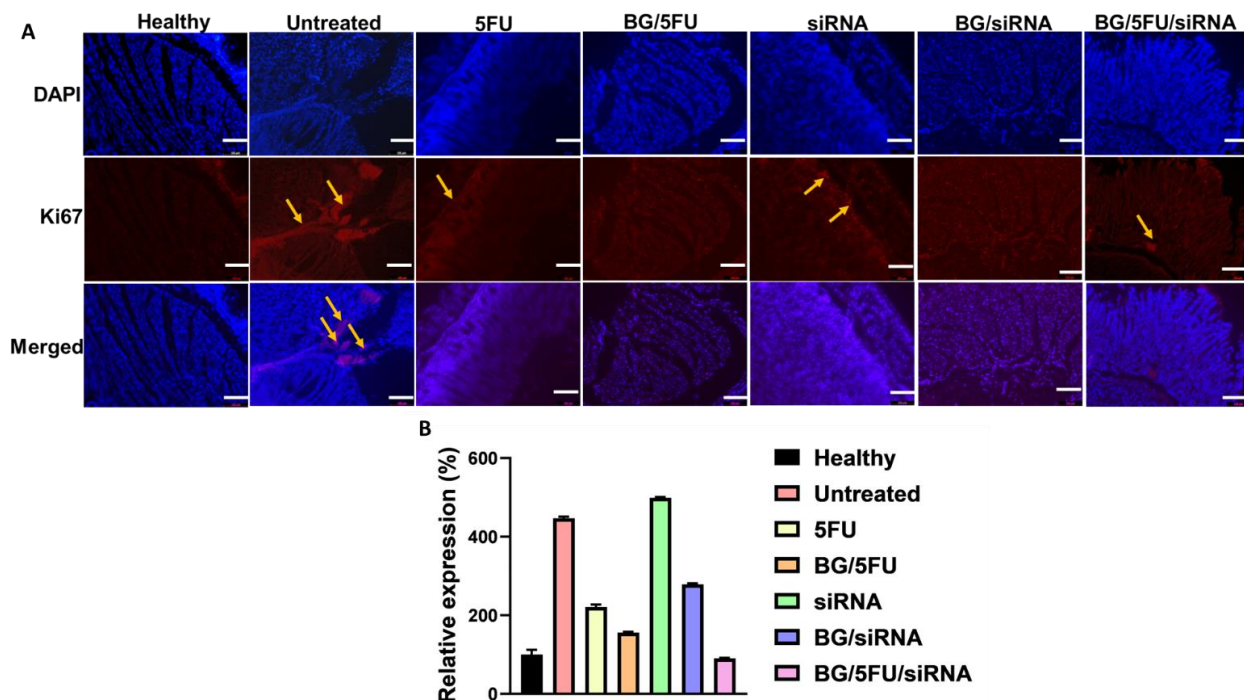


Figure 21: Immunofluorescence for *ki67* of stomach sections of different treatment groups. (A) A higher expression of *ki67* (yellow arrow) was observed in untreated group, whereas after treatment the expression got reduced specially with BG/5FU/siRNA formulation. Scale bar represents 100 μm . (B) *Ki67* expression was quantified compared to healthy control. Data presented as mean \pm SEM, where $n=5$.

H&E staining with stomach tissue was conducted to measure the anticancer therapeutic effect of stomach cancer as well as the inflammatory effect among the tissue/cell around the cancer. Figure 9 represents the H&E staining image of the same stomach section in different magnifications. To visualize the whole tumor area the image was taken at 10X magnification and to understand the pathophysiology a higher magnification image was taken at 40x by a slide scanner. As seen in **Figure 22**, the presence of tumors in the stomach as indicated by the black arrow. Moreover, a large intramucosal tumor was observed in the stomach of untreated cancer mice, and cancer mice

treated with siRNA and BG/siRNA. However, no visible tumor was observed in the stomach of the cancer mice treated with BG/5FU/siRNA. The total remission of cancer indicates the ability and anticancer efficacy of oral delivery of the 5FU/siRNA assisted by BG.

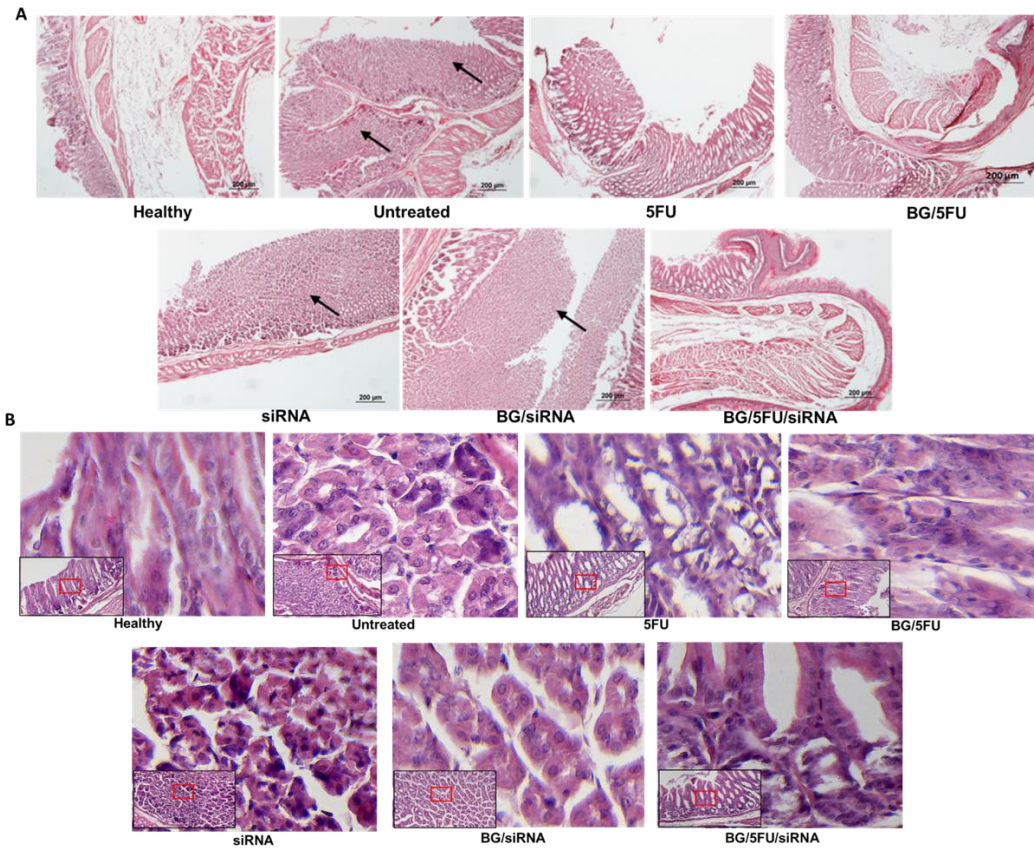


Figure 22: Histology of stomach. (A) The histological staining (H&E) shows a growth (blue arrow) in the untreated section, while after treatment with 5FU, 5FU/BG, and BG/5FU/siRNA the tumor region got significantly reduced. (B) H&E staining of stomach cancer sections with 40X magnification. The red rectangular area was cropped and magnified for better morphological understanding. The untreated, naked siRNA, and BG/siRNA shows the feature of adenocarcinoma. The section of BG/5FU/siRNA treatment group almost resemblance as healthy stomach.

In figure 19B, the images were taken at 40X, and then the red rectangular area was cropped to magnify for better and clearer visualization of the tissue morphology. The higher magnification of

the images shows adenocarcinoma in the untreated group where there was higher staining of nuclei, irregular glandular space, and distortion of normal epithelial structure [144]. Signet ring cells were also found in the untreated stomach cancer tissue. No improvement of tumor was observed with naked siRNA treated stomach section. However, mice treated with BG/5FU/siRNA and BG/5FU demonstrated that the cellular structure almost resembled to healthy stomach.

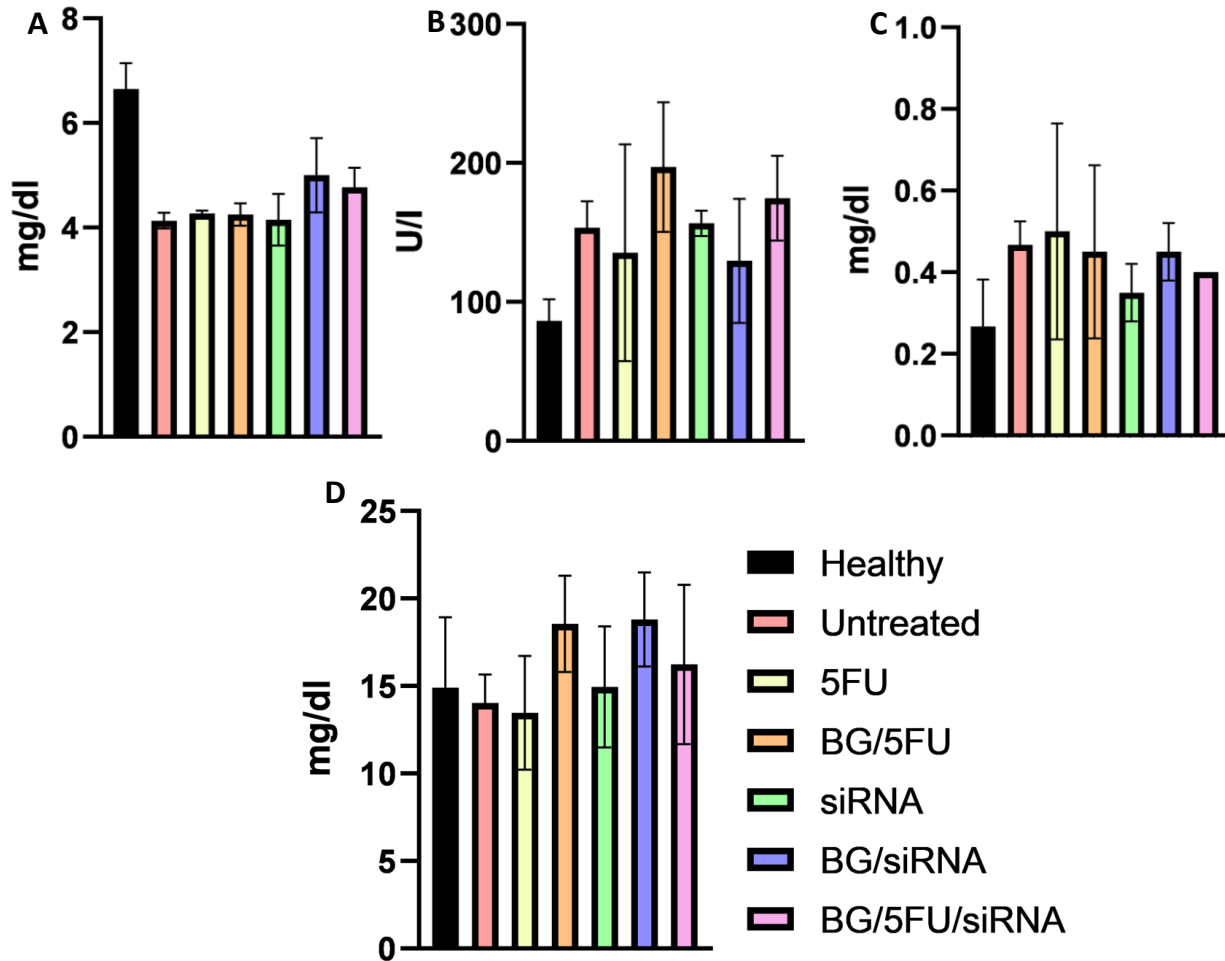


Figure 23: Serum biochemistry to demonstrate toxicity. Serum analysis for (A) total protein (TP), (B) alanine aminotransferase (ALT), (C) creatinine, and (D) blood urea nitrogen (BUN) does not show any significant difference of the treatment group with the untreated. Data presented as mean \pm SEM, where $n=5$.

3.3.8 Serum biochemistry and toxicity

To examine the systemic side effect mediated by the treatment modalities, serum analysis was conducted with the blood collected from both healthy controls, untreated, and treatment groups. Liver and kidney toxicity was measured by quantifying the presence of total protein (TP), alanine aminotransferase (ALT), creatinine, and blood urea nitrogen (BUN) in blood and compared with healthy control. As depicted in **figure 23**, none of the parameters were found out of the reference range, which confirms that the oral formulations are not significantly toxic to the liver and kidney. As, the treatments were given orally, the H&E staining of the small intestine was also done, and no toxicity was observed in the histological section of the duodenum, jejunum, and ileum of the different treatment groups (**Supplementary figure S15**).

3.4 CONCLUSIONS

Stomach specific oral delivery of anticancer therapeutics can enhance the retention duration of the therapeutic modalities thus improving the therapeutic effect by increasing drug concentration within the site of cancer. 5FU is the first-line treatment of choice for stomach cancer, however, toxic effect and development of resistance are the major concern. Considering the risk to benefit ratio of using 5FU, there is a concern about their broad-spectrum application for various cancer. In this study, oral delivery of 5FU and Bcl2 siRNA were used to enhance therapeutic effect by synergistic effect of 5FU and siRNA. RNAi is gaining popularity as an anti-cancer treatment option because of selective gene silencing and no off-targeting effect which provides better therapeutic efficacy and fewer side effect. To overcome the challenges associated with the oral delivery of siRNA, we have developed a nano carrier composed of BG, a highly biocompatible polysaccharide. The BG was not only protecting the payload of siRNA to maintain their stability but enhancing their retention within the stomach for at least 6 hr. The co-delivery of

BG/5FU/siRNA was shown to downregulate Bcl2 expression and apoptosis of cancer cells. TUNEL assay confirms the apoptosis of tumor cells. Ki67 marker was also reduced with the treatment and histological staining shows almost complete remission of the tumor region with BG/5FU/siRNA formulation. Our findings demonstrate that this oral therapeutic modality has potential for treating stomach cancer and the co-delivery of siRNA and 5FU is more effective than individual entities such as free siRNA and 5FU. However, the pathway of producing a synergistic effect in silencing Bcl2 has not been examined in this study. Therefore, we aim to continue this study to understand the mechanism of action of 5FU and Bcl2 siRNA combination.

SUPPLEMENTARY INFORMATION

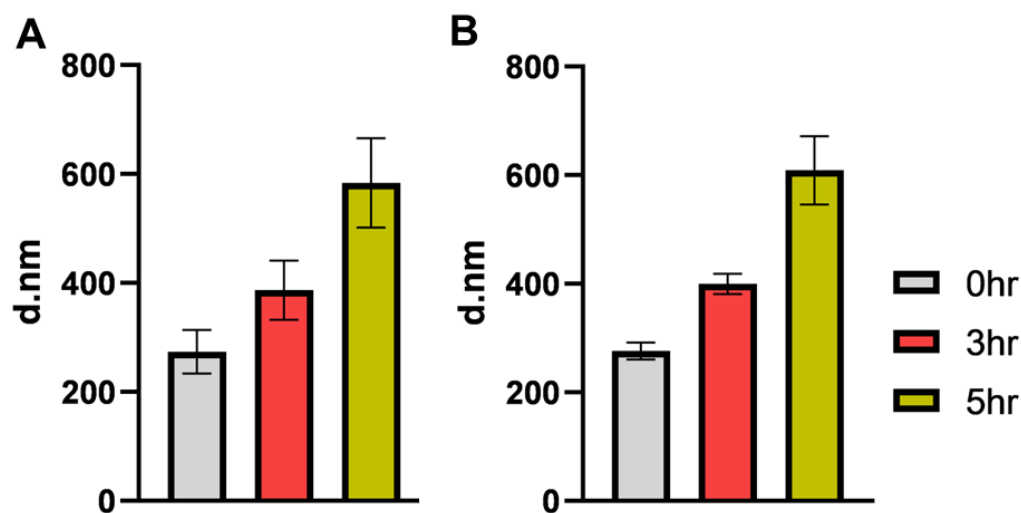


Figure S 7: Size of BG in PBS (A) and Gastric Juice (B). In both PBS and GJ size tends to increase with time.

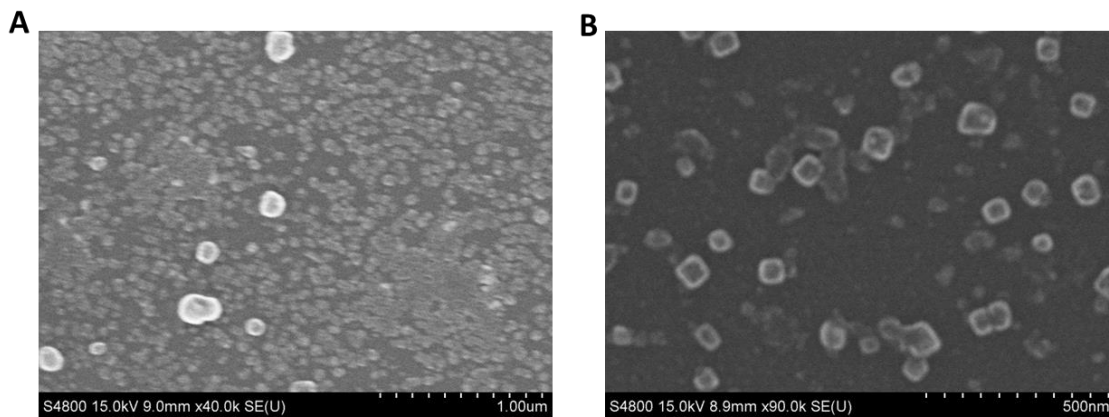


Figure S 8: SEM image of BG/FU (A) and BG/siRNA (B)

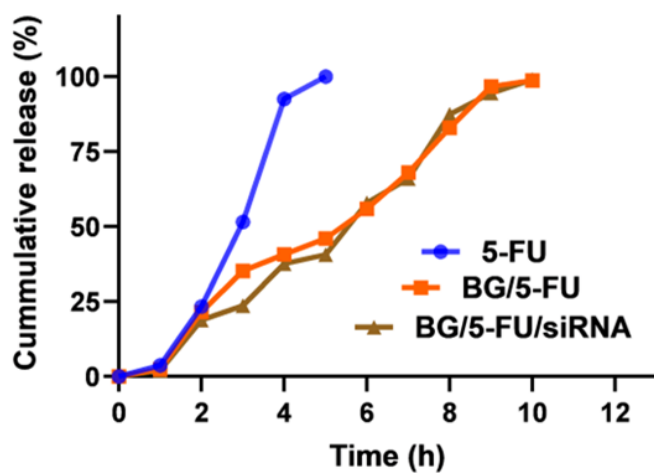


Figure S 9: Release study of 5FU. Free 5FU shows a burst release in 2nd hour compared to the BG/siRNA and BG/5FU/siRNA. BG/5FU and BG/5FU/siRNA shows a sustain release up to 10hrs.

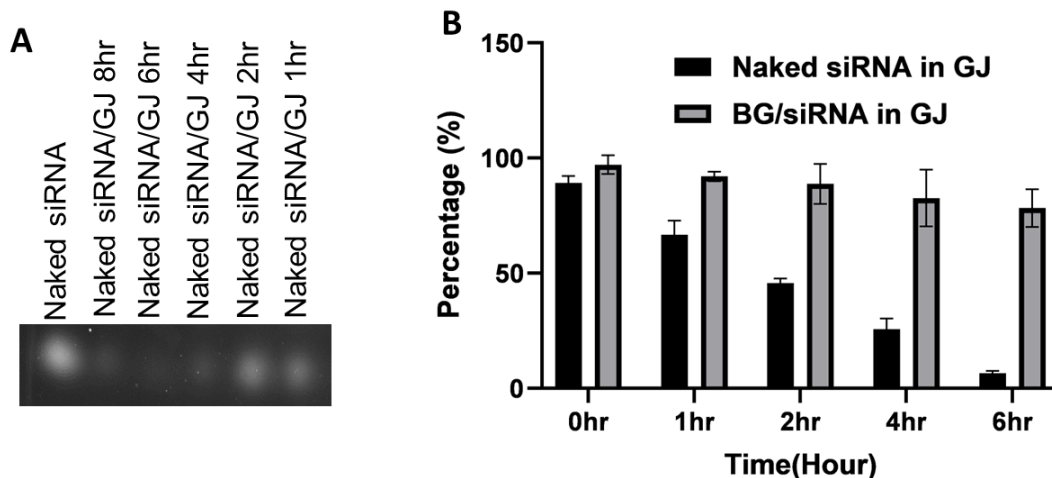


Figure S 10: Stability of siRNA formulation in BG. Stability of siRNA formulation in BG. (A) Agarose gel electrophoresis of naked siRNA in GJ after incubating for 1,2,4,6 and 8hrs. (B) Nanodrop measurement of siRNA shows that naked siRNA without BG is not stable in GJ.

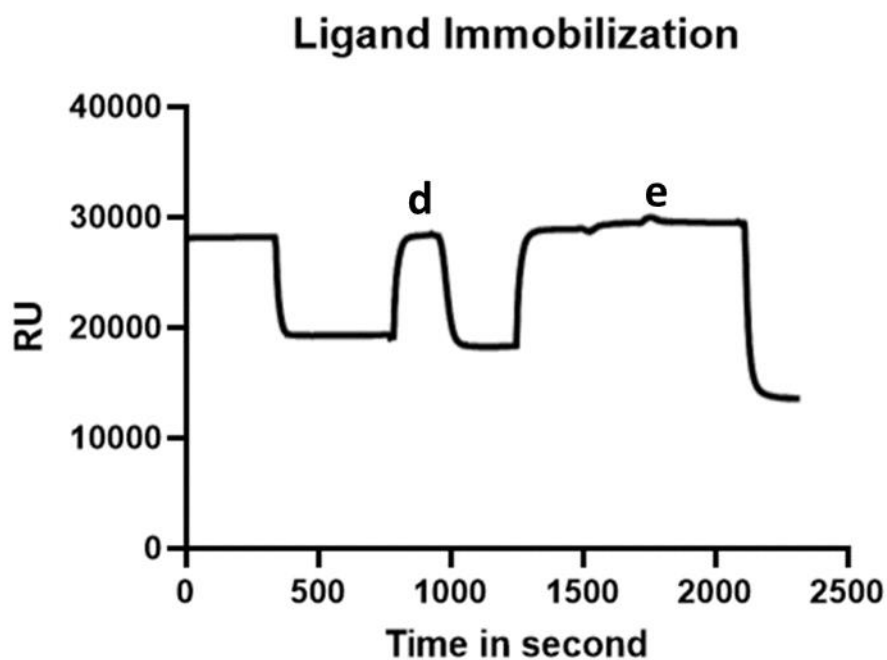


Figure S 11: Surface plasmon resonance (SPR) analysis for binding affinity of BG and mucin. Shows the picks for (d) EDC/NHS and (e) BG. BG was used as ligand over COOH-Au chip.

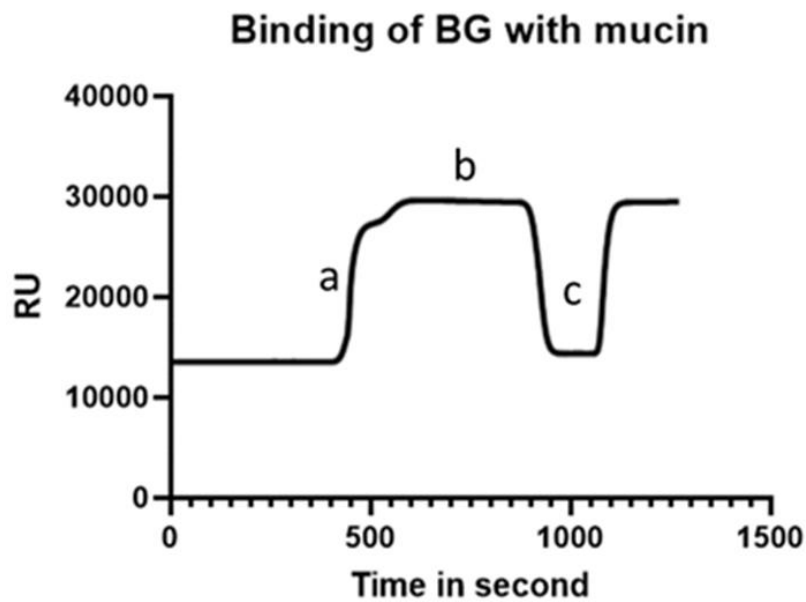


Figure S 12: Figure S1.6. SPR analysis shows the binding of BG to mucin. Curve- a) indicates association of BG with mucin, b) represents the plateau and where BG continues to bind with mucin and c) indicates the dissociation of BG with mucin.

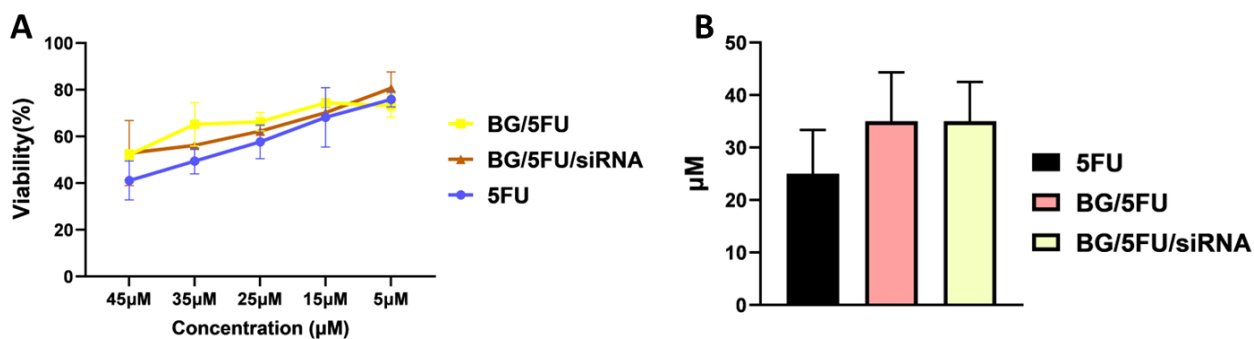


Figure S 13: Cellular viability (A) and IC₅₀ (B) value of 5FU formulations. Cellular viability (A) and IC₅₀ (B) value of 5FU formulations. The IC₅₀ value of 5FU, BG/5FU and BG/5FU/siRNA was found to be around 25µM± 8.3, 35µM± 9.3 and 35µM±7.4 respectively.

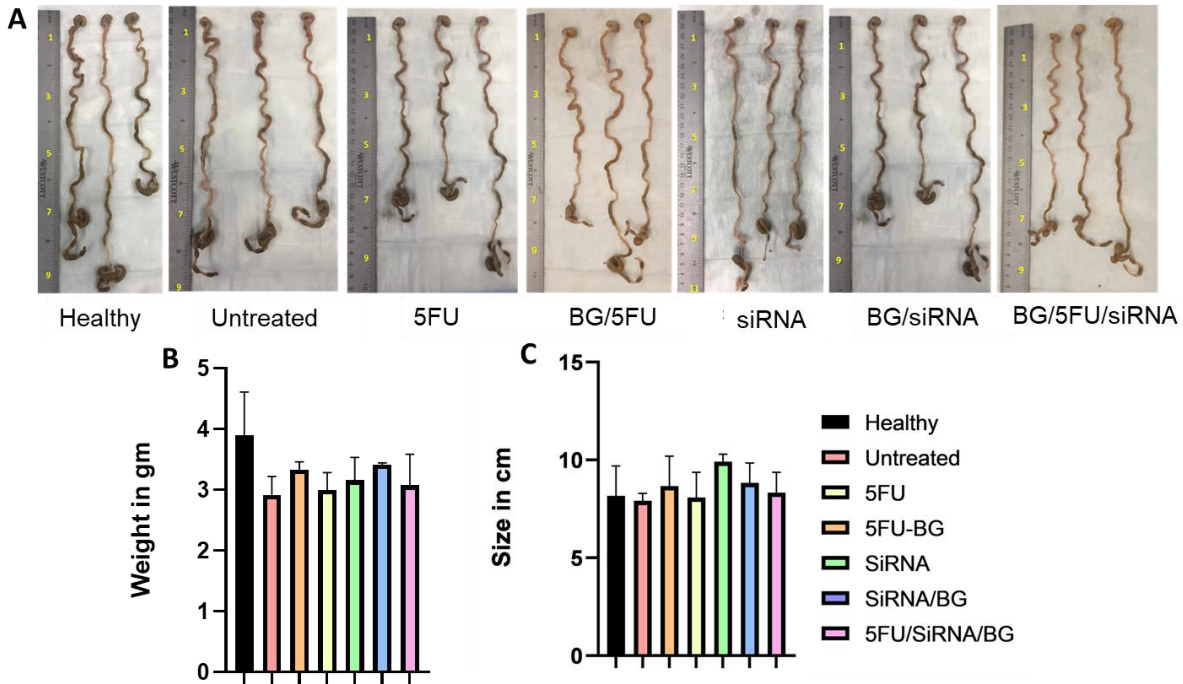


Figure S 14: Size and weight of intestine post-treatment. (A) Intestine collected from different treatment group. Weight (B) and size (C) of the collected intestine were measured. No significant difference was found between the treatment and untreated group.

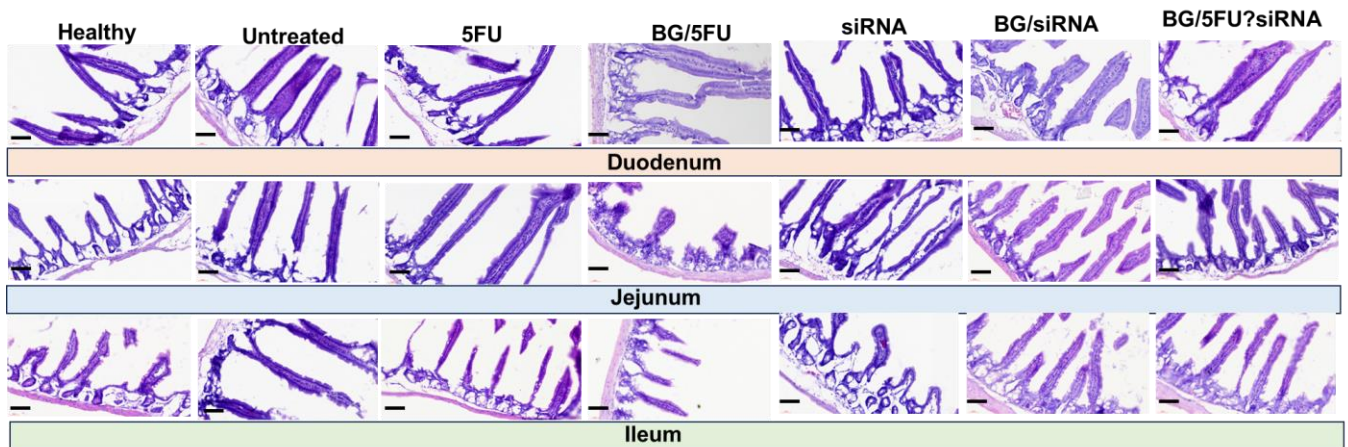


Figure S 15: H&E staining of intestine shows no significant toxicity. H&E staining of duodenum, jejunum, and ileum of different treatment groups. No significant toxic effect was observed in the intestinal section.

Summary:

The objective of this thesis was to figure out a safe treatment option for cancer and fibrosis as both these diseases have a very high number of mortality rate and very bad prognosis. To overcome the limitations of the current treatment options we used a nanocarrier to deliver the drug. Here Bcl2 inhibitors were used to load the drug on the specific targeted site and used Bcl2 inhibitors as therapeutic modality.

In the first project we focused on developing a myofibroblast targeted treatment option for kidney fibrosis. The conventional treatments are mostly symptomatic. Till now there has been no available treatment option for kidney fibrosis which would reverse the fibrosis process. In this purpose, we designed PLGA nanoparticle and modified the surface of nanoparticle with AT2 peptide and loaded Navi inside as a therapeutic modality. Navi is a very potent drug for both cancer and fibrosis. However, due to the hematological side effects it is still not FDA approved and is given orally to limit the side effects. The result showed that this AT2 targeted treatment option with Bcl2 inhibition was able to reverse kidney fibrosis process in fibrosed mice model at the same time it found that PLGA coating prevent the side effect specifically the hematological side effect. This study provided a much-needed treatment for kidney fibrosis. Although, more study needs to be done to proceed to the clinical trial, to be available for clinical use. However, it creates a new horizon of research with Bcl2 inhibition. No study has been done before with Bcl2 inhibition for kidney fibrosis.

- Bcl2 inhibition can induce apoptosis in fibrosed kidney cell and reverse it back to normal.
- Navi does not produce thrombocytopenia when delivered with PLGA coated nanoparticle.
- AT2 conjugation provides the kidney selective ability to the particle.
- A new treatment for kidney fibrosis.

In the second project we prepared an alternative stomach targeted oral treatment approach for stomach cancer. We have used Bcl2 siRNA to knock down Bcl2 gene and 5FU and loaded the therapeutics inside BG nanoparticle. The result of our study showed that the Bcl2 siRNA and 5FU produce synergistic effect in creating apoptosis and provided better therapeutic result compared to only siRNA or free 5FU. On top of that, BG nanoparticle helped longer retention of drugs in the site of cancer and reduced random distribution of drug which helped in getting better therapeutic efficacy with lesser dosages and demand less frequency and side effect. This study enabled oral siRNA-based chemotherapy for stomach cancer. RNAi has been revolutionary in cancer treatment as it could target a specific gene that causes cancer. However, oral delivery of nucleic acid is always a challenge as nucleic are not stable in intestinal milieu. BG were able maintain the stability of siRNA without any chemical modification and changing the properties intact. It provides a platform for research for oral delivery of other nucleic acids such as mRNA or other RNAi or protein molecules. The innovation of this study is listed below,

- 5FU and Bcl2 siRNA produce synergistic effect on apoptosis and provide better therapeutic effects.
- BG acts as a shield and provides the stability to the siRNA in acidic stomach environment.
- BG nanoparticle is more stomach specific compared to any other part of the body containing mucous.
- BG NP facilitates the transportation of hydrophobic small molecule like 5FU through the intestine.

In summary this thesis focused on developing a nanoparticle mediated improved treatment option for stomach cancer and kidney fibrosis with Bcl2 inhibition. Both the treatments were successful in terms of therapeutic efficacy and did not generate the usual toxic effect. We exhibited that Bcl2 inhibition of cancer cell and fibrosed cell can treat stomach cancer and reverse fibrosis.

Additionally, efforts to improve access to cancer care and reduce healthcare disparities are essential to ensure that all patients receive the best possible treatment options. Addressing these limitations will require continued research efforts to deepen our understanding of fibrosis pathogenesis, develop more effective and targeted therapies, improve diagnostic tools and biomarkers, and optimize treatment approaches for individual patients. Additionally, early detection and intervention strategies are needed to prevent or minimize fibrosis progression and improve patient outcomes. However, it's important to note that while preclinical studies are encouraging, further research, including clinical trials, is needed to fully evaluate the safety and efficacy of Navitoclax in cancer and fibrosis treatment in humans.

Acknowledgement

We acknowledge funding by the Cancer Prevention Research Institute of Texas (CPRIT) through a Texas Regional Excellence in Cancer Award (TREC) under Award No. PR210153, and the National Institutes of Health (NIH) under Award No. R03OD032624. The contents of this paper are solely the authors' responsibility and do not necessarily represent the official views of NIH. The author thanks Raj Kumar for SEM images. Sayantani Chakraborty and Lela Vukovic conducted an experiment related to molecular docking and simulations. The content for graphics and cartoons including table of contents were obtained from smart.servier.com and Microsoft PowerPoint.

Reference:

1. Elmore S. Apoptosis: a review of programmed cell death. *Toxicol Pathol* 2007;**35**:495–516.
2. Codispoti B, Makeeva I, Sied J *et al*. Should we reconsider the apoptosis as a strategic player in tissue regeneration? *Int J Biol Sci* 2019;**15**:2029–36.
3. Singh R, Letai A, Sarosiek K. Regulation of apoptosis in health and disease: the balancing act of BCL-2 family proteins. *Nat Rev Mol Cell Biol* 2019;**20**:175–93.
4. Tang D, Kang R. Chapter 2 - Cell death: machinery and regulation. In: Liao DBT-M of CD and O for TD (ed.). *Perspectives in Translational Cell Biology*. Academic Press, 2022, 47–64.
5. Bender T, Martinou J-C. Where killers meet--permeabilization of the outer mitochondrial membrane during apoptosis. *Cold Spring Harb Perspect Biol* 2013;**5**:a011106.
6. Todaro M, Lombardo Y, Francipane MG *et al*. Apoptosis resistance in epithelial tumors is mediated by tumor-cell-derived interleukin-4. *Cell Death Differ* 2008;**15**:762–72.
7. Um H-D. Bcl-2 family proteins as regulators of cancer cell invasion and metastasis: a review focusing on mitochondrial respiration and reactive oxygen species. *Oncotarget* 2016;**7**:5193–203.
8. Perini GF, Ribeiro GN, Pinto Neto JV *et al*. BCL-2 as therapeutic target for hematological malignancies. *J Hematol Oncol* 2018;**11**:65.
9. Valentini E, Di Martile M, Brignone M *et al*. Bcl-2 family inhibitors sensitize human cancer models to therapy. *Cell Death Dis* 2023;**14**:441.
10. González-Puertos VY, Hernández-Pérez E, Nuño-Lámbarri N *et al*. Bcl-2 overexpression in hepatic stellate cell line CFSC-2G, induces a pro-fibrotic state. *J Gastroenterol Hepatol* 2010;**25**:1306–14.
11. Saile B, Matthes N, El Armouche H *et al*. The bcl, NFκB and p53/p21WAF1 systems are

involved in spontaneous apoptosis and in the anti-apoptotic effect of TGF- β or TNF- α on activated hepatic stellate cells. *Eur J Cell Biol* 2001;**80**:554–61.

12. Wilson WH, O'Connor OA, Czuczman MS *et al.* Navitoclax, a targeted high-affinity inhibitor of BCL-2, in lymphoid malignancies: a phase 1 dose-escalation study of safety, pharmacokinetics, pharmacodynamics, and antitumour activity. *Lancet Oncol* 2010;**11**:1149–59.

13. Mohamad Anuar NN, Nor Hisam NS, Liew SL *et al.* Clinical Review: Navitoclax as a Pro-Apoptotic and Anti-Fibrotic Agent. *Front Pharmacol* 2020;**11**, DOI: 10.3389/fphar.2020.564108.

14. Cooley JC, Javkhlan N, Wilson JA *et al.* Inhibition of antiapoptotic BCL-2 proteins with ABT-263 induces fibroblast apoptosis, reversing persistent pulmonary fibrosis. *JCI insight* 2023;**8**, DOI: 10.1172/jci.insight.163762.

15. McElhinney K, Irnaten M, O'Brien C. p53 and Myofibroblast Apoptosis in Organ Fibrosis. *Int J Mol Sci* 2023;**24**, DOI: 10.3390/ijms24076737.

16. Jin H, Yoo Y, Kim Y *et al.* Radiation-Induced Lung Fibrosis: Preclinical Animal Models and Therapeutic Strategies. *Cancers (Basel)* 2020;**12**, DOI: 10.3390/cancers12061561.

17. Gazitt Y, Rothenberg ML, Hilsenbeck SG *et al.* Bcl-2 overexpression is associated with resistance to paclitaxel, but not gemcitabine, in multiple myeloma cells. *Int J Oncol* 1998;**13**:839–48.

18. Roberts AW, Seymour JF, Brown JR *et al.* Substantial Susceptibility of Chronic Lymphocytic Leukemia to BCL2 Inhibition: Results of a Phase I Study of Navitoclax in Patients With Relapsed or Refractory Disease. *J Clin Oncol* 2012;**30**:488–96.

19. Puglisi M, Molife LR, de Jonge MJ *et al.* A Phase I study of the safety, pharmacokinetics and efficacy of navitoclax plus docetaxel in patients with advanced solid tumors. *Future Oncol*

2021;**17**:2747–58.

20. Rawla P, Barsouk A. Epidemiology of gastric cancer: Global trends, risk factors and prevention. *Prz Gastroenterol* 2019, DOI: 10.5114/pg.2018.80001.

21. Chang ET, Gomez SL, Fish K *et al.* Gastric cancer incidence among hispanics in California: Patterns by time, nativity, and neighborhood characteristics. *Cancer Epidemiol Biomarkers Prev* 2012, DOI: 10.1158/1055-9965.EPI-11-1208.

22. Rogers JE, Ajani JA. Recent advances in the management of gastric adenocarcinoma patients. *Fac Rev* 2023;**12**:2.

23. Huang R, Fu P, Ma L. Kidney fibrosis: from mechanisms to therapeutic medicines. *Signal Transduct Target Ther* 2023;**8**:129.

24. Sesso R, Belasco AG, Ajzen H. Late diagnosis of chronic renal failure. *Brazilian J Med Biol Res = Rev Bras Pesqui medicas e Biol* 1996;**29**:1473–8.

25. US FDA approves Jardiance® for the treatment of adults with chronic kidney disease | Eli Lilly and Company.

26. Tewabe A, Abate A, Tamrie M *et al.* Targeted Drug Delivery - From Magic Bullet to Nanomedicine: Principles, Challenges, and Future Perspectives. *J Multidiscip Healthc* 2021;**14**:1711–24.

27. Ezike TC, Okpala US, Onoja UL *et al.* Advances in drug delivery systems, challenges and future directions. *Heliyon* 2023;**9**:e17488.

28. Baryakova TH, Pogostin BH, Langer R *et al.* Overcoming barriers to patient adherence: the case for developing innovative drug delivery systems. *Nat Rev Drug Discov* 2023;**22**:387–409.

29. Hines DJ, Kaplan DL. Poly(lactic-co-glycolic) acid-controlled-release systems: experimental and modeling insights. *Crit Rev Ther Drug Carrier Syst* 2013;**30**:257–76.

30. Alsaab HO, Alharbi FD, Alhibs AS *et al.* PLGA-Based Nanomedicine: History of Advancement and Development in Clinical Applications of Multiple Diseases. *Pharmaceutics* 2022;**14**, DOI: 10.3390/pharmaceutics14122728.
31. Xu Z, Li W, Han J *et al.* Angiotensin II induces kidney inflammatory injury and fibrosis through binding to myeloid differentiation protein-2 (MD2). *Sci Rep* 2017;**7**:44911.
32. Ruiz-Ortega M, Rupérez M, Esteban V *et al.* Angiotensin II: a key factor in the inflammatory and fibrotic response in kidney diseases. *Nephrol Dial Transplant* 2006;**21**:16–20.
33. Traulsen J, Zagami C, Daddi AA *et al.* Molecular modelling of the gastric barrier response, from infection to carcinogenesis. *Best Pract Res Clin Gastroenterol* 2021;**50–51**:101737.
34. Wynn TA. Common and unique mechanisms regulate fibrosis in various fibroproliferative diseases. *J Clin Invest* 2007;**117**:524–9.
35. Liu F, Zhuang S. New Therapies for the Treatment of Renal Fibrosis. In: Liu B-C, Lan H-Y, Lv L-L (eds.). *Renal Fibrosis: Mechanisms and Therapies. Advances in Experimental Medicine and Biology*. Singapore: Springer Singapore, 2019, 625–59.
36. Rosenbloom J, Mendoza FA, Jimenez SA. Strategies for anti-fibrotic therapies. *Biochim Biophys Acta - Mol Basis Dis* 2013;**1832**:1088–103.
37. Gifford CC, Lian F, Tang J *et al.* PAI-1 induction during kidney injury promotes fibrotic epithelial dysfunction via deregulation of klotho, p53, and TGF- β 1-receptor signaling. *FASEB J* 2021;**35**:e21725.
38. Chronic Kidney Disease in the United States, 2021.
39. Kidney Disease Statistics for the United States | NIDDK.
40. Johansen KL, Chertow GM, Foley RN *et al.* US Renal Data System 2020 Annual Data Report: Epidemiology of Kidney Disease in the United States. *Am J Kidney Dis* 2021;**77**:A7–8.

41. Klinkhammer BM, Goldschmeding R, Floege J *et al.* Treatment of renal fibrosis—turning challenges into opportunities. *Adv Chronic Kidney Dis* 2017;**24**:117–29.
42. Davison SN, Tupala B, Wasyluk BA *et al.* Recommendations for the Care of Patients Receiving Conservative Kidney Management. *Clin J Am Soc Nephrol* 2019;**14**:626–34.
43. Chen TK, Knicely DH, Grams ME. Chronic Kidney Disease Diagnosis and Management. *JAMA* 2019;**322**:1294.
44. Knipe RS, Tager AM, Liao JK. The Rho kinases: critical mediators of multiple profibrotic processes and rational targets for new therapies for pulmonary fibrosis. *Pharmacol Rev* 2015;**67**:103–17.
45. Xi Y, Xu P-F. Therapeutic potentials of fasudil in liver fibrosis. *World J Gastroenterol* 2021;**27**:7859–61.
46. Moshirfar M, Parker L, Birdsong OC *et al.* Use of Rho kinase Inhibitors in Ophthalmology: A Review of the Literature. *Med hypothesis, Discov Innov Ophthalmol J* 2018;**7**:101–11.
47. Horowitz JC, Thannickal VJ. Mechanisms for the resolution of organ fibrosis. *Physiology* 2019;**34**:43–55.
48. Edeling M, Ragi G, Huang S *et al.* Developmental signalling pathways in renal fibrosis: the roles of Notch, Wnt and Hedgehog. *Nat Rev Nephrol* 2016;**12**:426–39.
49. Panizo S, Martínez-Arias L, Alonso-Montes C *et al.* Fibrosis in Chronic Kidney Disease: Pathogenesis and Consequences. *Int J Mol Sci* 2021;**22**:408.
50. Huda MN, Borrego EA, Guarena CD *et al.* Topical Administration of an Apoptosis Inducer Mitigates Bleomycin-Induced Skin Fibrosis. *ACS Pharmacol Transl Sci* 2023;**6**:829–41.
51. Afrin H, Esquivel SV, Kumar R *et al.* β -Glucan-Mediated Oral Codelivery of 5FU and Bcl2 siRNA Attenuates Stomach Cancer. *ACS Appl Mater Interfaces* 2023;**15**:32188–200.

52. Weder B, Mamie C, Rogler G *et al.* BCL2 Regulates Differentiation of Intestinal Fibroblasts. *Inflamm Bowel Dis* 2018;**24**:1953–66.
53. Safaeian L, Abed A, Vaseghi G. The role of Bcl-2 family proteins in pulmonary fibrosis. *Eur J Pharmacol* 2014;**741**:281–9.
54. Teng K-Y, Barajas JM, Hu P *et al.* Role of B Cell Lymphoma 2 in the Regulation of Liver Fibrosis in miR-122 Knockout Mice. *Biology (Basel)* 2020;**9**:157.
55. Rudin CM, Hann CL, Garon EB *et al.* Phase II Study of Single-Agent Navitoclax (ABT-263) and Biomarker Correlates in Patients with Relapsed Small Cell Lung Cancer Navitoclax for Recurrent Small Cell Lung Cancer. *Clin Cancer Res* 2012;**18**:3163–9.
56. Senatilleke U, Abeysiriwardana H, Makubura RK *et al.* Estimation of Potential Evapotranspiration across Sri Lanka Using a Distributed Dual-Source Evapotranspiration Model under Data Scarcity. Baldi M (ed.). *Adv Meteorol* 2022;**2022**:6819539.
57. Wilczewska AZ, Niemirowicz K, Markiewicz KH *et al.* Nanoparticles as drug delivery systems. *Pharmacol reports* 2012;**64**:1020–37.
58. Dobrovolskaia MA, McNeil SE. Strategy for selecting nanotechnology carriers to overcome immunological and hematological toxicities challenging clinical translation of nucleic acid-based therapeutics. *Expert Opin Drug Deliv* 2015;**12**:1163–75.
59. Byrne JD, Baugh JA. The significance of nanoparticles in particle-induced pulmonary fibrosis. *Mcgill J Med* 2008;**11**:43–50.
60. Poilil Surendran S, George Thomas R, Moon MJ *et al.* Nanoparticles for the treatment of liver fibrosis. *Int J Nanomedicine* 2017;**12**:6997–7006.
61. Yu H, Lin T, Chen W *et al.* Size and temporal-dependent efficacy of oltipraz-loaded PLGA nanoparticles for treatment of acute kidney injury and fibrosis. *Biomaterials* 2019;**219**:119368.

62. Cao L, Chen Y, Lu L *et al.* Angiotensin II upregulates fibroblast-myofibroblast transition through Cx43-dependent CaMKII and TGF- β 1 signaling in neonatal rat cardiac fibroblasts. *Acta Biochim Biophys Sin (Shanghai)* 2018;**50**:843–52.
63. Carvajal G, Rodríguez-Vita J, Rodrigues-Díez R *et al.* Angiotensin II activates the Smad pathway during epithelial mesenchymal transdifferentiation. *Kidney Int* 2008;**74**:585–95.
64. Rupérez M, Ruiz-Ortega M, Esteban V *et al.* Angiotensin II Increases Connective Tissue Growth Factor in the Kidney. *Am J Pathol* 2003;**163**:1937–47.
65. Mezzano SA, Ruiz-Ortega M, Egido J. Angiotensin II and Renal Fibrosis. *Hypertension* 2001;**38**:635–8.
66. Afrin H, Huda MN, Islam T *et al.* Detection of Anticancer Drug-Induced Cardiotoxicity Using VCAM1-Targeted Nanoprobes. *ACS Appl Mater Interfaces* 2022, DOI: 10.1021/acsami.2c13019.
67. Huda MN, Deaguro IG, Borrego EA *et al.* Ionic liquid-mediated delivery of a BCL-2 inhibitor for topical treatment of skin melanoma. *J Control Release* 2022;**349**:783–95.
68. Varadi M, Anyango S, Deshpande M *et al.* AlphaFold Protein Structure Database: massively expanding the structural coverage of protein-sequence space with high-accuracy models. *Nucleic Acids Res* 2022;**50**:D439–44.
69. Coudert E, Gehant S, de Castro E *et al.* Annotation of biologically relevant ligands in UniProtKB using ChEBI. *Bioinformatics* 2023;**39**:btac793.
70. Trott O, Olson AJ. AutoDock Vina: improving the speed and accuracy of docking with a new scoring function, efficient optimization, and multithreading. *J Comput Chem* 2010;**31**:455–61.
71. Chaturvedi P, Kelich P, Nitka TA *et al.* Computational Modeling of the Virucidal Inhibition Mechanism for Broad-Spectrum Antiviral Nanoparticles and HPV16 Capsid Segments. *J Phys*

Chem B 2021;**125**:13122–31.

72. Eckenstaler R, Sandori J, Gekle M *et al.* Angiotensin II receptor type 1—An update on structure, expression and pathology. *Biochem Pharmacol* 2021;**192**:114673.

73. Wu EL, Cheng X, Jo S *et al.* CHARMM-GUI Membrane Builder toward realistic biological membrane simulations. *J Comput Chem* 2014;**35**:1997–2004.

74. Klauda JB, Venable RM, Freites JA *et al.* Update of the CHARMM all-atom additive force field for lipids: validation on six lipid types. *J Phys Chem B* 2010;**114**:7830–43.

75. Phillips JC, Hardy DJ, Maia JDC *et al.* Scalable molecular dynamics on CPU and GPU architectures with NAMD. *J Chem Phys* 2020;**153**.

76. Huang J, MacKerell Jr AD. CHARMM36 all-atom additive protein force field: Validation based on comparison to NMR data. *J Comput Chem* 2013;**34**:2135–45.

77. Brooks BR, Bruccoleri RE, Olafson BD *et al.* CHARMM: a program for macromolecular energy, minimization, and dynamics calculations. *J Comput Chem* 1983;**4**:187–217.

78. Laskowski RA, Swindells MB. LigPlot+: Multiple Ligand–Protein Interaction Diagrams for Drug Discovery. *J Chem Inf Model* 2011;**51**:2778–86.

79. Jurrus E, Engel D, Star K *et al.* Improvements to the APBS biomolecular solvation software suite. *Protein Sci* 2018;**27**:112–28.

80. Pavkovic M, Pantano L, Gerlach C V *et al.* Multi omics analysis of fibrotic kidneys in two mouse models. *Sci Data* 2019;**6**:92.

81. Oropeza BP, Serna C, Furth ME *et al.* Assessment of Angiogenesis and Cell Survivability of an Inkjet Bioprinted Biological Implant in an Animal Model. *Materials (Basel)* 2022;**15**, DOI: 10.3390/ma15134468.

82. Hruba VJ, Patel D. 6 - Structure–Function Studies of Peptide Hormones: An Overview. In:

- Gutte BBT-P (ed.). San Diego: Academic Press, 1995, 247–86.
83. Harvey SJ, Jarad G, Cunningham J *et al.* Disruption of glomerular basement membrane charge through podocyte-specific mutation of agrin does not alter glomerular permselectivity. *Am J Pathol* 2007;**171**:139–52.
84. Liu C-P, Hu Y, Lin J-C *et al.* Targeting strategies for drug delivery to the kidney: From renal glomeruli to tubules. *Med Res Rev* 2019;**39**:561–78.
85. Hinz B. Formation and Function of the Myofibroblast during Tissue Repair. *J Invest Dermatol* 2007;**127**:526–37.
86. Iwamiya T, Segard B-D, Matsuoka Y *et al.* Human cardiac fibroblasts expressing VCAM1 improve heart function in postinfarct heart failure rat models by stimulating lymphangiogenesis. *PLoS One* 2020;**15**:e0237810.
87. Tai Y, Woods EL, Dally J *et al.* Myofibroblasts: Function, Formation, and Scope of Molecular Therapies for Skin Fibrosis. *Biomolecules* 2021;**11**:1095.
88. Beaven E, Kumar R, Bhatt HN *et al.* Myofibroblast specific targeting approaches to improve fibrosis treatment. *Chem Commun* 2022;**58**:13556–71.
89. Hecker L, Vittal R, Jones T *et al.* NADPH oxidase-4 mediates myofibroblast activation and fibrogenic responses to lung injury. *Nat Med* 2009;**15**:1077–81.
90. Cohen EP. Fibrosis causes progressive kidney failure. *Med Hypotheses* 1995;**45**:459–62.
91. Xu Z, Dai C. Ablation of FGFR2 in fibroblasts ameliorates kidney fibrosis after ischemia/reperfusion injury in mice. *Kidney Dis* 2017;**3**:160–70.
92. Thanakitcharu P, Jirajan B. Early detection of subclinical edema in chronic kidney disease patients by bioelectrical impedance analysis. *J Med Assoc Thai* 2014;**97**:S1–10.
93. Tsai Y-C, Tsai J-C, Chen S-C *et al.* Association of fluid overload with kidney disease

- progression in advanced CKD: a prospective cohort study. *Am J Kidney Dis* 2014;**63**:68–75.
94. Ellis D. Pathophysiology, Evaluation, and Management of Edema in Childhood Nephrotic Syndrome. *Front Pediatr* 2016;**3**, DOI: 10.3389/fped.2015.00111.
95. Scallan J, Huxley VH, Korthuis RJ. Capillary fluid exchange: regulation, functions, and pathology. *Colloquium Lectures on Integrated Systems Physiology* * 18pt From *Molecules to Function*. Vol 2. Morgan & Claypool Publishers, 2010, 1–94.
96. QIU B, WEI F, SUN X *et al*. Measurement of hydroxyproline in collagen with three different methods. *Mol Med Rep* 2014;**10**:1157–63.
97. Kumar Srivastava A, Khare P, Kumar Nagar H *et al*. Hydroxyproline: A Potential Biochemical Marker and Its Role in the Pathogenesis of Different Diseases. *Curr Protein Pept Sci* 2016;**17**:596–602.
98. Wang F, Dupuis J-Y, Nathan H *et al*. An Analysis of the Association Between Preoperative Renal Dysfunction and Outcome in Cardiac Surgery*: Estimated Creatinine Clearance or Plasma Creatinine Level as Measures of Renal Function*. *Chest* 2003;**124**:1852–62.
99. Babitt JL, Lin HY. Mechanisms of anemia in CKD. *J Am Soc Nephrol* 2012;**23**:1631–4.
100. de Vos S, Leonard JP, Friedberg JW *et al*. Safety and efficacy of navitoclax, a BCL-2 and BCL-X L inhibitor, in patients with relapsed or refractory lymphoid malignancies: results from a phase 2a study. *Leuk Lymphoma* 2021;**62**:810–8.
101. Rawla P, Barsouk A. Epidemiology of gastric cancer: global trends, risk factors and prevention. *Gastroenterol Rev* 2019;**14**:26–38.
102. Thrift AP, El-Serag HB. Burden of Gastric Cancer. *Clin Gastroenterol Hepatol* 2020;**18**:534–42.
103. Drugs Approved for Stomach (Gastric) Cancer - NCI.

104. Zhang C, Liu Z-K. Gene therapy for gastric cancer: A review. *World J Gastroenterol* 2003;**9**:2390.
105. Wang LJ, Jin HC, Wang X *et al.* ZIC1 is downregulated through promoter hypermethylation in gastric cancer. *Biochem Biophys Res Commun* 2009;**379**:959–63.
106. Zhang N, Wang A-Y, Wang X-K *et al.* GAS5 is downregulated in gastric cancer cells by promoter hypermethylation and regulates adriamycin sensitivity. *Eur Rev Med Pharmacol Sci* 2016;**20**:3199–205.
107. Chen H, Pan Y, Cheng Z-Y *et al.* Hypermethylation and clinicopathological significance of RASAL1 gene in gastric cancer. *Asian Pac J Cancer Prev* 2013;**14**:6261–5.
108. Eftang LL, Esbensen Y, Tannæs TM *et al.* Up-regulation of CLDN1 in gastric cancer is correlated with reduced survival. *BMC Cancer* 2013;**13**:586.
109. Delario AJ. Problems in the Diagnosis of Cancer of the Stomach. *Am J Cancer* 1936;**27**:334–40.
110. Gu E, Song W, Liu A *et al.* SCDB: an integrated database of stomach cancer. *BMC Cancer* 2020;**20**:490.
111. Galia E, Nicolaides E, Hörter D *et al.* Evaluation of Various Dissolution Media for Predicting In Vivo Performance of Class I and II Drugs. *Pharm Res* 1998;**15**:698–705.
112. Rajput GC, Majmudar FD, Patel JK *et al.* Stomach specific mucoadhesive tablets as controlled drug delivery system—A review work. *Int J Pharm Biol Res* 2010;**1**:30–41.
113. Alshaer W, Zureigat H, Al Karaki A *et al.* siRNA: Mechanism of action, challenges, and therapeutic approaches. *Eur J Pharmacol* 2021;**905**:174178.
114. Islam T, Huda MN, Ahsan MA *et al.* Theoretical and Experimental Insights into the Possible Interfacial Interactions between β -Glucan and Fat Molecules in Aqueous Media. *J Phys*

Chem B 2021;**125**:13730–43.

115. Vetvicka V, Vannucci L, Sima P. β -glucan as a new tool in vaccine development. *Scand J Immunol* 2020;**91**, DOI: 10.1111/sji.12833.

116. Lee D-Y, Nurunnabi M, Kang SH *et al.* Oral Gavage Delivery of PR8 Antigen with β -Glucan-Conjugated GRGDS Carrier to Enhance M-Cell Targeting Ability and Induce Immunity. *Biomacromolecules* 2017;**18**:1172–9.

117. Chowdhury AS, Geetha Bai R, Islam T *et al.* Bile acid linked β -glucan nanoparticles for liver specific oral delivery of biologics. *Biomater Sci* 2022;**10**:2929–39.

118. Nutraceutical functions of beta-glucans in human nutrition. *Rocz Państwowego Zakładu Hig* 2019:315–24.

119. Schwartz B, Hadar Y. Possible mechanisms of action of mushroom-derived glucans on inflammatory bowel disease and associated cancer. *Ann Transl Med* 2014;**2**:19.

120. Su Y, Chen L, Yang F *et al.* Beta-d-glucan-based drug delivery system and its potential application in targeting tumor associated macrophages. *Carbohydr Polym* 2021;**253**:117258.

121. Xu Z-Y, Tang J-N, Xie H-X *et al.* 5-Fluorouracil Chemotherapy of Gastric Cancer Generates Residual Cells with Properties of Cancer Stem Cells. *Int J Biol Sci* 2015;**11**:284–94.

122. Kohnoe S, Maehara Y, Takahashi I *et al.* Treatment of advanced gastric cancer with 5-fluorouracil and cisplatin in combination with dipyridamole. *Int J Oncol* 1998, DOI: 10.3892/ijo.13.6.1203.

123. Sano T, Kodera Y. Japanese gastric cancer treatment guidelines 2010 (ver. 3). *Gastric Cancer* 2011;**14**:113–23.

124. Abdel-Rahman O. 5-Fluorouracil-related Cardiotoxicity; Findings From Five Randomized Studies of 5-Fluorouracil-based Regimens in Metastatic Colorectal Cancer. *Clin Colorectal*

Cancer 2019;**18**:58–63.

125. Peng H, Yang H, Song L *et al.* Sustained delivery of siRNA/PEI complex from in situ forming hydrogels potently inhibits the proliferation of gastric cancer. *J Exp Clin Cancer Res* 2016;**35**:57.

126. Afrin H, Geetha Bai R, Kumar R *et al.* Oral delivery of RNAi for cancer therapy. *Cancer Metastasis Rev* 2023, DOI: 10.1007/s10555-023-10099-x.

127. Song C, Han Y, Luo H *et al.* HOXA10 induces BCL2 expression, inhibits apoptosis, and promotes cell proliferation in gastric cancer. *Cancer Med* 2019;**8**:5651–61.

128. Siddiqui WA, Ahad A, Ahsan H. The mystery of BCL2 family: Bcl-2 proteins and apoptosis: an update. *Arch Toxicol* 2015;**89**:289–317.

129. Bold RJ, Virudachalam S, McConkey DJ. BCL2 expression correlates with metastatic potential in pancreatic cancer cell lines. *Cancer* 2001;**92**:1122–9.

130. Boidol B, Kornauth C, van der Kouwe E *et al.* First-in-human response of BCL-2 inhibitor venetoclax in T-cell prolymphocytic leukemia. *Blood* 2017;**130**:2499–503.

131. Mei J, Liu G, Li R *et al.* LncRNA SNHG6 knockdown inhibits cisplatin resistance and progression of gastric cancer through miR-1297/BCL-2 axis. *Biosci Rep* 2021;**41**, DOI: 10.1042/BSR20211885.

132. Kang SH, Revuri V, Lee SJ *et al.* Oral siRNA Delivery to Treat Colorectal Liver Metastases. *ACS Nano* 2017, DOI: 10.1021/acsnano.7b05547.

133. Muddineti OS, Rompicharla SVK, Kumari P *et al.* Vitamin-E/lipid based PEGylated polymeric micellar doxorubicin to sensitize doxorubicin-resistant cells towards treatment. *React Funct Polym* 2019;**134**:49–57.

134. Yamachika T, Nakanishi H, Inada K *et al.* N-methyl-N-nitrosourea concentration-

- dependent, rather than total intake-dependent, induction of adenocarcinomas in the glandular stomach of BALB/c mice. *Jpn J Cancer Res* 1998;**89**:385–91.
135. Hayakawa Y, Fox JG, Gonda T *et al.* Mouse models of gastric cancer. *Cancers (Basel)* 2013, DOI: 10.3390/cancers5010092.
136. Boegh M, Nielsen HM. Mucus as a Barrier to Drug Delivery – Understanding and Mimicking the Barrier Properties. *Basic Clin Pharmacol Toxicol* 2015;**116**:179–86.
137. Kaur R, Sharma M, Ji D *et al.* Structural Features, Modification, and Functionalities of Beta-Glucan. *Fibers* 2020;**8**, DOI: 10.3390/fib8010001.
138. Miao X, Li Y, Wyman I *et al.* Enhanced in vitro and in vivo uptake of a hydrophobic model drug coumarin-6 in the presence of cucurbit[7]uril. *Medchemcomm* 2015;**6**:1370–4.
139. Kong N, Zhang R, Wu G *et al.* Intravesical delivery of KDM6A-mRNA via mucoadhesive nanoparticles inhibits the metastasis of bladder cancer. *Proc Natl Acad Sci* 2022;**119**:e2112696119.
140. Aydin S, Ozercan İH, Dagli F *et al.* Ghrelin immunohistochemistry of gastric adenocarcinoma and mucoepidermoid carcinoma of salivary gland. *Biotech Histochem* 2005;**80**:163–8.
141. Lazăr D, Tăban S, Sporea I *et al.* Ki-67 expression in gastric cancer. Results from a prospective study with long-term follow-up. *Rom J Morphol Embryol* 2010;**51**:655–61.
142. Itaya M, Yoshimoto J, Kojima K *et al.* Usefulness of p53 protein, Bcl-2 protein and Ki-67 as predictors of chemosensitivity of malignant tumors. *Oncol Rep* 1999, DOI: 10.3892/or.6.3.675.
143. Sethy C, Kundu CN. 5-Fluorouracil (5-FU) resistance and the new strategy to enhance the sensitivity against cancer: Implication of DNA repair inhibition. *Biomed Pharmacother*

2021;**137**:111285.

144. Tsurudome I, Miyahara R, Funasaka K *et al.* In vivo histological diagnosis for gastric cancer using endocytoscopy. *World J Gastroenterol* 2017;**23**:6894–901.

Vita

I am Humayra Afrin, a PhD candidate from the department of Environmental Science and Engineering. I completed my Doctor of Medicine from Rangpur Medical College, Bangladesh. After completing my residency, I joined as a medical officer in the department of Oncology. At that time, I became interested in research regarding human health, specifically on cancer. With this goal in mind, I started to look for higher studies and research opportunities abroad. I got admission to The University of Texas at El Paso and started working under the supervision of Dr. Nurunnabi in the School of Pharmacy. In UTEP I work on targeted drug delivery for cancer and fibrosis to improve therapeutic efficacy with minimum or no toxicity. For that, I design bioengineered or biomimetic molecules as a delivery vehicle. My research also focuses on alternative delivery approaches to improve patient compliance, easy administration, less drug induced toxicity, and better therapeutic effect than conventional route. I examined the role of Bcl2 in cancer and fibrosis development and treatment approaches. For my initial work I developed a nanoprobe to identify the Doxorubicin induced cardiac damage. My study observed that Vcam1 is overly expressed in chronic Doxorubicin exposed heart. Later, I delivered Bcl2 siRNA orally for stomach cancer treatment with Beta-glucan and Navitoclax (a Bcl2 inhibitor) intravenously with PLGA nanoparticle for kidney fibrosis. My work resulted in 13 peer-reviewed publications with 2 patents. For my work I received several awards including Dodson research grant, Jess hay chancellors fellowship form UT system. For my future work I want to continue my work in academic research involving newer pathways for disease development and treatment.

Contact Information: hafrin@miners.utep.edu